AES/PE

Modelling the spectral gamma-ray log: the influence of provenance and selective transport

August 1, 2014

M. C. van der Boor

TU Delft Delft University of Technology
Challenge the future

Delft University of Technology

Master thesis

Modelling the spectral gamma-ray log: the influence of selective transport and provenance

Martijn van der Boor

August 2014

Graduation Committee:

Dr. G.J. Weltje	Supervisor
Dr. A. Barnhoorn	Co-reader
Ir. M.R. Bloemsma	Co-reader
Dr. R.L. Koomans	External Committee-member

Department of Applied Earth Sciences
Delft University of Technology
The Netherlands

Abstract

In clastic rock, the interpretation of facies from the spectral gamma-ray log should be applied with caution because a consistent relationship with gamma-ray is lacking due to variations in provenance and/or diagenesis. In this thesis the use of the gamma-ray log for the derivation of source rock characteristics and/or diagenesis is examined. This is done by reconstructing part of the history of the sedimentary rock by modelling or minimizing the variance caused by selective transport in the gamma-ray signal and interpreting the residual signal. Two different approaches were studied:

In the first approach a model was suggested which simulates the selective transport process. The composition of sediment subject to selective sorting is modelled as a compositional linear trend where the proportion of minerals increase or decrease as function of the settling velocity of the grains. Diagenesis and mixing of sediment sources is neglected in this model. With the forward model characteristics reflecting the parent lithology such as composition and radio-nuclide concentration can be used to simulate a gamma-ray signature. Iterative forward modelling was used in an attempt to derive provenance characteristics from the gamma-ray signatures. The performance of the model was tested on synthetic and real gamma-ray signatures. With the iterative forward model an excellent fit with the well log gamma-ray was found however, the resulting radio-nuclide concentrations show an unrealistic large variation. Two conclusions were drawn based on these outcomes, first the model is very sensitive to the noise present in gamma-ray logs and secondly not enough constraints are available to produce realistic results from the model.

The second approach is based on simplifying assumption concerning selective transport. It is assumed sediment within a sufficiently small grain size class is deposited under similar hydraulic conditions and therefore has a comparable (chemical) composition if there are no variation in provenance or diagenesis. If this is the case, the gamma-ray log can be reconstructed from a grain size record if we take into account the variation caused by the averaging effect of the detector. The detectors response was approximated based on attenuation effects in the formation and allows us to degrade the high resolution

gamma-ray log derived from the grain size record to a resolution matching the well log gamma-ray. Application to carboniferous core E10-3 resulted in a good fit and realistic gamma-ray signatures for the grain size classes. Thorium showed the highest dependency with grain size, potassium and uranium show a comparable and less pronounced correlation. In case of core E10-3 the residual variance is expected to be mainly caused by diagenesis (formation of kaolinite), degree of sorting and organic content and it was concluded that in this case the residual signal is hard to interpret. The model was also applied to the point bar deposits of the Huesca dataset. Again the thorium content showed the highest dependency with grain size, the uranium content showed less strong correlation and no clear relationship of the grain size record with the potassium content was found. Individual processing of the point bar deposits clearly showed an increased potassium content in the point bar at the depth interval 57m - 61m. Several plausible explanations can be posed for the increased potassium content, for example the potassium content could be present as a solution in the pore structure, higher proportion of K-feldspar or increased radio-activity of the potassium bearing minerals.

Acknowledgement

I would like to express my sincere gratitude to my thesis supervisors Gert Jan Weltje and Menno Bloemsma for their continuous help and support throughout this thesis. I am very happy I was always welcome for any discussion and I have learned a lot in the process.

It was always pleasant to visit Medusa and I would like to thank them for their time and effort invested in this thesis. In particular Ronald Koomans for being part of my graduation committee and for the discussions during the project and Marco Tijs for conducting the core-plug gamma-ray measurements and helping with the processing.

I would like to thank Panterra BV and Wintershall Noordzee BV for their efforts in making core E10-3 available. Also, I would like to thank Rick Donselaar for providing me with the Huesca data and samples.

Finally, I would like to thank Auke Barnhoorn for being part of my graduation committee and taking the time to read my thesis.

Contents

List of Figures

List of Tables

Chapter 1

Introduction

1.1 Introduction

The objective of petrophysical analysis is to interpret characteristic reservoir units which are grouped based on fluid flow properties. Fluid flow properties depend on the rock's physical characteristics, for instance texture and composition. These characteristics can be determined directly from subsurface samples but indirect measurements of geophysical parameters can be obtained faster and with lower costs. The main source for this type of information are well logs. Well logs are interpreted by geoscientists and petrophysicist and translated into subsurface properties used to assess the reservoir properties.

The natural gamma-ray log is an example of one commonly used well log and records the quantity of natural occurring radio-nuclides of potassium (K), uranium (U) and thorium (Th). These elements are incorporated in a wide diversity of minerals but higher concentrations are often observed in specific mineral groups. In sedimentary rock it is commonly observed shale is more radio-active than sandstone due to the presence of clay minerals which are often enriched in thorium and uranium. A link between gamma-ray and grain size therefore appears to exist: the fine grained fraction contains more clay minerals, which in turn are more radio-active than the coarse fraction which contains weak or non-radioactive minerals such as quartz or calcite.

Trends in grain size are an important clue for the depositional environment in which the rock was formed, for example rivers with an high discharge can transport coarse and fine grains while aeolian deposits mainly transport the finest fraction. Given the apparent relation between gamma-ray and grain size, characteristic gamma-ray shapes were used as indicator for depositional facies. A classic example is the bell shaped gamma-ray curve, which is interpreted as a fining upward grain size trend and is associated with a deltaic or fluvial bar, see figure 1.1.

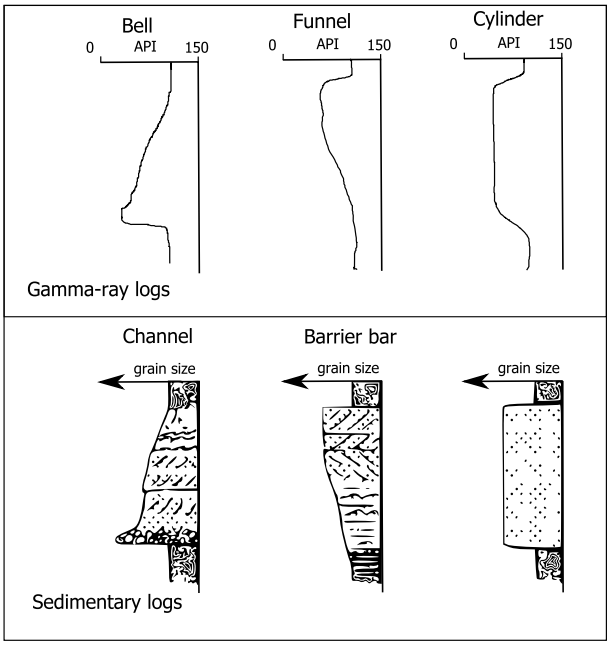

FIGURE 1.1: Shape of the gamma-ray curve and their depositional facies association, after Serra et al. (1975).

The simple relationship between gamma-ray and grain size does not always hold as several authors have pointed out, see for example Hurst (1990); Rider (1990). The most important reason being the large variation in properties and composition of sedimentary rock. Sedimentary rock can consist of various coarse and fine grained radio-active minerals with varying concentrations of radio-nuclides, without additional information increased radioactivity cannot be attributed to the fine grained fraction. The composition of sedimentary rock is controlled by various process, summarized in figure 1.2. The composition of the source rock controls the mineralogy (the chemical composition) of the weathered and eroded sediment. The sediment is then selectively dispersed based on properties as size, shape and density. After deposition and lithification, the minerals chemical composition and texture changes (diagenesis) resulting in a modified set of minerals.

1.2 Objectives

All the processes involved in the evolution of clastic sediment to the formation of a sedimentary rock also affect the chemical composition, partly reflected by the gamma-ray signature. Ideally, when interpreting the gamma-ray log the variability of these processes should be incorporated to be successful. For example the empirical statement: *increasing radio-activity reflects a decreasing grain size trend* does not take into account the variability in mineralogy of the parent rock and therefore fails in some cases. A

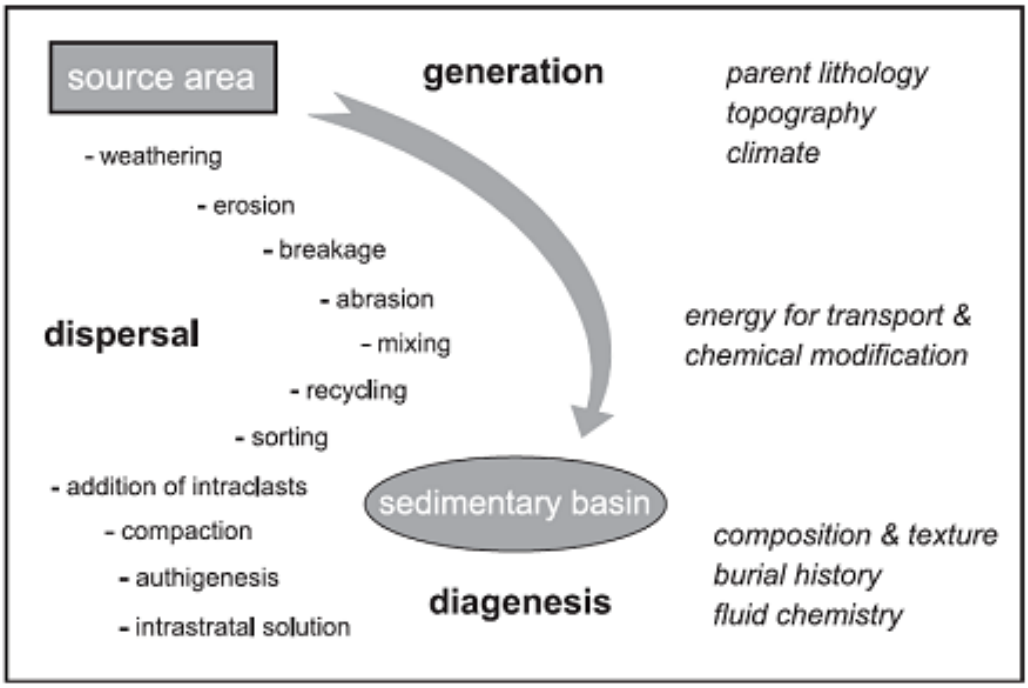

FIGURE 1.2: Main processes involved in the evolution of clastic sediment Weltje and von Eynatten (2004).

better statement would be: *rock showing a fining upward grain size trend derived from source X shows gamma-ray signature Y* a more accurate statement because it takes into account the provenance. This restricts the interpretation of the gamma-ray log in the sense that more information is needed to untangle the variability but in return potentially useful information can be derived from the residual signal. This principle forms the basis for this thesis. The goal in this thesis is not to derive information concerning facies but we focus on the residual signal after the effects of facies are minimized. The main research question is:

Can we improve the use of the gamma-ray log?

In the first section of this thesis we will focus on the effects of selective transport and provenance on the gamma-ray signature. Sediment is often selectively dispersed based on hydraulic properties such as size, density and shape. If we can determine the hydraulic properties of sediment grains and the characteristics of the source rock, a gamma-ray signature can be simulated. If forward prediction of gamma-ray signatures is feasible, inverse modelling techniques can be applied to derive important characteristics of the source rock from gamma-ray signatures. The first goal of this thesis is:

Can we accurately model the gamma-ray signature of sediment subject to size selective sorting?

Instead of modelling the gamma-ray signature, a different approach is to minimize the effect of the process on the gamma-ray signature. This can be achieved by grouping properties such that the variation caused by a process is more or less equal in each group. The second goal of this thesis is to use this approach to minimize the effect of selective transport on the gamma-ray signature. Transport of sediment is selective and grain size is one of the most important parameters governing the behaviour of sediment grains during transport. Sediment grains which have a comparable grain size are expected to be transported together, minimizing the effect of fractionation. The variation of the gamma-ray signature of sediment grains within a (sufficiently small) grain size class are therefore expected to be mainly dependent on other processes such as variation in provenance and diagenesis. With a gamma-ray signature of a grain size class we can attempt to reconstruct the gamma-ray log, which should reveal a residual signal if variation is present unrelated to selective transport. Core-plug samples will be used to determine an high resolution response of the gamma-ray signature of a grain size class.

Can we derive information from the residual gamma-ray signal if the variation caused by selective transport is minimized?

1.3 Outline of the thesis

In chapter 2 a brief introduction of the basics of natural gamma-ray logging and sources of natural gamma-ray will be given. In chapter 3 the mathematical theory of compositional data analysis is be introduced. The theory of compositional data analysis will be used throughout this thesis to model compositional trends and is applied to the analysis of gamma-ray logs.

In chapter 4 the approach of the selective sorting model will be explained and applied to two synthetic datasets to produce gamma-ray patterns of two distinct sediment sources. Iterative forward modelling is applied to synthetic data to assess the performance. This chapter is mainly theoretical in chapter 6 the performance of the model will be assessed on a real dataset. In chapter 5 a different approach is assessed in which the contribution of selective sorting is minimized and the models are applied to a dataset of well E10-3. In chapter 6 both theoretical models will be applied to the Huesca core.

Chapter 2

Natural gamma-ray logging

This chapter serves as introduction and background for the basic principles of importance in gamma-ray logging and theory used later in this thesis. We will briefly cover the basics of gamma-ray logging: particle interaction with matter, detection and identification of gamma-rays. Finally, an overview will be given of (common) sources of natural gamma-ray in the subsurface.

2.1 Radio-active decay

Radio-activity is the spontaneous decay of unstable atoms to a more stable state by emitting some form of radiation. The SI unit of radio-activity is Becquerel (s^{-1}) , indicating one disintegration per second. Three types of radio-active decay can be distinguished: alpha, beta and gamma decay. Alpha and beta-decay involve the ejection of particles (an helium and an electron respectively). Gamma-radiation involves the ejection of photons, electromagnetic radiation similar to visible light, but with an high frequency and energy. This process is stochastic, each nuclei has a probability (λ) of decaying independent from external influences. The number of remaining radio-nuclides $N(t)$ decayed after time of time t relative to N_0, the initial number of nuclides, can be expressed as:

$$N(t) = N_0 e^{-\lambda t} \tag{2.1}$$

The activity of the source is more commonly defined as its half-life $t_{1/2}$: the statistical time required for half of the atoms to decay:

$$t_{1/2} = \frac{ln(2)}{\lambda} \tag{2.2}$$

The activity of a source in Bq is related to the ratio of the total mass m in grams and the atomic mass m_a in grams per mol (i.e. the number of moles), Avogrado's constant N_A (mol^{-1}) and the half live $t_{1/2}$:

$$A_{Bq} = \frac{m}{m_a} N_A \frac{ln(2)}{t_{1/2}} \tag{2.3}$$

The most import gamma-ray emitters in nature are isotopes of potassium (^{40}K), uranium (^{238}U) and thorium (^{232}Th). Half-lives of ^{40}K,^{238}U and ^{232}Th are comparable to or larger than the age of the Earth. These unstable isotopes decay to stable isotopes by emission of (a combination of) alpha- or beta-particles or gamma-radiation. Figure 2.1 shows the simplified decay chains for ^{40}K, ^{238}U and ^{232}Th. The figure shows that ^{232}Th and ^{238}U have several and ^{40}K has one, gamma-ray emitting daughter in their decay chain. Each daughter product emits a photon at a distinct energy level. If elements within a decay chain exist in secular equilibrium (the rate of elements generated is equal to the rate of elements destroyed) the energy spectrum can be analysed and related to the abundance of K, U and Th. There are various ways to analyse an energy spectrum. A straightforward analysis is to count the number of particles at a characteristic energy peaks produced by the daughter products. Energy of particles is commonly recorded in electron volts (eV) where one eV corresponds to $1.6 \times 10^{-}19$J. For instance if ^{238}U decays a peak will be recorded at 1.76 MeV (gamma-ray emitted from ^{214}Bi), for ^{232}Th this is at 2.61 MeV (^{208}Ti) and for ^{40}K there is only one gamma-ray emitter at 1.46 MeV. The frequency these energy levels are recorded is directly proportional to the abundance of K, U and Th.

2.2 Interaction with matter

Interaction of photons with matter can causes a gradual or instant release of the photons energy. There are various ways a photon can interact with an atom, depending on the energy of the particle and atomic number Z of the absorber, two types of interaction are dominant in natural gamma-ray logging where the energy is below 3 MeV (Hendriks et al., 2001):

1. Photo-electric effect
2. Compton scattering

In the photoelectric effect, collision between photons and electrons causes the bound electron to be ejected from its atom. The energy from the photon is completely absorbed

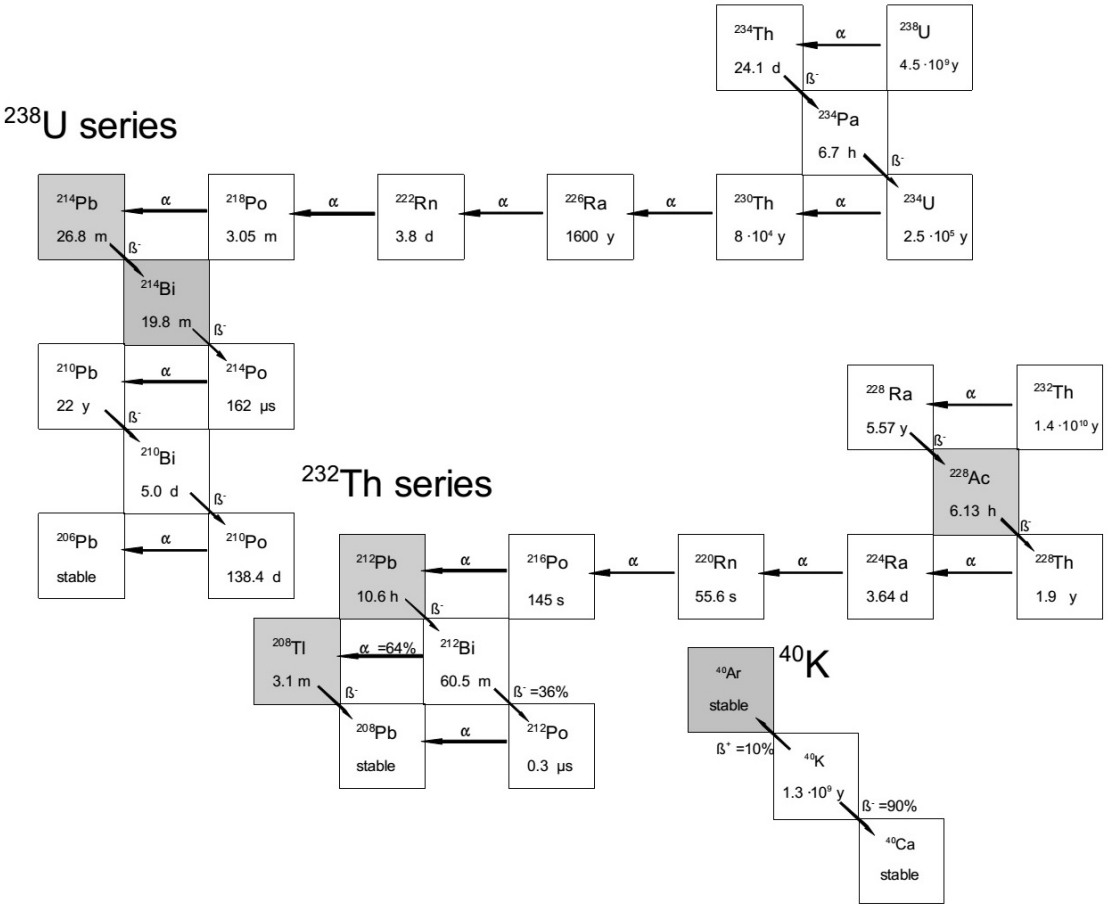

FIGURE 2.1: Simplified decay chains of ^{40}K, ^{238}U and ^{232}Th (Koomans, 2000). The grey boxes indicate important gamma-ray emitters. Half life of each element in years (y), months (m), days (d), hours (h) or seconds (s)

in the process (Serra, 1988). The electron is ejected if the energy of the photon is higher than the binding energy of the electron. This effect is dominant at low photon energy or high atomic number (Z) of the absorber. Compton scattering is dominant at higher energy levels, here a photon is scattered of an electron, the photon loses energy in the process. The number of unattenuated photons over an absorber with thickness r is given by the general gamma-ray attenuation relationship:

$$N = N_0 e^{-\mu \rho_b r} \tag{2.4}$$

Where N_0 is the number of emitters present in the source, ρ_b is the density of the absorber and μ is the mass attenuation coefficient. The mass attenuation coefficient accounts for the photo-electric effect and Compton scattering and can be seen as is the probability per unit length a photon will interact with an absorber. High energy photons have a larger probability of passing through an absorber undisturbed, at low energies or higher atomic number the probability of either Compton scattering or photo-electric

interaction increases.

2.3 Detection of gamma-rays

Scintillation crystals are most commonly used to record a gamma-ray spectrum. Scintillation crystals emit light when a photon interacts with the material, the intensity of the emitted light is proportional to the released energy of the photon. The light signal is processed by various electronics and stored. From the resulting spectrum the proportions of K [%], U [ppm] and Th [ppm] of the formation can be determined. The identification of isotopes is only possible if the energy of the photon is completely absorbed by the the detector i.e. absorbed photoelectrically. Due to Compton scattering in and around the detector, incident gamma-ray particles may already have lost, or gradually lose, their energy in the detector before photoelectric absorption. As a result the recorded energy spectrum is continuous and not a collection of discrete (photo-)peaks. The resolution of a spectrum is further degraded by the electronics used to to process the light pulses, resulting in broadening of peaks.

In the oil industry windows analysis is commonly used to analyse the energy spectra. In windows analysis the energy range is divided into a number of energy windows (often upto 256 windows are used). The counts in each window are related to the counts contributed by each radio-nuclide by determining a so called 'response matrix' in a calibration pit with known radio-nuclide concentrations (Ellis, 2007).

$$\begin{pmatrix} W_1 \\ W_2 \\ \vdots \\ W_n \end{pmatrix} = \bar{A} \begin{pmatrix} Th \\ U \\ K \end{pmatrix} \tag{2.5}$$

Where W_i is the $n \times 1$ matrix with count rates of window i and $\bar{A}$ is $n \times 3$ response matrix. The coefficients of matrix $\bar{A}$ correct the count-rate in each window to a radio-nuclide specific count-rate, this process is called 'spectral stripping'. Multiple radio-nuclides can contribute to one window (see figure 2.2), for example the Compton continuum of thorium and uranium overlap some of the energy windows close to the photopeak of potassium.

Equation 2.5 is overdetermined and does not take into account noise effects, the final solution is obtained by minimizing the square of the residuals r_i^2 in the equation:

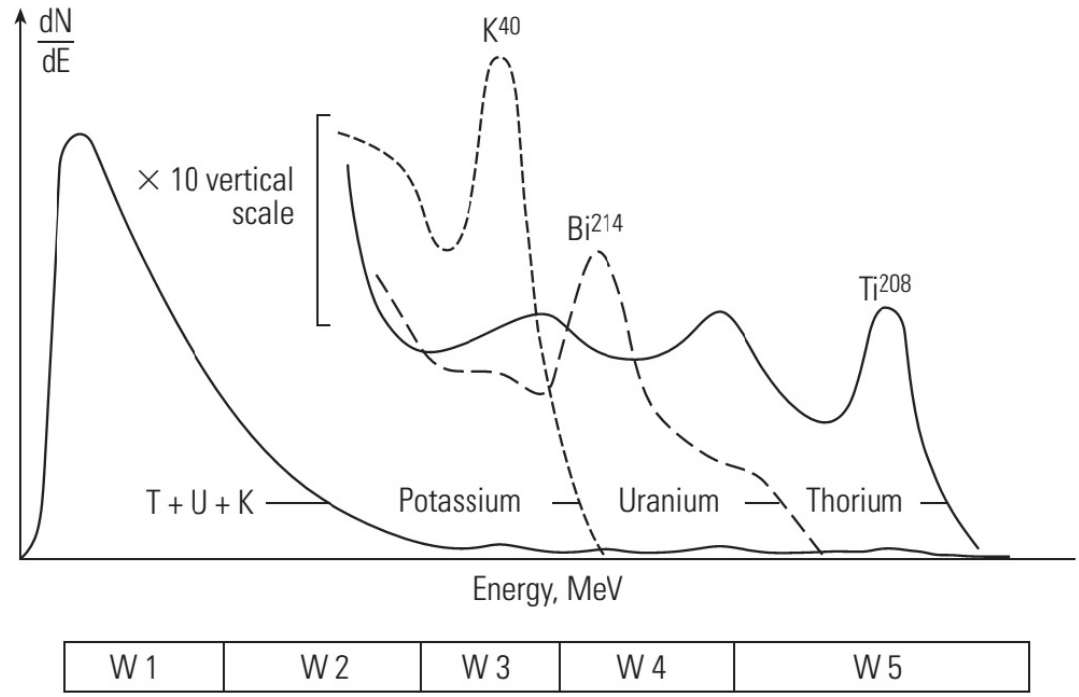

FIGURE 2.2: Schematic spectrum as measured by a crystal (Ellis, 2007). Sharp peaks are due to the photoelectric effect. Compton scattering can be observed in the lower energy levels next to a peak. In this figure five energy windows are used to determine concentrations of radio-nuclides.

$$\sum_{i=1}^{n}(W_i - A_iTh - B_iU - C_iK)^2 = \sum_{i=1}^{n} r_i^2 \tag{2.6}$$

r_i is the residual counting rate for each window i due to noise or background radiation. The coefficients A_i, B_i and C_i are elements from $\bar{A}$ relating the count in window i to the actual radio-nuclide concentration. Often these coefficients are called 'standards' or 'standard spectra' as they represent the response of the detector in a given geometry to a known radio-active source. The calibration can be done in a calibration pit or with Monte-Carlo simulations.

2.4 Sources of natural gamma-ray

Potassium is a common element on Earth, around 2.5% in weight abundance and often present in the crystal lattice of minerals (Ellis, 2007). The natural abundance of the isotope ^{40}K in potassium is 0.0118%. Common minerals containing potassium are K-feldspars, micas and clay minerals. During alteration (some of) the potassium in micas and feldspars is liberated and may be transported in solution (Serra, 1988). The elements thorium and uranium are a lot more scarce ($10^{-4} - 10^{-2}$ % in weight) and consist

almost exclusively of isotopes of ^{238}U and ^{232}Th (99.28% and 100% respectively). Minerals containing thorium and uranium in their mineral structure are rare, they are often present in minerals due to adsorption (adhesion of atoms to a solid surface) or locked in as impurities. The distribution of uranium is found to be very irregular, it is often 'trapped' in organic material (Fertl et al., 1988). Thorium is fairly insoluble and thorium bearing minerals are more stable. It is therefore the most reliable shale indicator and has been related to heavy minerals such as zircon and rutile. (Hassan et al., 1976).

Due to the complex processes involved in formation of minerals the radio-activity varies depending on the environment in which the mineral was formed and diagenetic processes after formation. Table 2.1 shows a list of some common minerals with concentrations of K, U, Th based on a table compiled by Luthi (2000). It should be noted that these values are an approximation. Hurst (1990) noted that the measurements are often based on low number of samples and lack statistical parameters. Measurements have often been performed on coarse grained samples (for example mineral veins).

Mineral	K (%)	U (ppm)	Th (ppm)
Quartz	**0.08**	**0.7**	**2**
Orthoclase	**14** (10.9 - 16)	0.2 - 3	**5** (3 - 7)
Albite	0.2 - 5	0.5 - 3	-
Anorthite	0.2 - 5	0.5 - 3	-
Illite	**6.7** (3.5 - 8.3)	1.5 - 12.4	10 - 25
Kaolinite	**0.35** (0.0 - 0.5)	1.5 - 9.0	6 - 42
Smectite	**1.6** (0.0 - 4.9)	2.0 - 7.7)	10 - 24
Chlorite	0 - 0.3	-	0 - 8
Muscovite	7.8 - 9.8	2 - 8	20 - 25
Biotite	6.2 - 10	1 - 40	**25** (5 - 50)
Zircon	-	100 - 500	100 - 500
Apatite	-	10 - 100	10 - 100
Hornblende	0.5 - 3	-	-
Xenotime	-	500 - 3000	100 - 500

TABLE 2.1: Radioacitivity in common minerals and some heavy minerals used in this thesis. Table modified from (Luthi, 2000) and (Serra, 1988), heavy mineral values from (Carmichael, 1982). Bold values indicate average values, values indicated with '-' are unknown or very low.

2.5 Gamma-ray well logs

Gamma-rays can penetrate through large amounts of mass and can therefore be detected in a borehole despite the presence of borehole fluids or casings. In the petroleum industry knowledge of the chemical composition is valuable for example as an indicator of mineralogy of a formation. Gamma-ray measurements are fast and can be performed in-situ and are logged in almost every well. Two type of logs are used in the oil industry, the total gamma-ray log and the spectral gamma-ray log. The total gamma-ray log shows the total activity of the formation and is recorded in American Petroleum Institute (API) units. The API units were designed as a standardization to account for variations in detector size by calibration in an artificially radio-active pit with known element abundance to solve the parameters α, β and γ from the equation (Ellis, 2007):

$$GR_{API} = \alpha \cdot U(ppm) + \beta \cdot Th(ppm) + \gamma \cdot K(\%) \tag{2.7}$$

The values α, β and γ are detector specific but can be approximated by 4, 8 and 16 for modelling purposes (Luthi, 2000). Presently the spectral gamma-ray is standard since it provides more (detailed) information than the total gamma-ray log. The units used are % (K) and parts per million (U and Th), these mass concentrations are linearly related to the activity in Bq/kg (see equation 2.3).

Count statistics

Radioactive decay is a random process and follows the Poisson distribution, the count-rate of a source is therefore not constant. For simplicity the count error introduced is usually approximated with a normal distribution, where the mean is equal to the total counts and the standard deviation is equal to the square root of the total counts. For large values this is a very good approximation of the Poisson distribution.

Chapter 3

Compositional data analysis

In this chapter we will explain the concepts of compositional data analysis, a mathematical framework used throughout this thesis. A lot of restrictions on compositional data are commonly ignored, by transforming compositional data these restriction disappear and normal statistical methods can be applied without limitations.

3.1 Compositional data

Many data in earth sciences consist of compositional data: proportions of some whole. Compositional data is constrained in several ways: proportions are always positive and the sum of all components equals a constant f.e. 1, 100%, 1.000.000 ppm etc. The compositional space spanned by the components is called the simplex. A common graphical representation of a three part composition is the ternary diagram. The simplex S^D is defined as:

$$S^D = [x_1, \ldots, x_D] : x_i > 0 (i = 1, \ldots, D), x_1 + \ldots + x_D = \boldsymbol{\kappa} \tag{3.1}$$

Where $x_1 \ldots x_D$ are the components of a composition $\boldsymbol{x}$ with D-parts and constant sum $\boldsymbol{\kappa}$. A D-part composition has dimension $D - 1$ due to the constant sum constraint. The ternary diagram for instance is a three part composition S^3 but can be expressed with two values only, the third value can be determined by subtracting the sum of the preceding elements from the constant sum κ. The choice of the constant κ can be chosen to be any value. If z_i is a component from the composition $\mathbf{z}$, the closure operation $\mathcal{C}$ for any constant sum κ is given by:

$$\mathcal{C}(\mathbf{z}) = \left[\frac{\kappa z_1}{\sum_{i=1}^{D} z_i}, \frac{\kappa z_2}{\sum_{i=1}^{D} z_i}, \ldots, \frac{\kappa z_D}{\sum_{i=1}^{D} z_i}\right] \tag{3.2}$$

Closed compositional data share a common denominator and only provide information about the relative magnitudes of the parts. For example if we want to determine the proportions of quartz (Q), feldspar (F) and clay (C) in a sample by point counting, all the terms share a common denominator (Q+F+C). When comparing compositions an increase of one proportion can be caused by 1) an increase of the proportion 2) a decrease of the other proportions 3) a combination.

Due to the constant sum constraint we cannot use standard statistical methods to analyse compositional data because important statistical parameters such as the variance and covariance are not uniquely defined. For instance these parameters will change for the same element in a different sub-composition (Weltje, 2012). The non-negativity constraints complicates matter even further. Aitchison (1986) solved these problems by log-transforming the data. Transformation of the data removes the constraints and data can be analysed with normal statistical methods, figure 3.1 shows three compositional paths on a ternary graph and in the log-ratio space.

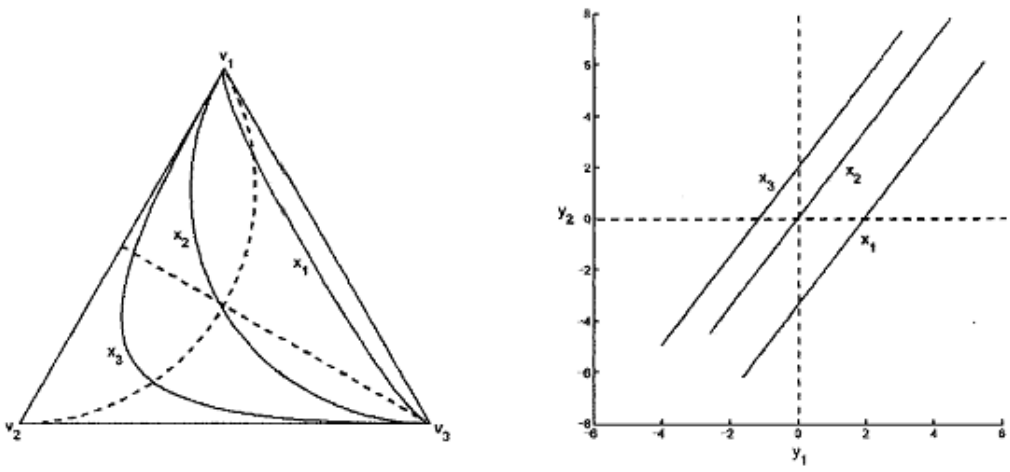

FIGURE 3.1: Compositional changes on a ternary graph and the same changes in the log-ratio-space

In the log-transformed sample space we are free to modify a component in the composition without perturbing the other values or affecting the unit sum constraint. The most straightforward transformation is the additive log-ratio transform (alr) $S^D \rightarrow R^{D-1}$ and is defined as:

$$\mathbf{y} = alr(\mathbf{x}) = \left[ln(\frac{x_1}{x_D})ln(\frac{x_2}{x_D})\dots ln(\frac{x_{D-1}}{x_D})\right] \tag{3.3}$$

The common divisor can be chosen freely and does not affect the final result, we can rewrite the right hand side of the equation to $[ln(x_1) - ln(x_D)ln(x_2) - ln(x_D)\dots ln(x_{D-1}) - ln(x_D)]$ to see that the divisor only results in a shift on the real plain. We can transform back to compositional space, $R^{D-1} \rightarrow S^D$ with the inverse log-ratio transformation alr^{-1}:

$$\mathbf{x} = alr^{-1}(\mathbf{y}) = \mathcal{C}[e^{y_1}ey_2\dots e^{y_{D-1}}] \tag{3.4}$$

The *alr* transformation is asymmetric. The centred log-ratio transform (*clr*) is the symmetrical version of the *alr* transform $S^D \rightarrow U^D$:

$$\mathbf{z} = clr(\mathbf{x}) = \left[ln(\frac{x_1}{g(\mathbf{x})})\dots ln(\frac{x_D}{g(\mathbf{x})})\right] \tag{3.5}$$

Where $g(\mathbf{x})$ is the geometric average. The *clr* transformed dataset centres around zero in an unconstrained hyperplane (U^D).

3.1.1 Relevance to gamma-ray logging

In natural gamma-ray logging the compositional data consists of weight proportions of potassium [%], uranium [ppm] and thorium [ppm]. As discussed in chapter 2 the quantities obtained in gamma-ray logging are extracted from counts in energy windows, therefore the measurements of K, U and Th do not have a common denominator. However, the quantities are sum constrained and statistical analysis on proportions is only justified on unconstrained data. Throughout this thesis we will use the compositional data framework and present the radio-nuclide concentrations as trajectories through alr-tranformed space. The data is plotted on three axis: $ln(API), ln(\frac{4U}{8Th}), ln(\frac{16K}{8Th})$. The coefficients do not affect the result of the analysis but are chosen to represent the API coefficients, see equation 2.7.

Chapter 4

Selective sorting model

The first goal of this thesis is constructing a model which simulates part of the rock forming process: fractionation. The model can be used to predict the gamma-ray signature of selectively dispersed sediment where the sediment is sorted based on settling velocity (size, shape and density). The gamma-ray signature of the sorted sediment is a function of the proportion of radio-active minerals and the concentration of radio-nuclides present in the minerals.

In the first section of this chapter the modelling approach will be explained and the model will be applied to two synthetic datasets with two distinct sediment sources. After the construction of the forward model, iterative forward modelling techniques will be applied to estimate sediment properties from a synthetic gamma-ray signature.

4.1 Modelling approach

Consider a sediment source where the composition and size of the grains is known. The sediment eroded from the source rock is transported by a fluvial system. The energy in the system decreases as the distance from the source increases. The energy decrease in the system will cause the sediment to sort (laterally) as function of their hydraulic properties. Dense and coarse particles settle first, less dense and fine particles will be kept in suspension longer and settle further away from the source. This process results in a (predictable) compositional trend. Close to the source the proportion of coarse and fine grains remain unaltered, since all particles are still entrained by the flow. Further away from the source the proportion of fine grained material entrained by the the flow increases as the flow is unable to entrain the coarse particles. We suggest a compositional linear trend to describe this process (see chapter 3). Compositional linear

trends have been successfully applied to describe trends in mechanical weathering or mixing of sediment sources, see for example von Eynatten (2004); Weltje (2012) for a more detailed description. The mathematical expression of the model is:

$$clr(X(k)) = clr(X_0) + k \cdot clr(W) \tag{4.1}$$

All the matrices are vectorized first before being transformed to clr-space i.e. the matrix is closed over all values. The definitions of the matrices in this equation are largely based on the work of Weltje (2004). The composition of the transported sediment is represented by matrix X at 'sorting step' k. Where X is a $[m \times p]$ matrix, containing the mineral composition m per grain size class p of the sediment at each step k. The matrix X_0 contains the composition of the sediment before transport. The sum of all elements in matrix X equals 1. The scalar $k \in \mathbb{R}$ can be viewed as the change in energy in the system at every step. For negative values of k after each sorting step the system loses energy to maintain suspension, resulting in a decrease of the proportion of minerals with high settling velocities. The perturbing $[m \times p]$ matrix W contains the settling velocities of each mineral m in grain size class p. See figure 4.1 for a schematic representation of this process.

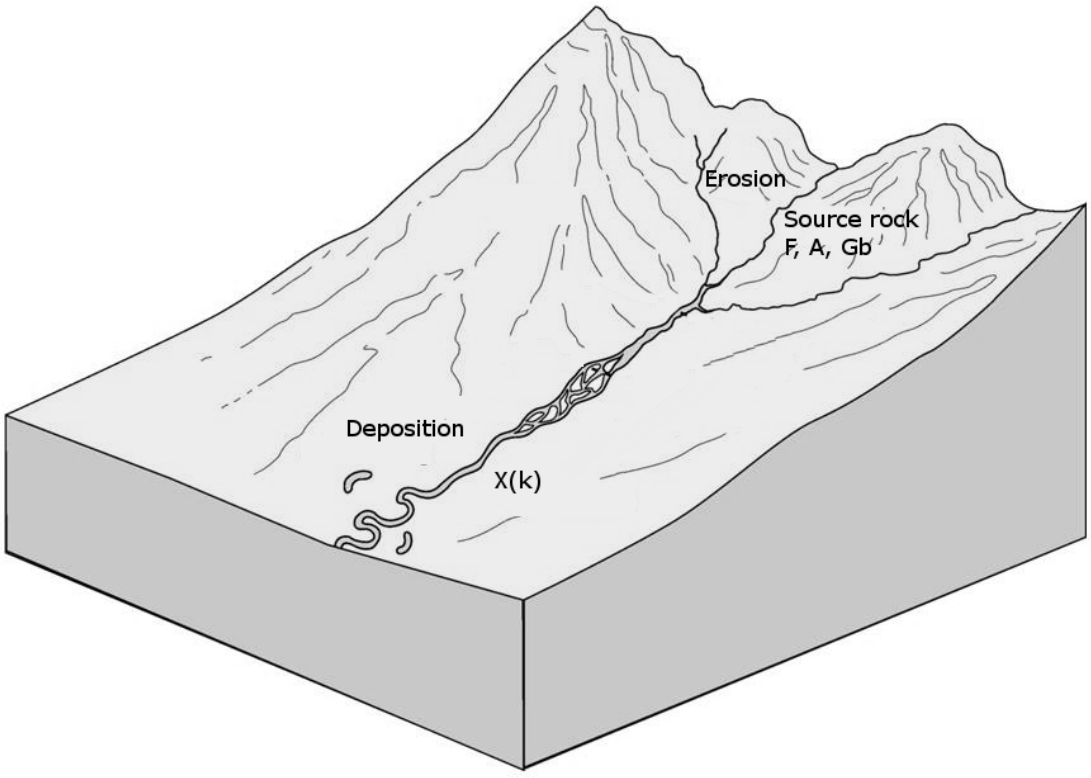

FIGURE 4.1: Selective sorting in a fluvial system. The variation within samples $X(k)$ decreases further away from the source. Figure modified from (Nichols, 2009)

The mineralogy per grain size class of the initial composition varies with the source the sediment originated from (provenance). Provenance is described by a $[m \times n]$ matrix F, every row vector in this matrix represents the type and proportion of the mineral present in a grain size class. The sum of every row vector equals one. The bulk grain size distribution of the sediment is defined as a vector, to simplify notation the vector is expanded to a $[m \times m]$ diagonal matrix G_b. The grain size distribution weighed with the provenance matrix results in the initial composition of the sediment X_0:

$$X_0 = G_b F \tag{4.2}$$

This equation shows the model can only represent a single source or a homogeneous mixture of sediment sources. This is a simplification, in reality we will often find a basin infill to be a mixture of several sources. The concentration of elements K, U and Th can be calculated by multiplying the composition $X(k)$ with the $[m \times 3]$ activity matrix A. Where each row contains the concentration of K, U, Th of each mineral in the composition:

$$GR(k) = A^T X(k) \tag{4.3}$$

The $[3 \times p]$ matrix $GR(k)$ contains the concentration of the elements K [%], U [ppm], Th [ppm] per grain size class p. Summing over the grain classes results in the total element concentration of the composition at step k. The model does not take into account any changes to the chemical composition of the sediment after deposition. Chemical weathering can have a large impact on the concentration of K, U and Th.

4.1.1 Settling velocity

Settling velocity is an important parameter in geology, hydraulic equivalent grains have a similar behaviour and tend to accumulate at the same location when dispersed. This is often reflected as sorting in terms of grain size since parameters as density and shape tend to be similar between sedimentary particles. Fining upward trends are the most common grain size trend and occur for example when particles settle from suspension in stagnant water. Fining upward grain size trends can be observed in various depositional environments, for example in fluvial systems, delta plains or overbank floodings.

Settling velocity is defined as the velocity reached when the net forces acting on a particle are zero: the upward acting buoyancy and drag forces are equal to the downward acting gravitational force. Particle density, shape, size and fluid viscosity are important

parameters affecting the balance between these forces. Due to the complex interaction of these parameters, the settling velocity is often determined with empirical models. In this thesis we use the model by Wu and Wang (2006), this model is valid over a large range of particle sizes and takes into account the effect of particle shape. The equation used is:

$$\omega_s = \frac{M\nu}{Nd}\left[\sqrt{\frac{1}{4} + (\frac{4N}{3M^2}D_*^3)^{1/n}} - \frac{1}{2}\right]^n \tag{4.4}$$

Where ω_s is the settling velocity, M, N and n are coefficients which are a function of the Corey shape factor S_f.

$$M = 53.5e^{-0.65S_f}; N = 5.65e^{-2.5S_f}; n = 0.7 + 0.9S_f \tag{4.5}$$

The Corey shape factor is defined as:

$$S_f = \frac{D_s}{\sqrt{D_i D_l}} \tag{4.6}$$

Where D_x refers to one of three axis of a grain approximated as an ellipsoid: the long D_l, intermediate D_i and short axis D_s.

D_* in equation 4.4 represents the effective weight of the particle and is defined as:

$$D_* = d\left[(\frac{\rho_s}{\rho} - 1)\frac{g}{\nu^2}\right]^{1/3} \tag{4.7}$$

Where $d = \sqrt[3]{D_l D_i D_s}$ represents the nominal diameter of the particle (Wu and Wang, 2006).

Throughout these formulae we see a great dependence on grain shape. Different grain shapes can lead to substantial differences in settling velocities. Micaceous minerals are a common group of minerals where grain shape tends to deviate from a 'spherical grain' the shape tends to be a platy, elongated shape. The effect on settling velocity is substantial: the settling velocity of sand sized platy micas are comparable to silt or clay sized near spherical sediment grains (Komar et al., 1984). In the model we therefore define two shapes which are assumed to be representative in most cases:

1. Natural worn sediment (roughly spherical) where $D_l \geq D_i \geq D_s$.
2. Mica shaped particles (plate shaped) where $D_l \geq D_i \gg D_s$.

The matrix W is the collection of settling velocities for all minerals and grain sizes in the composition, calculated with these equations. Figure 4.2 shows a comparison of settling velocities calculated with these formulas compared to settling velocities determined by (Komar et al., 1984).

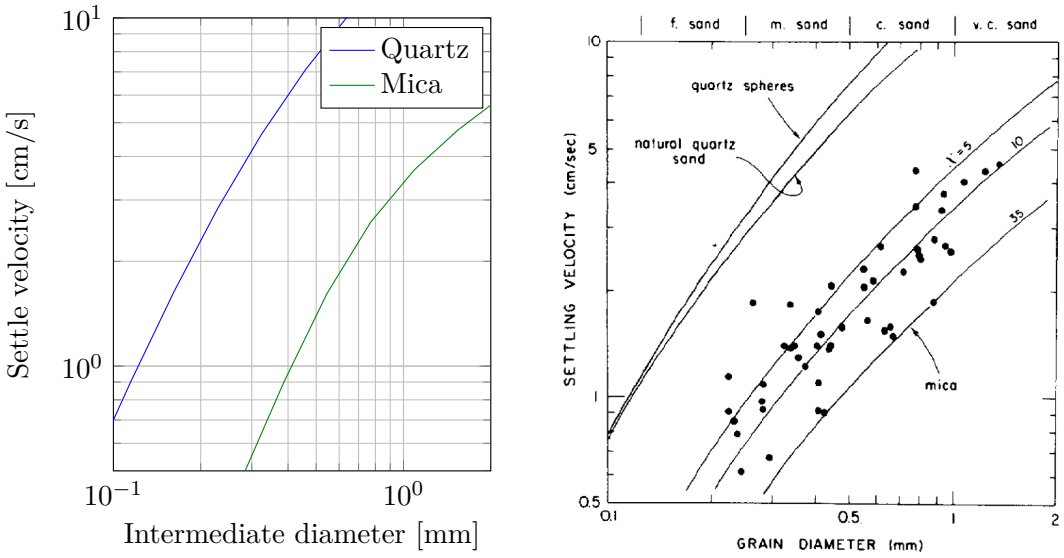

FIGURE 4.2: Comparison of results using relations from Wu and Wang (2006) (left image) and the results presented in Komar et al. (1984) (right image). The quartz line by Komar et al. (1984) is theoretically derived, the dots are experimental settling velocities data from mica with different flatness ratios with the solid line representing the fit through the data points. The results are very similar.

4.2 Application to two sediment sources

The forward model allows us to predict the gamma-ray signature of selectively dispersed grains as a function of sediment source. In this section we will construct two datasets representing sediment from two distinct source rocks: granitic and low grade metamorphic and model the gamma-ray signature of the two datasets.

The synthetic datasets are compiled based on data from Palomares Herranz et al. (1990) in their analysis of modern sediment from the Madrid Basin in central Spain. A large number of samples was sieved to construct grain size distribution, the mesh size ranged from 1 to 0.062 mm, with sieve class interval of 1ϕ unit. In each sieve class the heavy mineral fraction and framework grains were point counted and weighed. The two provenance matrices F are based on this data. A few assumptions had to be made to complete the dataset:

1. The sieve class interval was reduced to 0.5ϕ units by linear interpolation between the existing sieve classes.

2. Very fine sand to clay sized particles (4ϕ - 8ϕ) are not taken into account by Palomares Herranz et al. (1990). These grain size classes are added. It is assumed there are only clay minerals (Illite, Smectite and Kaolinite) present in the 8 ϕ grain size class. The fraction of other minerals is assumed to decrease linearly from 4ϕ.

The provenance or matrix F of the two synthetic datasets (see Appendix A) has been summarized in figure 4.3. The main difference in mineralogy is the higher fraction of K-feldspar in the granitoid dataset. In addition, the granitoid dataset contains small amounts of the radio-active Zircon, not present in the metamorphic dataset.

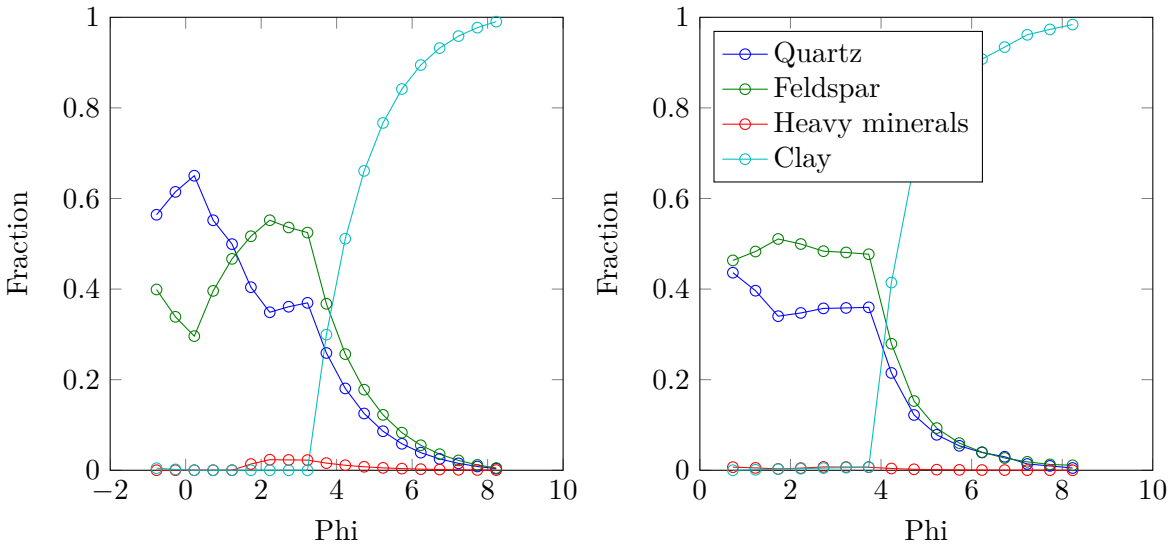

FIGURE 4.3: Left figure metamorphic dataset. Right figure granitoid dataset.

To determine the settling velocities of the minerals an accurate description of the dimensions of the grains are needed. Sieve analysis only sorts grains to its intermediate diameter (D_i) but the sieving process is not accurate because 1) the shape of grains often deviate from (the assumed) perfect spherical shape and 2) experiments have shown that some grains will not end up at their corresponding sieve due to the finite time of sieving or screen imperfections (Komar and Cui, 1985; Weltje, 2014). Both factors cause a systematic error, Weltje (2014) created a statistical model to compensate for these effects, his findings can be summarized as follows: The intermediate diameters of a grain can be approximated by a φ-normal distribution with median (m) and φ_k as the k-th sieve in ϕ units. For natural worn sediment the median value is $m_\varphi = \varphi_k - 1/8$ for micas the median value is $m_\varphi = \varphi_k - 5/8$. The corrections are used to compensate the intermediate diameters extracted from the sieve measurements. The short and long axis of the sediment particles are calculated from the Corey shape factor. We assume $D_i = D_l$ and calculate the short diameter by rewriting equation 4.6 to $D_s = D_{i=l}Sf$ such that the grains shape is reflected in the settling velocity.

4.2.1 Gamma-ray signature and provenance

The bulk grain size distribution is assumed to be equal for both datasets and was assumed to have a log-normal distribution with mean of 4 phi and a standard deviation of 2.5 phi units. Figure 4.4 shows the result of the modelled compositional trend. The initial, unsorted composition of the granitoid dataset is displayed at $k = 0$. After each step k the variation in the sediment decreases. For very small k-values the model approaches a situation with only one clay mineral present as the proportion of minerals with an higher settling velocity decreases. This is an unrealistic effect and sufficiently large k-values should be chosen to prevent 'over'-sorting.

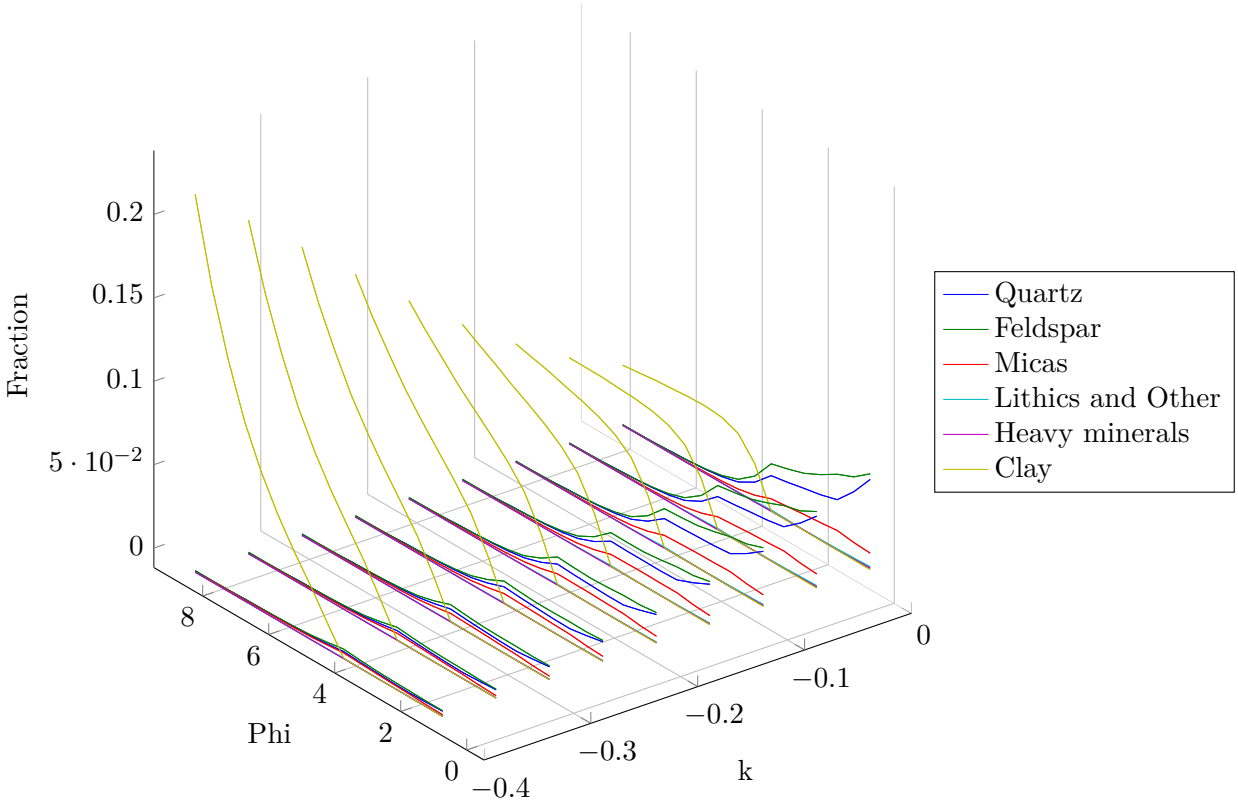

FIGURE 4.4: The composition of the matrix X at each step k. The sediment sorts from its initial composition X_0 to a composition with almost exclusively clay minerals (lowest settling velocity)

.

Figure 4.5 shows the proportion of K, U and Th for the two datasets, as a path in log-ratio space and as a standard spectral gamma-ray log. The mineral activities have been set according to the average values listed in table 2.1. Figure 4.5 shows a considerable difference in potassium content for large k-values which is mainly caused by the higher K-feldspar content in the granitoid sample, the contribution of K-feldspar to the K signal in sand sized particles is 40% to 60%. In the silt to clay fraction the main contributor to K are clay minerals. For all k-values the contribution to Th and U are mica's and

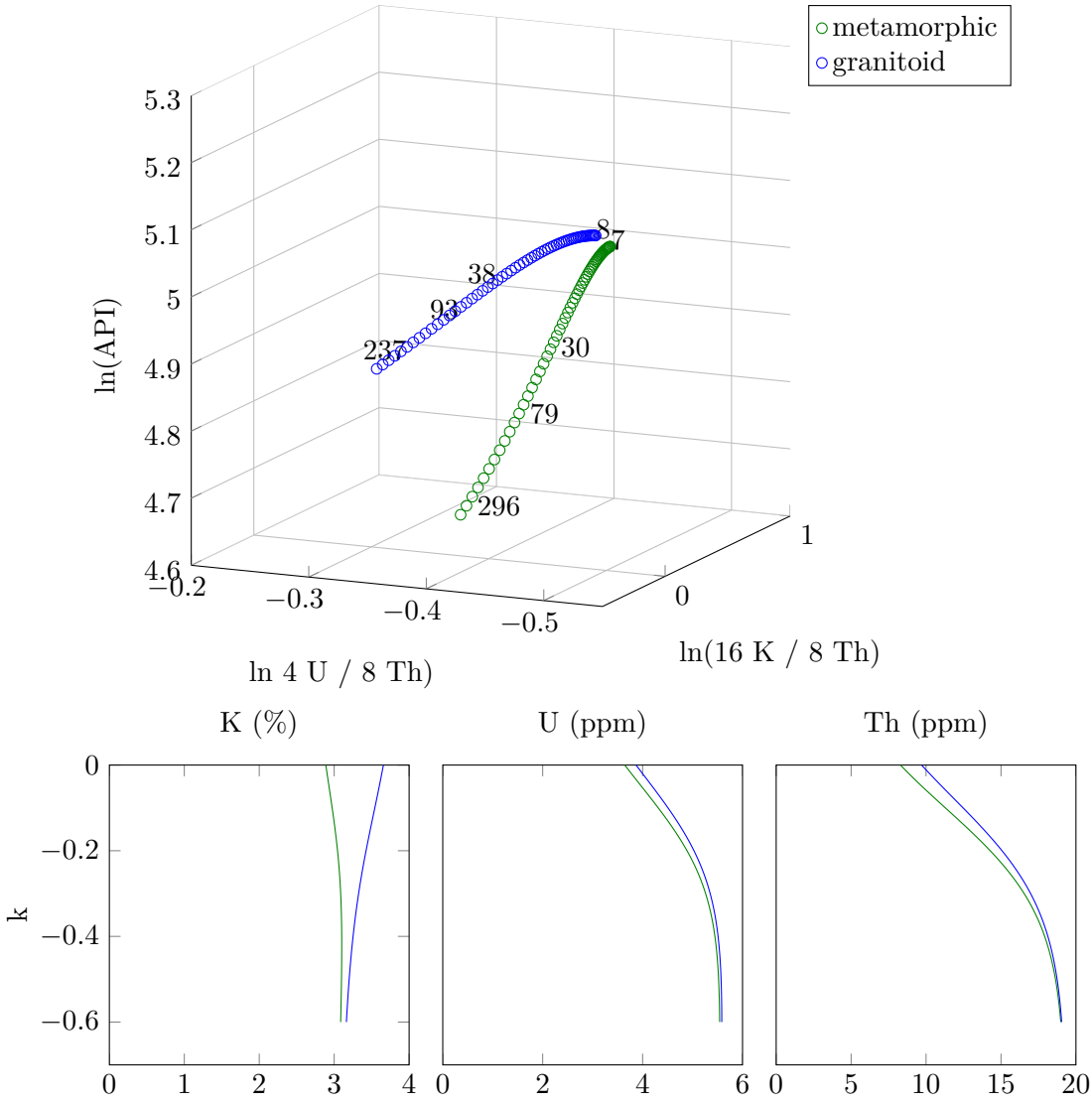

FIGURE 4.5: Path in log-ratio space of the granitoid and metamorphic dataset. The labels indicated in the plot at the top indicate the d_{50} at each sorting step.

clay and to lesser extend heavy minerals. Since the minerals carrying U and Th in the two datasets are very similar, their signature is almost the same. The difference in heavy mineral content between the two datasets does not result in a higher radio-activity due to their low proportions. The contribution of heavy minerals is around 10% to U and Th. In reality a more significant change in the gamma-ray signature is expected, the provenance of the sedimentary rock will not only be reflected by a difference in sediment composition but will also be reflected by different values of K,U and Th per mineral group. The relative importance of the mineral composition and radio-nuclide concentrations will be treated in the next section.

4.2.2 Sensitivity

Sensitivity analysis is performed to quantify the effect of parameter uncertainty on the outcome of the model. There are two important input parameters with a high degree of uncertainty: the radio-nuclide concentration (A) and the initial sediment composition (X_0). Both parameters have to be estimated or determined by measurements. Radio-nuclide concentrations of minerals show a large spread (see table 2.1) and exact determination of radio-activity is complex/expensive. Sediment composition can be determined by point counting or estimated but will always contain a sampling error. The effects of these uncertainties will be examined by introducing an error on the mineral proportions X_0 and varying the radio-activity of the minerals (A) keeping all other parameters constant.

1. The mineral activities are assumed to follow a normal distribution with mean value the mean of the range listed in table 2.1. The minimum and maximum are assumed to be three standard deviations away from the mean, such that probability of a drawing a number outside this range is almost zero.
2. Effect of a sampling error on the composition (X_0). The noise is modelled as a normal distribution in clr-space: $clr(\hat{X}_0) = clr(X_0) + clr(clrinv((N(0, \sigma^2)))$. The standard deviation is set based on the variation of the minerals within the grain size classes of the initial composition f.e. the proportion of clay and quartz varies considerably in the grain size classes and here we expect a large sampling error.

The sensitivity analysis is performed to give some idea of the order of magnitude of both parameters on the output, it is not a thorough analysis and based on a few assumptions and simplifications. Moreover, the sensitivity analysis is based on the granitoid synthetic dataset, it is obvious the variability of the gamma-ray signature depends on the ratio in which K, U and Th are present, which is different for every dataset. The first simplification is the proportion of radio-nuclides and minerals increases or decreases simultaneously. Secondly, the standard deviations in both cases are chosen somewhat arbitrary as the exact limits of uncertainty are hard to define. The limits found in literature on the radio-nuclide concentrations are likely to be good indications of the ranges we can expect but are no guarantee the values will stay within the reported ranges. Random counting errors on compositional data are often based on goodness of fit criteria such as Pearson's chi squared statistic (Weltje, 2004) where sample size is an essential parameter in the assessment. The standard deviation is chosen such that the composition does not change significantly and remains within 10% of the initial value. Since statistical parameters are unknown these assumptions are considered reasonable to give an idea of the order of magnitude of each parameter.

To quantify the magnitude of change of the output, the base case (P50 value) is compared to two cases: the lower P10 and upper P90 bound at 10% probability of occurrence. Because shape is an import feature of gamma-ray we will use the distance between equal d_{50} values to quantify the effect of changes in shape. Figure 4.6 shows the effect of changing the mineral radio-activity (A) and the initial composition X_0.

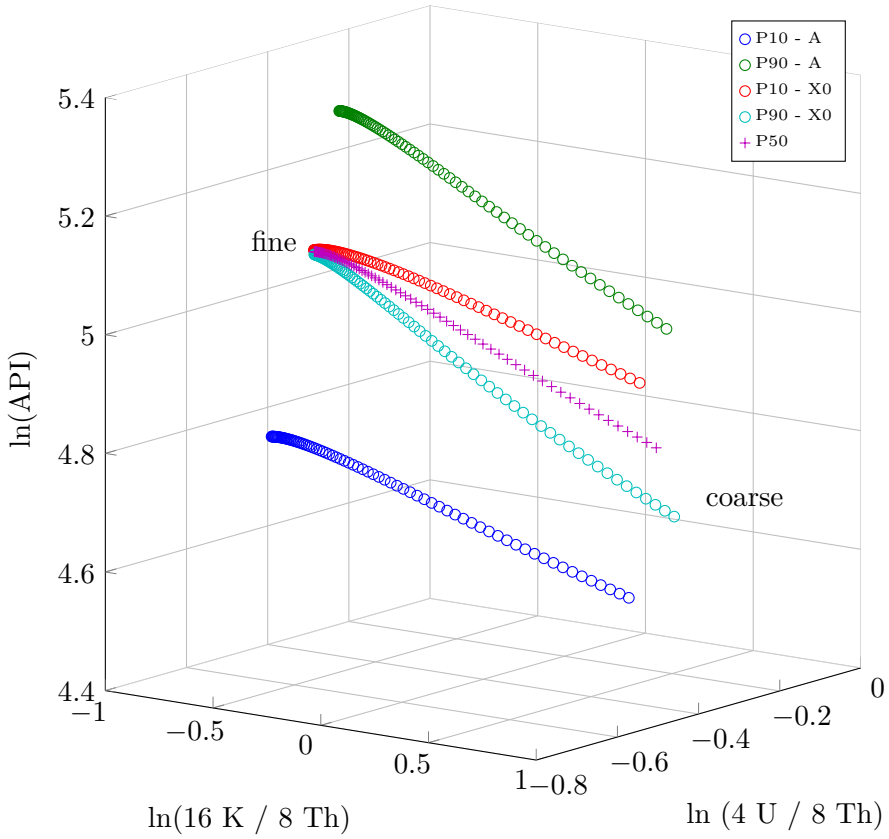

FIGURE 4.6: Variations in radio-nuclide concentrations, green and dark blue curve. Initial composition red and light blue curves. The P10 and P90 case refer to upper and lower bounds of occurrence with respect to the base case (P50) under the assumption the uncertainty is normal distributed.

The results indicate that the mineral radio-activity seems to contribute far more than the proportion of minerals present and is the largest source of uncertainty when predicting a gamma-ray signature.

4.3 Iterative model

Iterative forward modelling can be applied to fit the forward curve to an observed gamma-ray curve and infer model parameters like sediment composition or mineral radio-nuclide concentrations. With only 3 independent variables (K, U, Th) and many unknowns the problem is likely to be underdetermined with many solutions. The number of solutions is reduced by minimizing an objective function and applying a number

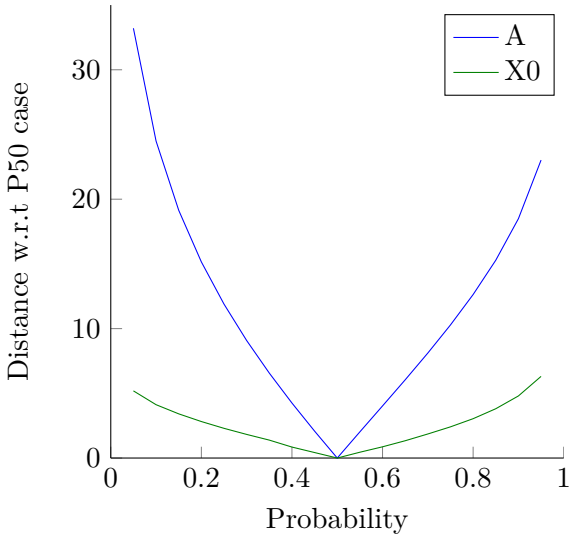

FIGURE 4.7: Distance between equal d_{50} points for the radio-nuclide concentrations (blue) and initial composition (green).

of constraints. The objective function is defined as:

$$min \sum (x - x^*)^2 + (y - y^*)^2 + (z - z^*)^2 \tag{4.8}$$

Where x, y, z is the log ratio of K/Th, U/Th and the log of the gamma-ray in API units of the input data respectively. x^*, y^*, z^* are the fitted values predicted by the forward model. The squared loss is computed between datapoints with a matching grain size (d_{50}). The model assumes all variations in the fitted parameters can be attributed to selective transport. In practice however we are likely to encounter noise which cannot be explained by the model. Sources of uncertainty may be structural or random. Structural uncertainty is introduced when for example sedimentary particles are not bound to a single mode of transport. Different transport modes may show different sorting patterns as different sediment properties become dominant. In a fluvial system for instance after settling sediment could be transported by rolling or saltation (bedload) where ease of sliding or rolling becomes the dominant parameter (Blatt et al., 1980).

The optimization problem is solved using the Nelder-Mead simplex method. The Nelder-Mead method uses a simplex with $n + 1$ vertices for a n dimensional problem and computes the function values at each vertex. The best value at each iteration step is chosen and according to a set of rules the simplex reflects, expands and contracts to a (local) minimum, see Lagarias et al. (1998) for more details concerning the mathematics of the routine. Constraints on the parameters can be set to ensure feasible parameters. The constraints on the radio-nuclide concentrations are defined as the lower and upper bound of radio-nuclide concentration found in literature. Additionally, multiple optimization cycles with randomly selected initial values are run to prevent the algorithm to be 'stuck'

in a local minimum. The best solution with the lowest residual sum is selected from all obtained solutions.

4.3.1 Application to synthetic dataset

The iterative model is applied to a synthetic gamma-ray signature produced from the granitoid dataset, the goal is to estimate the radio-nuclide concentrations from the gamma-ray signature and test the reliability of the model when noise is introduced. The sediment shows a fining upward grain size trend where the coarse fraction consists mainly of quartz and feldspar and the fraction of the clay minerals in the smallest grain size class. Initial d_{50} is 640 μm and sorts to final composition with dominantly clay minerals d_{50} 25 μm. The following errors are introduced:

1. The spectral gamma-ray response is perturbed by noise.
2. The grain size distribution is perturbed by noise, i.e. the initial composition contains a sampling error.

The noise of the gamma-ray response is modelled with a normal distribution. The grain size distribution (see figure 4.8)is log-normal distributed: for the original dataset μ =1.5 and σ =1 for the perturbed grain size distribution μ =1.7 and σ =1.5. The slight deviation in grain size distribution will introduce a small error by changing the initial composition of the sediment (X_0). These errors will be translated in radio-nuclide concentrations.

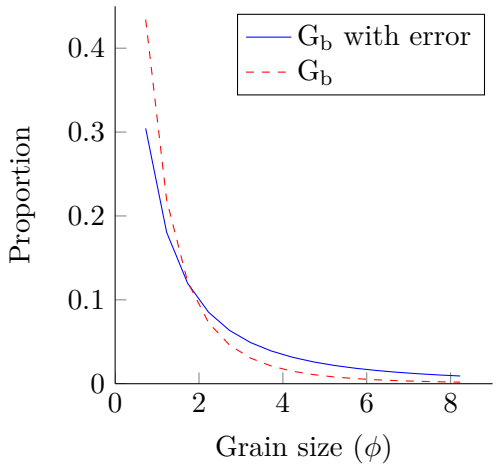

FIGURE 4.8: The grain size distribution used to generate the synthetic data (dashed red) and the grain size distribution used for the fit (solid blue).

The fitting procedure can only resolve the mineral radio-activity if minerals exist in an unique grain size class, for example the radio-activity in the clay fraction cannot be

attributed to different clay minerals. The number of minerals is therefore restricted to the most important gamma-ray carriers in each grain size class: K-Feldspar, Micas (biotite and muscovite) and clay minerals (chlorite, smectite, illite, kaolinite). The solution and fit is shown in figure 4.9.

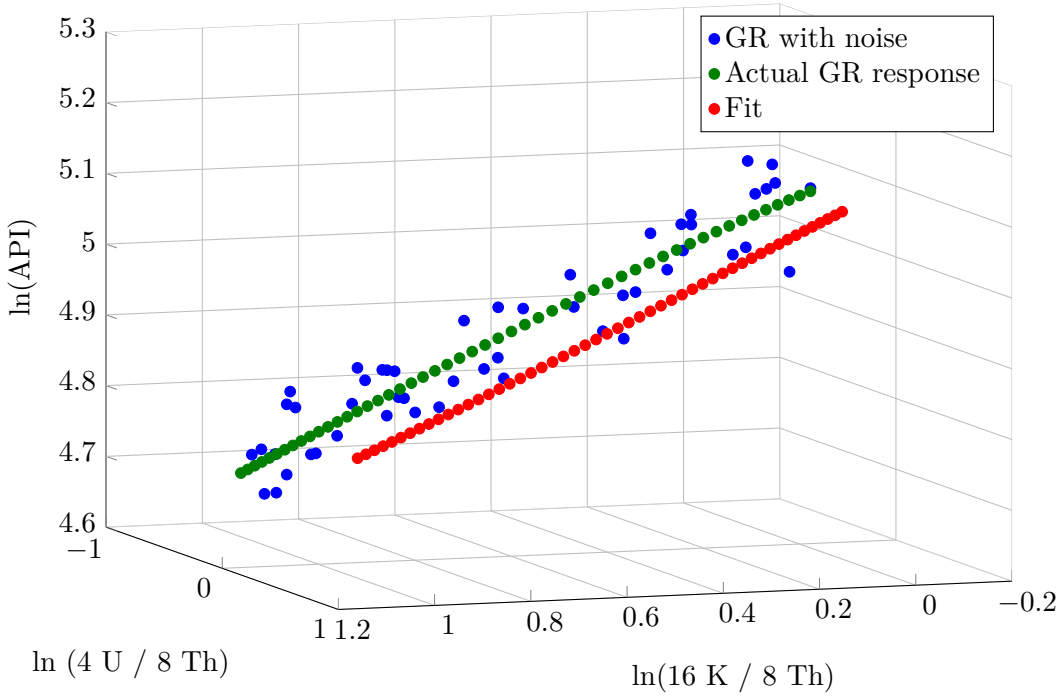

FIGURE 4.9: Noise perturbed gamma-ray response used as input (blue), noise free gamma-ray response (green) and the obtained fit with the lowest residual sum after five cycles (red).

The resulting radio-nuclide concentrations are given in table 4.1. Most values are reasonably close to the original input values, but some values show (very) large discrepancies for example the K concentration in the mica's. The introduced noise is seems to translate in large errors in the prediction of the radio-nuclide concentrations of the minerals.

	Obtained values			Actual values		
Mineral	K (%)	U (ppm)	Th (ppm)	K (%)	U (ppm)	Th (ppm)
K-Feldspar	10.4	0.8	11.4	14.0	1.4	5.0
Micas	57.6	28.9	20.1	16.9	25.5	47.5
Clay	44.0	16.6	59.5	36.3	17.0	62.5

TABLE 4.1: Comparison of obtained concentration of radio-nuclides with actual used model parameters.

4.4 Discussion and conclusion

The goal of this chapter was:

Can we simulate the gamma-ray response of selectively dispersed sediment?

We successfully constructed a forward model which is able to predict gamma-ray patterns of sediment subjected to size selective sorting. The sorting of the sediment is based on the settling velocity of the particles and predicts gamma-ray patterns as function of mineral composition and concentration of radio-nuclides. The model illustrates the variables involved in the relationship between the gamma-ray signature and grain size.The model is based on the assumption that the sorting process can be adequately modelled with a compositional linear trend. This assumption is not validated in this chapter. Diagenesis and mixing of sediment sources are not taken into account.

The sensitivity analysis on the synthetic data showed the radio-nuclide concentration is likely to be the most important parameter, within the range of radio-nuclide concentrations commonly observed in minerals this parameter has the largest impact on the gamma-ray signature. Iterative forward modelling can be used to reconstruct properties of the source rock. A constrained Nelder-Mead search algorithm is used to find the closest fit. The inverse model is applied to moderately noisy synthetic data, the first results suggest that the inverse model is very sensitive to the noise introduced on the synthetic data.

Chapter 5

Reconstruction of the gamma-ray log from grain size

In chapter 4 we constructed a forward model which simulates a gamma-ray signature of selectively dispersed sediment. The usability of this model may be limited, for example inverse modelling may fail because the problem is under determined or due to the large noise present in the gamma-ray log. In this chapter we take another approach and directly determine the gamma-ray signatures of a grain size (facies) class from core plug samples. Sediment within a (sufficiently small) grain size class are expected to be deposited under similar hydraulic conditions and therefore have a comparable (chemical) composition if there is no variation in provenance or diagenesis. If this condition holds, the gamma-ray log can be reconstructed from a (high resolution) grain size record. However, the limited vertical resolution of the gamma-ray log should be taken into account. In this chapter a forward model is constructed to account for the effect of the detector. The forward model is applied to the E10-3 dataset with the aim of reconstructing the gamma-ray log from the facies (or grain size) interpretation. The main goal of this chapter is:

Can we derive information from the residual gamma-ray signal if the variation caused by selective transport is minimized?

5.1 Modelling approach

The vertical resolution of the gamma-ray log is around 0.6m - 0.9m, depending on the length of the detector and formation properties (Serra, 1988). Well logging tools with a poor vertical resolution such as the natural gamma-ray tool will not have an instant

response to sharp bed boundaries. The response will gradually reach the true formation value, a so called 'shoulder effect'. Similarly the gamma-ray response to multiple thin bed boundaries (below the vertical resolution) will 'mix' in varying proportions, depending on the formations K, U and Th values within the sampled volume. The detector response A to a horizontally layered formation G is distorted by coefficients in C, the vertical response function:

$$A = GC \tag{5.1}$$

The $1 \times m$ vector G is the formation divided in m homogeneous horizontal layers with a specified height. Each layer m in G represents a facies or grain size class and is assigned corresponding values of radio-activity (K, U, Th) in Becquerel (Bq) per kilogram. The detector is positioned in the center of the vertical borehole and is modelled as a line with an height of 25cm. The $m \times n$ matrix with vertical response coefficients C defines the relative contributions of each gridblock m to the total radio-activity A $(1 \times n)$ as measured by the detector. The detector moves through the grid in discrete steps n where the step size can be chosen to represent the speed of the detector moving along the formation. The size of the sampled volume from which the photons are able to reach the detector depend on attenuation effects in the formation and the borehole. In this model only attenuation effects in the formation are considered, attenuation effects of the borehole, in the detector and potentially casing are neglected.

5.1.1 Vertical response function

The vertical response coefficients define the contribution of each gridblock to the final detector reading (i.e the contribution as function of distance from the detector). During the logging operation the detector travels with a predefined speed, a balance between a sufficiently long time to built a reliable spectrum (the time constant) and speed of the operation. The logging speed should be set such that only a small distance is travelled within a time constant, if the logging speed is set to high the response will average over a too large rock volume. The logging speed also affects the shape of the response function. A point moving towards the detector will contribute more to the detectors reading because the volume is within the detectors sphere of influence longer, causing the peak of the response function to shift upwards. Figure 5.1 shows the effect of logging speed on the shape of the response function.

The effect of logging speed on the shape of the response function is usually small if the correct speed is chosen, the speed is usually set such that 30cm is logged within one

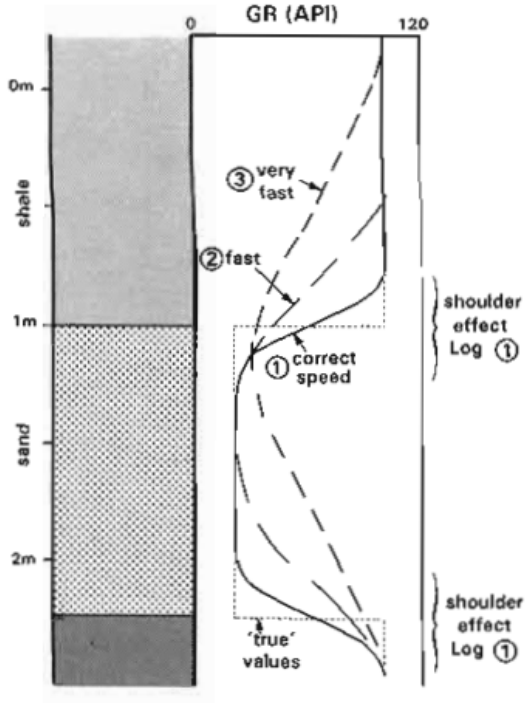

FIGURE 5.1: Change in shape of the vertical response as function of logging speed (Rider, 2002).

time constant (Rider, 2002). In the forward model, we assume the shape of the response function does not change as function of speed which corresponds to an infinite measurement time (time constant). In this case the response function is perfectly symmetrical: gridblocks close to the detector have an high contribution, the contribution decreases with distance due to gamma-ray interaction (see equation 2.4). By considering the attenuation in the formation an approximation of the response function can be obtained. The length in centimetres the flux decreases with a factor of $1/e$ is defined as the mean free path (λ):

$$\lambda = \frac{1}{\mu \rho_b} \tag{5.2}$$

Where λ is the mean free path in centimetres, μ is the mass attenuation coefficient as defined in Chapter 2 and ρ_b the density, assumed to be uniform 2.5 gr cm^{-3}. The mass attenuation coefficient is a function of photon energy and atomic number. For common elements in rock the mass attenuation can be considered roughly constant (Ellis, 2007) and is therefore only a function of photon energy. The mass attenuation coefficients for each radio-nuclide are listed in table 5.1. Ellis (2007) showed that the fraction of unscattered gamma-rays (the so called 'integrated geometric factor' $J(r)$) within radius r relative to the detector is proportional to:

$$J(r) = (1 - e^{-\frac{r}{\lambda}}) \tag{5.3}$$

With the listed mass attenuation coefficients and equation (5.2) the depth of investigation can be approximated. The depth of investigation is defined here as the point 90% of unscattered gamma-rays originate from.

Characteristic peak (MeV)	Mass attenuation (cm^2 g^{-1})	Depth of investigation (cm)
1.46 (K)	0.051	18.1
1.76 (U)	0.044	20.9
2.61 (Th)	0.036	25.5

TABLE 5.1: Mass attenuation coefficients (Hubbell, 1982) for common elements found in the subsurface as function of photon energy and their calculated depth of investigation.

The resulting response functions are shown in figure 5.2. In this figure the length of the horizontal part of the curve equals the detector length. Note that due to the cut-off value of 90% the contribution is not zero at the at the maximum distance.

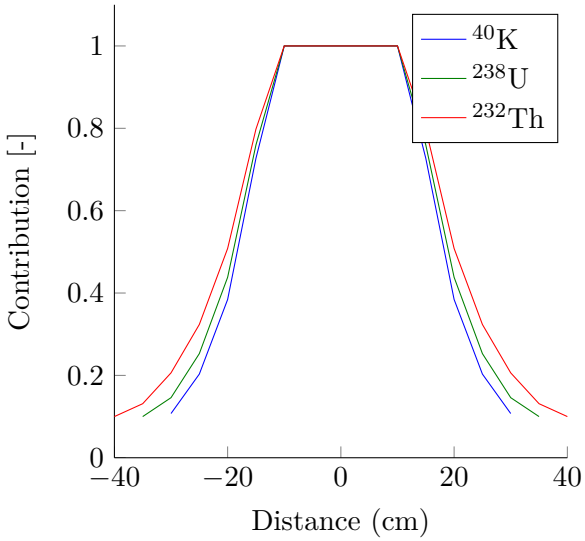

FIGURE 5.2: Response function for the radio-nuclides. Higher photon energies have a smaller probability of interaction with the formation consequently their sphere of influence is larger.

This approach is a simplification, usually we are dealing with an energy spectrum which is resolved into element concentrations.

5.2 Application to core E10-3

Core E10-3 is recovered from an offshore well drilled by Wintershall Noordzee. Panterra performed a complete analysis on the recovered core including spectral core gamma-ray,

petrophysical properties and sedimentology. Their findings are summarized in the report by Boels (2003). The core interpretation will be used to assign representative concentration of K, U and Th to each facies (grain size) class. The core plug response can be interpreted as the 'true' formation response without the degrading resolution effects (matrix G) if other variation on the gamma-ray response is negligible. The discrepancy between the recorded and modelled gamma-ray curve can give insights in the provenance and/or diagentic changes of rock.

5.2.1 Core description

Core E10-3 was recovered from a well situated in block E10-3 in the Dutch part of the North Sea. Two cores were recovered from a 73m interval at a depth of 3648m to 3720m. The sediment in core E10-3 were deposited in a deltaic system of (high energy) braided rivers with varying marine influence. The lithofacies association of the core can be summarized as follows Boels (2003):

- Upper (3650m - 3556m) and middle (3666m - 3698m) part of core and most dominant lithofacies association consists of bedload deposits of braided channels. Characterized by sandstones with a grain size ranging from pebbles to silt but mainly varying between upper fine to medium sand. Bed boundaries are erosive or scoured. Three channel units can be distinguished: Channel Unit 3: 3648m 3656m, Channel Unit 2: 3666m 3680m, Channel Unit 1: 3680m - 3698m.
- In between the braided channel deposits (3656m - 3666m) the recovered core consists of Crevasse splay and Interdistributary bay deposits. Crevasse splay is characterized by very fine grained sandstone beds with moderate amounts of carbonaceous matter and clay (5-35%). Interdistributary bay deposits contain claystones with silt and sand laminae.
- Lower part of the recovered core (3698m - 3720m) contains the Crevasse splay lithofacies association and poorly drained floodplain. The poorly drained floodplain is associated with claystones with regular coal laminae and organic matter. Other lithofacies associations in the lower part of the core are swamp and well drained floodplain but are minor in occurrence.

See table 5.2 for the textural properties associated to these depositional environments.

	M	**J**	**S1l**	**S1u**	**S2l**	**S2u**	**S3l**	**S3u**	**S4l**	**S4u**	**S5l**
Abundance (%)	26	7	5	11	12	14	15	9	1	1	0
Texture											
Mean grain size μ	6	31	74	105	149	210	297	420	595	841	1189
Mean sorting (1.3=good 2.35=poor)	1.6	1.1	1.5	1.7	1.7	1.7	1.9	1.7	2.0	2.2	2.4
Grain size abundance (%)											
Floodplain	0.8	2.6	-	-	-	-	-	-	-	-	-
Poorly drained floodplain	15.2	2.5	-	-	-	-	-	-	-	-	-
Swamp	3.2		-	-	-	-	-	-	-	-	-
Interdistributary bay	10.1	0.2	-	-	-	0.1	-	-	-	-	-
Crevasse splay	1.4	1.3	2.7	4.7	0.5	0.2	-	-	-	-	-
Braided channel complex	-	0.9	0.6	5.6	10.2	13.9	12.0	7.3	2.5	1.0	0.2

M	Mudstone	S3l	Medium lower sandstone
J	Siltstone	S3u	Medium upper sandstone
S1l	Very fine lower sandstone	S4l	Coarse lower sandstone
S1u	Very fine upper sandstone	S4u	Coarse upper sandstone
S2l	Fine lower sandstone	S5l	Very coarse lower sandstone
S2u	Fine upper sandstone		

TABLE 5.2: Textural characteristics for each depositional environment in core E10-3

5.2.2 Data acquisition and results

One to three core plugs were selected from each grain size class, depending on their abundance. Where possible homogeneous plugs were selected to represent the grain size class as closely as possible. The core plugs were analysed inside a lead shielded 3x3inch NaI detector at the Medusa office in Groningen, see figure 5.3. The core plugs are placed inside a foam cast to ensure the position of each coreplug on the detector is the same for each sample. The calibration of the detector was done using Monte-Carlo simulations, in the simulation the geometry and position of the core-plugs with respect to the detector are taken into account to derive the correction coefficients or 'standard spectra' (see equation 2.6). Despite the thick lead shield the count-rate from the background radiation due to either cosmic or environmental radiation resulted in roughly 10 counts per second. The count-rate of the samples were in some cases (on average) only a few tenths of a count per seconds higher than the background radiation, due to the low weight (<50 gram) and low activity of the samples. This resulted in extreme measurement times to acquire statistically acceptable results and the chosen measurement time of 24 hours per coreplug was not always sufficient. The raw spectra are analysed as follows:

1. The gain stabilisation coefficients are determined. This procedure shifts and widens

the peaks of the raw spectrum such that the channels correspond to the correct gamma-ray energy.

2. After stabilisation the background contribution is subtracted from the spectrum.

3. The resulting spectrum is analysed and the best fit of the standard spectra is determined by a least square algorithm.

An example of two recorded spectra are shown in figure 5.4. The figure shows a spectrum of a sample with very low radio-activity compared to a more radio-active sample. The low activity sample does not show a response other than background radiation and after the 24 hours of acquisition time and no accurate reading can be assigned to this sample.

FIGURE 5.3: Set-up for the core plug measurements. The detector is positioned at the bottom of the lead cylinder to reduce background radiation.

The results of the coreplug analysis are added in Appendix B. The table in the Appendix shows the radio-nuclide concentrations of the core plugs with their corresponding statistical counting error. The results of ^{40}K are the most accurate followed by ^{232}Th, the results of ^{238}U are mostly unreliable due to the poor fit of the standard spectra and resulted in negative values. The difference in accuracy of U compared to K and Th is caused by the more complex analysis of U. ^{238}U emits a large number of gamma-ray particles without a distinct photopeak, in contrast to ^{40}K and ^{232}Th. The fitting of the standard spectra for ^{238}U is therefore a lot more unreliable, resulting in non-physical results, for core plugs with a low radio-activity. The non-zero values of K, U and Th

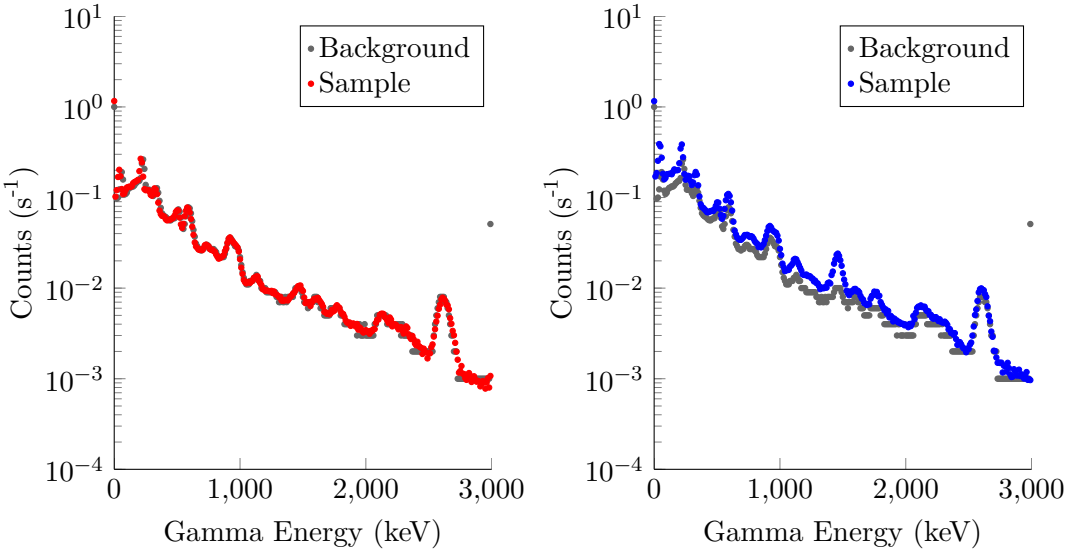

FIGURE 5.4: Left figure spectrum of sample with almost no activity, background spectrum perfectly overlays sample response. Right figure sample with a clear response.

are plotted in figure 5.5 together with their corresponding grain size classification. Error bars indicate the 68% confidence interval. The figure shows that the potassium and thorium content show a decreasing trend with decreasing grain size. The spread in potassium content between samples is small and within the statistical uncertainty of the measurement with the exception of the two siltstone (J) core plugs. The uranium content is unreliable due to the poor fit results and shows little relation between samples. The spread in thorium content is large between samples in equal grain size classes, with the exception of the lower sandstone class (S1l).

5.2.3 Reconstruction of the gamma-ray log

A representative gamma-ray signature of each grain size class is obtained by calculating the mean and variance of the core plugs. The previously reported counting error is neglected in this process. The assigned values are listed in table B.2. With the vertical response function the effect of the detector can be mimicked and should resemble the core gamma-ray curve if:

1. The response function is a good approximation for the averaging effect of the detector.
2. The mean and variance of K, U, Th are representative for the values observed in each grain size class.
3. The effects of provenance and diagenesis are constant.

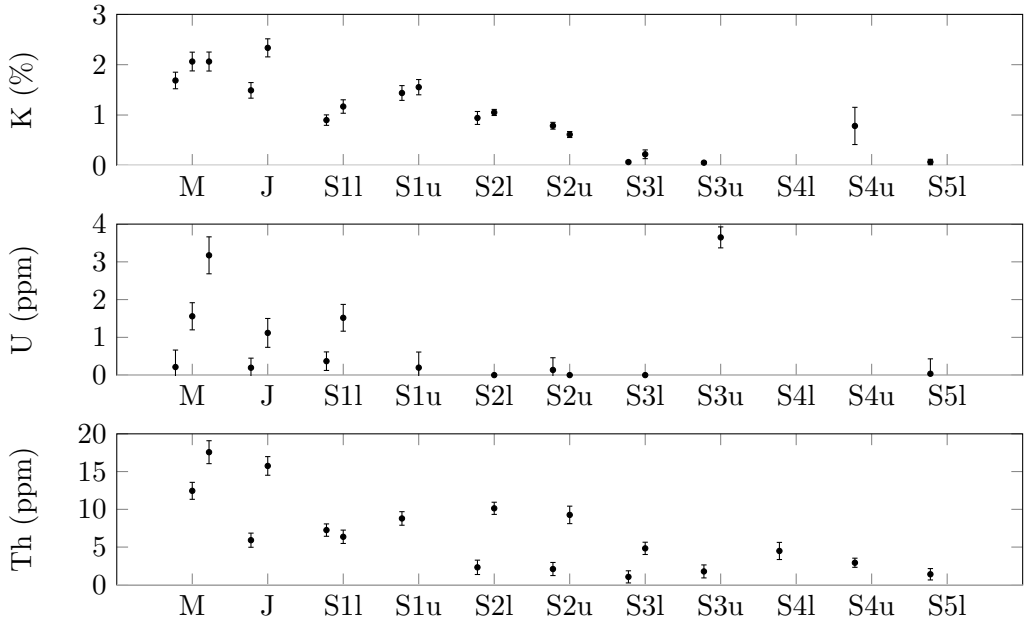

FIGURE 5.5: Results of the coreplug analysis. Grain size class on x-axis in descending order, with concentrations of K (top) U (middle) and Th (bottom).

The grain size data from core E10-3 was obtained from the core description by Boels (2003) and reported in intervals of 25 cm. The spectral gamma-ray data was obtained from the core and recorded every 10 cm. Figure 5.6 shows the result of the forward model. As expected, the modelled U response does not resemble the core gamma-ray due to the poor core-plug gamma-ray results. The modelled K and Th curves are a reasonable representation for the shape of the core gamma-ray but the concentrations throughout the grain size classes are systematically lower, with the exception of high activity samples in the M and J grain size class. The discrepancy is the highest in the low activity, coarse grained samples of the K and Th curve, this can be clearly seen in the response at the interval 3670m-3680m and 3685m-3695m (braided channel deposits). The disagreement between the modelled and recorded curves are therefore clearly related to data acquisition. An illustration of the effect of the response function is shown in figure 5.7. The formation blocked response is degraded into a smooth response. In most cases this appears to be an accurate approximation, for example the shoulder effect between the 3708m - 3707m is accurately predicted by the model.

5.2.4 Optimised fit

The systematic poor fit of the model and the core gamma-ray indicates the main reason for the large discrepancy between the predicted and recorded well log is related to the data acquisition. The low weight and consequently low activity of the samples complicates the measurement considerably.

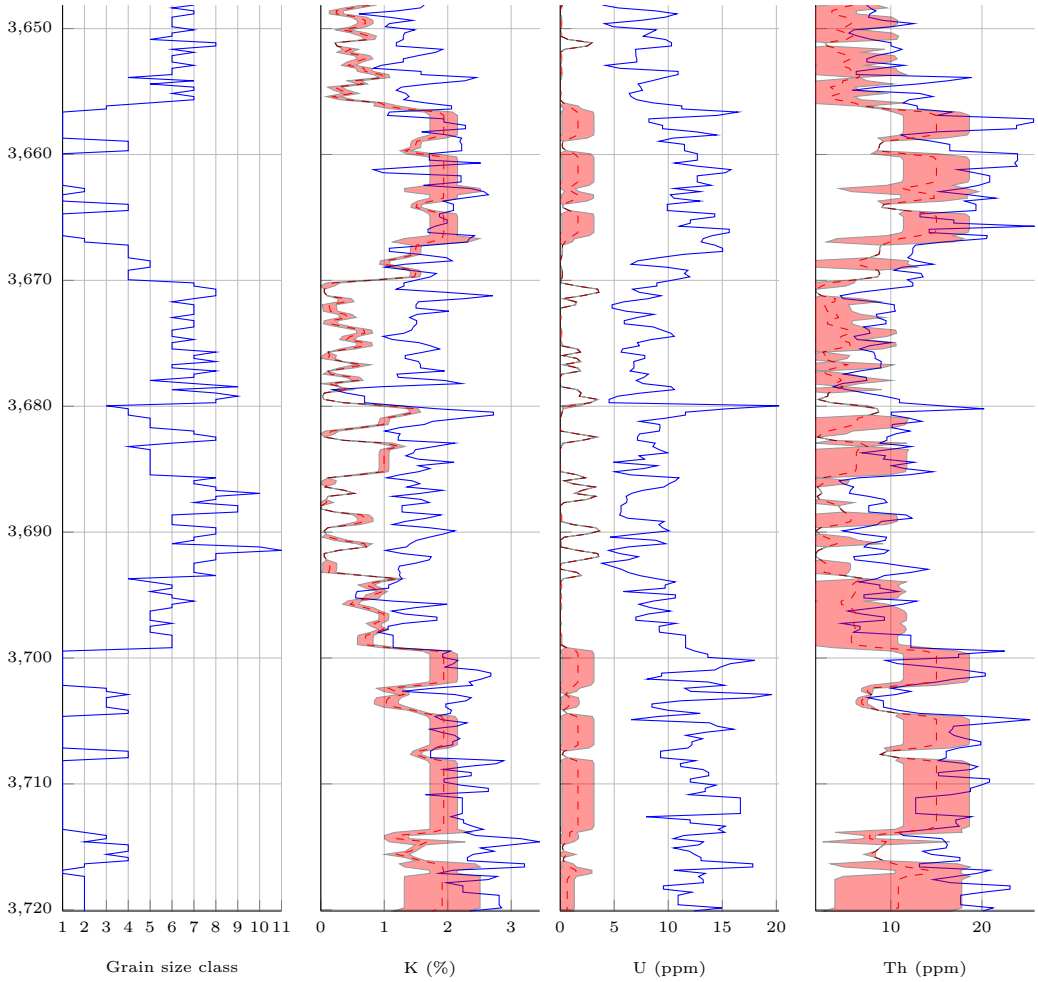

FIGURE 5.6: Left figure: grain size interpretation over the logged interval (Boels, 2003). Grain size codes refer to the following classes: 1=M 2=J 3=S1l 4=S1u 5=S2l 6=S2u 7=S3l 8=S3u 9=S4l 10=S4u 11=S5l. The remaining figures show the K, U and Th mean (dotted red curve) and variance (filled red) and the core gamma-ray (solid blue).

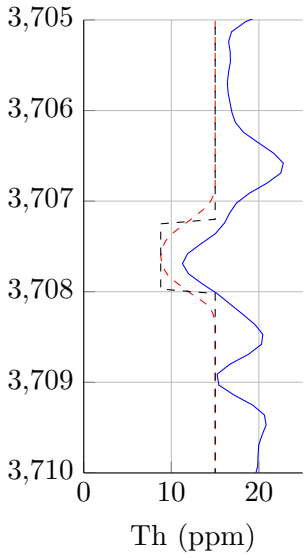

FIGURE 5.7: Effect of vertical response function for thorium.

Even if accurate results are obtained, differences between laboratory determined values and well logs are still observed (see for example Fabricius et al. (2003); Hurst (1990)) and attributed to the use of different detectors in different conditions (calibration, acquisition time, geometry). A large mismatch can be expected when comparing the values.

The Nelder-Mead algorithm can be used to find the most optimal radio-nuclide concentration for each grain size class. With the optimisation routine the squared distance between the model and the core gamma-ray is minimized using the same objective function as in chapter 4 (see equation 4.8). The number of grain size classes are reduced to 8 by merging the least abundant, coarse fraction (S3u, S4l, S4u and S5l) into one grain size class S4. The initial values used in the optimisation routine are the obtained coreplug activities, except for the potassium content in S4 set to 1% and the uranium content where the initial value is set ⅔ of the Th response. The result of the fit is reasonable (figure 5.8) and results in realistic K, U and Th values (figure 5.9). Occasionally the peaks of model are slightly shifted with respect to the core gamma-ray, these differences are probably caused by small inaccuracies in the depth alignment of the core-plugs and the core gamma-ray. The fit suggests a strong dependency of the gamma-ray signal with grain size, especially the thorium content. However there is still a large proportion residual variance, multiple sources could be responsible:

1. The poor resolution of the grain size record compared to the well log gamma-ray, thin beds cannot be reconstructed but might have a considerable contribution.

2. The poor sorting of the sediment on some intervals might cause a highly variable mineral composition. The poorest sorting is in the coarse grained braided channel deposits (see for example 3685m-3695m). Here large variations in the gamma-ray signature are present. However, analysis of the mineralogy (Boels, 2003) reveal an important gamma-ray carrier in this fraction is authigenic kaolinite which is be present in small amounts (about 10%).

3. The mudstone deposits show considerable variance in their gamma-ray signature. For example the interdistributary bay deposits (3656m - 3658m) show higher Th and lower K values than the poorly drained floodplain mudstone deposits (3709m - 3712m). This could be a residual effect of facies, for example presence of organic content.

4. Noise. For example changes in borehole geometry (wash-outs or position of the detector relative to the formation). Statistical counting error.

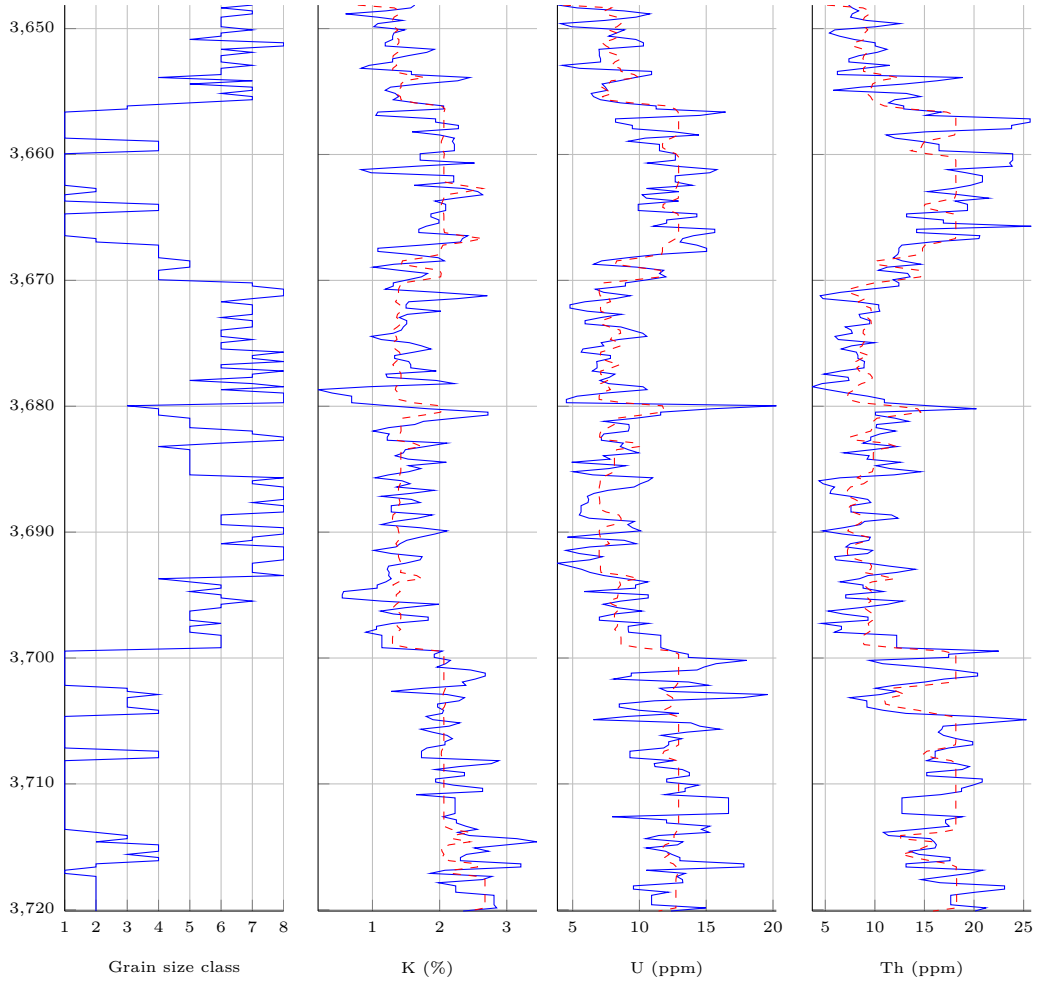

FIGURE 5.8: Left figure grain size interpretation over the logged interval (Boels, 2003). Grain size codes refer to the following classes: 1=M 2=J 3=S1l 4=S1u 5=S2l 6=S2u 7=S3l 8=S4. The remaining figures show the fit of the K, U and Th (dotted red curve).

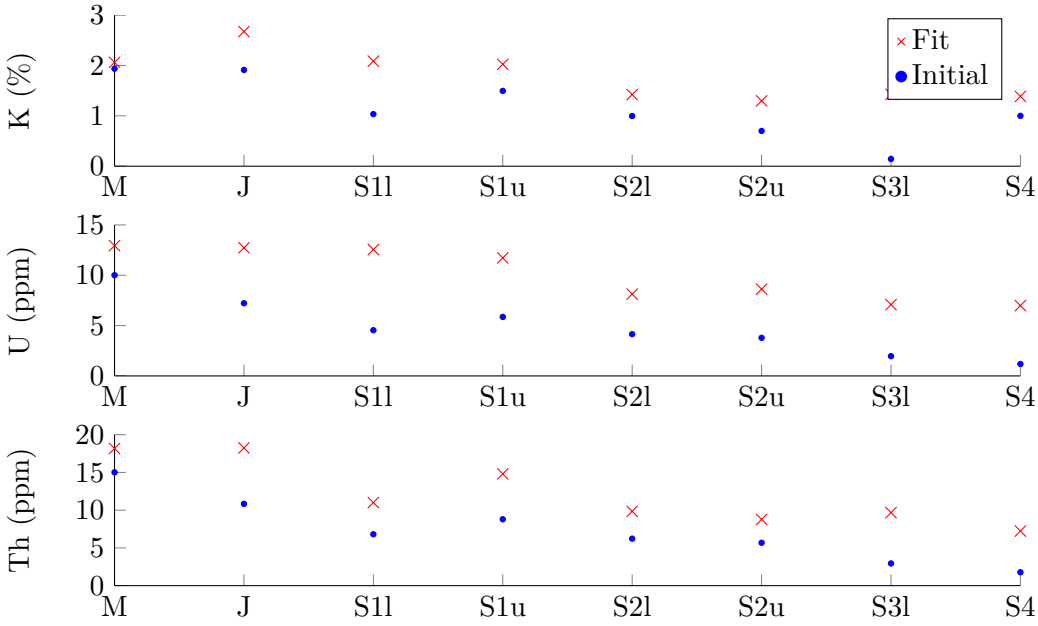

FIGURE 5.9: Initial and fitted values found for each grain size class.

5.2.5 High resolution grain size and gamma-ray

In this section an higher resolution grain size record is used to reconstruct the gamma-ray signal. The grain size classification is based on data from Bloemsma (2010) who used the color record from core images combined with geochemistry (XRF) as a proxy for grain size. Two models were applied to the data: the first model is a direct predictor of grain size using first order multi-variate regression (MVR). The second model is a categorical prediction using Bayesian theory where a probability is assigned to each grain size class. The grain size classification is obtained by multiplying the probability with the average grain size of the class (see table 5.2). In both cases the grain size is predicted in intervals of 1 cm, the core gamma-ray data is recorded in intervals of 10cm.

Comparison with low resolution grain size record

The model parameters are changed to match the resolution of the grain size and gamma-ray record: the layer height is set to 1cm, the stepsize of the detector is set to intervals of 10cm. The activities of the grain size classes are set to the initial K,U and Th core-plug values. Both the MVR and the Bayesian classification result in a better fit of the gamma-ray curve compared to the low resolution grain size record although the differences are small and still a large deviation is present, see figure 5.10. There is no considerable change in the shape of the gamma-ray curve but peaks are more pronounced due to the presence of thin, fine grained layers of more radio-active rock. The difference between the gamma-ray curves produced by the two grain size records is very small.

Optimisation

If we assume the gamma-ray signal is mainly a grain size signal, we can assess which high resolution grain size record is the most accurate based on the fit of the core gamma-ray with the gamma-ray curves produced from the MVR and the Bayesian grain size classification. The Nelder-Mead optimisation algorithm is applied to both datasets with the same initial values used in the previous optimisation, the fit and the fitted activities are depicted in figure 5.11 and 5.12. Compared to the fit of the low resolution grain size record the result shows moderate improvements, there is more detail present in the gamma-ray curve but still the optimisation tends to result in a smooth, average of the core gamma-ray without a close match. Based on the fit and the resulting activities per grain size class no decisive conclusion can be drawn with regards to which grain size record is a more accurate representation. The total residual sum favours the Bayesian grain size classification (8410 versus 8811) but this difference is small. The activities per grain size class, figure 5.12 are mostly comparable to the optimisation results for the low resolution grain size classification in the Bayesian case, the MVR fit results tend to be closer to the measured core-plug values.

Histograms of the discrepancies of K, U and Th per grain size class are attached in Appendix B for both grain size datasets. The histograms were fitted with a normal distribution, the standard deviation and mean of the fit is shown in the title above each histogram. In most cases the residuals are well described by a normal distribution.

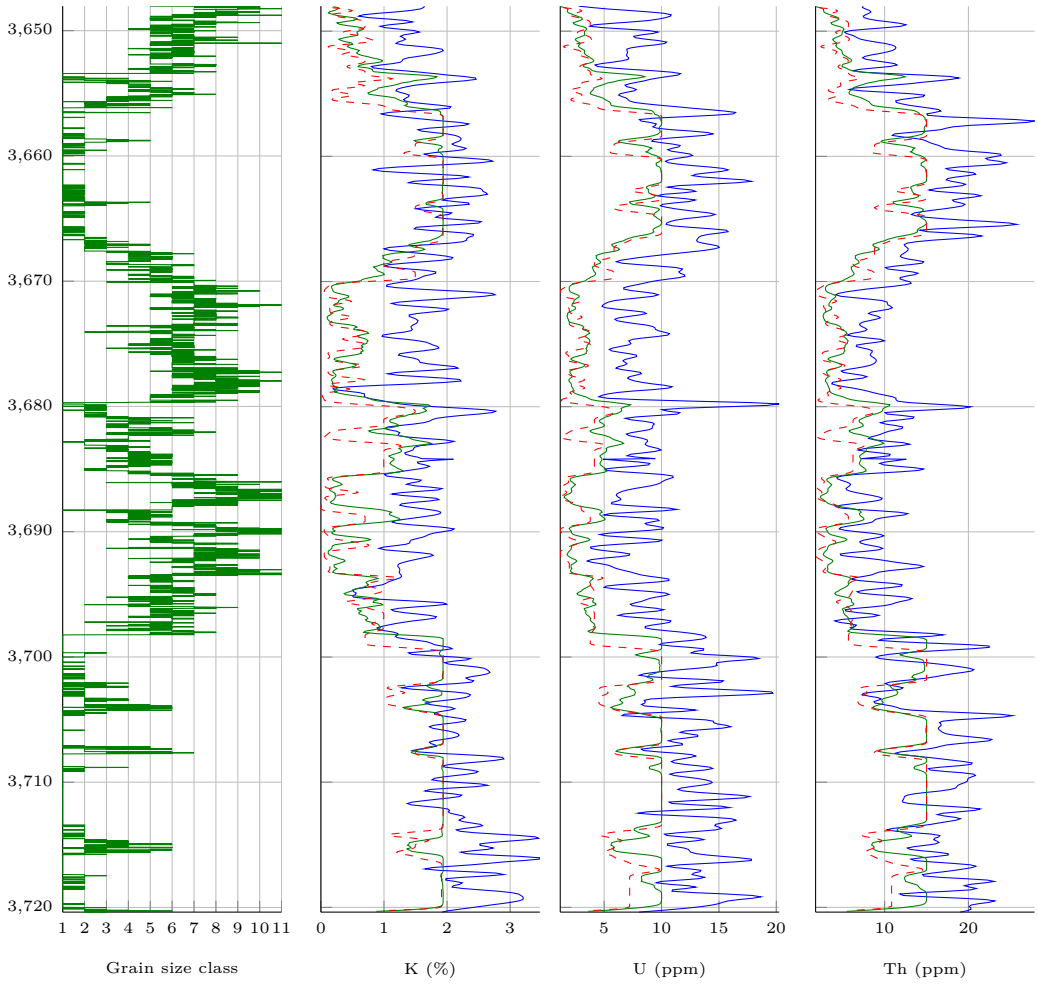

FIGURE 5.10: Left figure high resolution grain size interpretation (MVR) (Bloemsma, 2010). Grain size codes refer to the following classes: 1=M 2=J 3=S1l 4=S1u 5=S2l 6=S2u 7=S3l 8=S3u 9=S4l 10=S4u 11=S5l. The remaining figures show the GR produced from the low resolution grain size (dashed red) and GR produced from the high resolution grain size record (solid green).

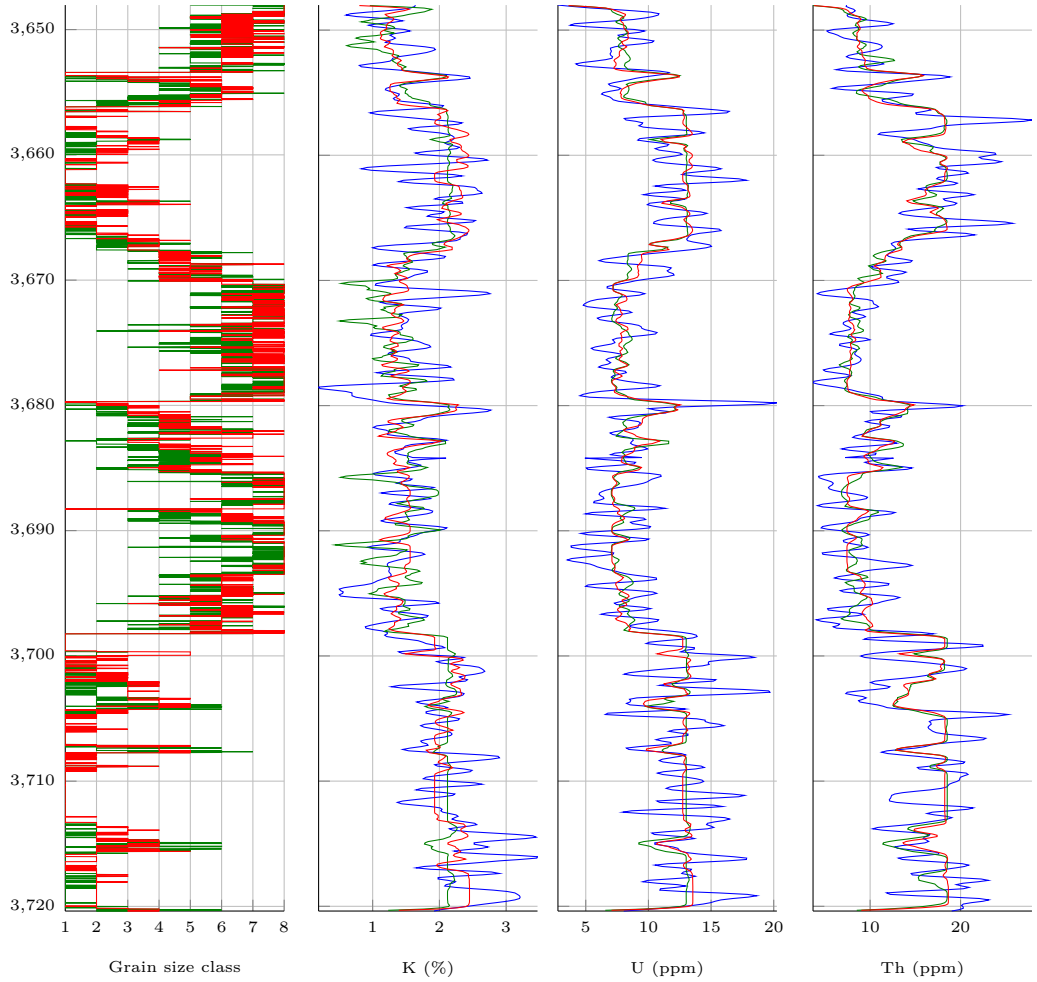

FIGURE 5.11: Left figure grain size interpretation MVR (green) and Bayesian (red) over the logged interval (Bloemsma, 2010). Grain size codes refer to the following classes: 1=M 2=J 3=S1l 4=S1u 5=S2l 6=S2u 7=S3l 8=S4. The remaining figures show the fit of the K, U and Th for the MVR model (green) and the Bayesian model(red).

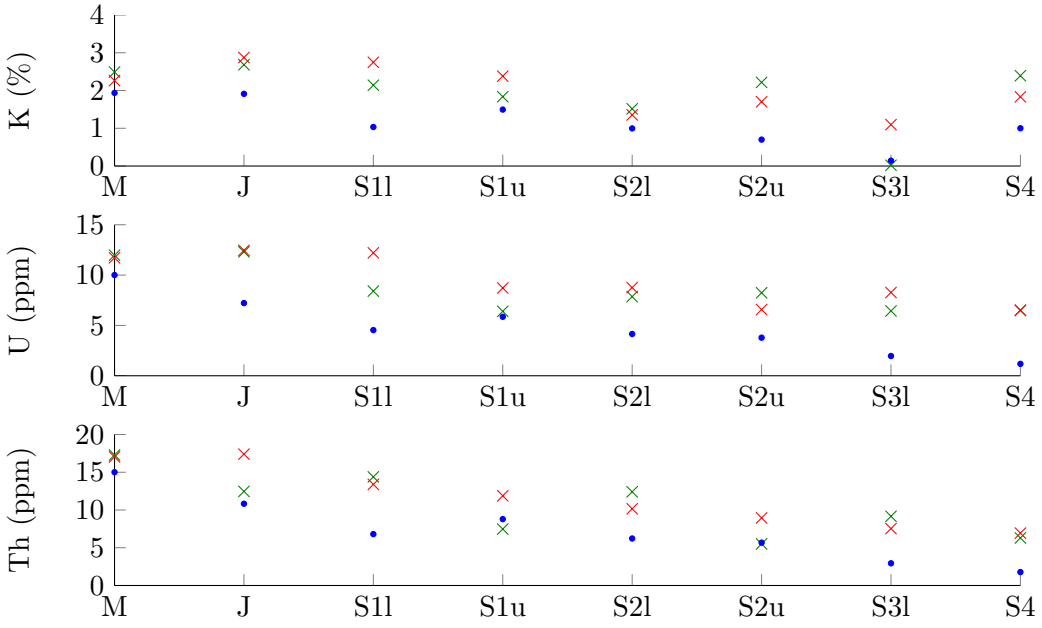

FIGURE 5.12: Initial measured coreplug activities (blue) and fit results for the MVR (green) and Bayesian (red) dataset.

5.3 Inverse model

The approach used in the previous chapters to obtain high resolution gamma-ray using core plug activities has a few drawbacks. In a standard lead shielded detector the measurement time is long and the results are poor when dealing with core plugs with low activities. The second drawback is heterogeneity on the plug scale could result in unrepresentative values for a grain size (facies) class and a large number of sample should be sampled to get an idea of the variance within the classes. A different approach using core gamma-ray is suggested here which can be integrated in the core analysis routine without the need for additional equipment. In this section the method of acquiring higher resolution gamma-ray will be discussed and tested on synthetic data.

5.3.1 Approach

To obtain high vertical resolution core gamma-ray it is suggested to decrease the logging speed such that consecutive points are sampled repeatedly. The similarity or autocorrelation between datapoints can be used to extract the higher resolution gamma-ray values. The forward model presented in equation 5.1 can be rewritten to:

$$G = C^{-1}A^T \tag{5.4}$$

Where A is the acquired spectral gamma-ray log, a vector with n measurement points. C is the matrix with vertical response coefficients. The vector A contains the $m \times 1$ vector G in its convolved form due to the averaging effect of the detector. In theory if $m = n$ and A is free of any noise this results in a perfectly deconvolved signal. In reality however we will be dealing with finite measurement time (i.e. a detector moving with a predefined speed) which has two effects on the measurements A, it introduces noise and reduces the number of observations. In other words, the problem becomes increasingly underdetermined ($m > n$) with increasing logging speed. In this case, the inverse of C can only be approximated, the Moore Pseudoinverse is used in this section to give an approximation of the solution in the least-squares error sense. When noise is present in the measured data however a least-square estimate will give poor results and magnify measurements errors. Regularisation methods are therefore used to add some form of bias to the solution and reduce noise effects. In this section the performance of this method will be assessed and the trade-off between noise and resolution will be evaluated. A synthetic dataset is used such that the exact input is known and can be compared to the model results.

5.3.2 Moore-Penrose pseudoinverse

A pseudo inverse can be used to compute the solution of a system with no unique solution. The solution of the pseudo inverse is special because the norm of the solution vector is minimized, in this case the expression: $||GC - A||^2$ is minimized. One way to determine the pseudo-inverse is using a Singular Value Decomposition, which is convenient because important information concerning the solution can be deducted from the decomposed matrices. A singular value decomposition factorizes a matrix into three matrices:

$$C = USV^T \tag{5.5}$$

U and V are orthogonal matrices e.g. $UU^T = I, VV^T = I$ and of unit length (orthonormal). S is the diagonalised matrix containing the so called singular values (σ): the non-negative square root of the eigenvalues (Golub and Reinsch, 1970) in descending order. An intuitive way of looking at the decomposition in the case C is square is in terms of transformations. Matrices U and V are rotation matrices and S is a scaling matrix. The condition number of the matrix (a rough estimate for the stability of the solution) follows directly from the decomposition by $cond(C) = \sigma_1/\sigma_n$ (Hansen, 1994). The condition number indicates the sensitivity of the solution to small changes in the input and therefore the response of the solution to noise. The pseudoinverse of C can easily be determined from the Single Value Decomposition:

$$C^+ = US^+V^T \tag{5.6}$$

Where C^+ denotes the pseudoinverse. The inverse of the diagonal matrix S is simply the reciprocal of the non-zero entries of the singular values.

5.3.3 Regularization

To deal with noise, inherently present in gamma-ray data, two methods are used:

- Truncated SVD (TSVD)
- Tikhonov regularisation

Truncated SVD

By omitting singular values some of the variance associated to measurement errors is

omitted by setting very small singular values to zero. The condition number of the matrix decreases therefore resulting in a solution less sensitive to noise. However, the increase in the stability results in a decrease in resolution, a general trade-off which is always observed (Menke, 2012). We take a simple approach and only truncate the SVD if a large drop is observed. Figure 5.13 shows the decay of the singular values for two cases, when h=5cm and h=10cm. For h=5cm there is a clear drop from 10^{-1} to 10^{-3}. The last singular value can be set to zero to improve the stability of the solution.

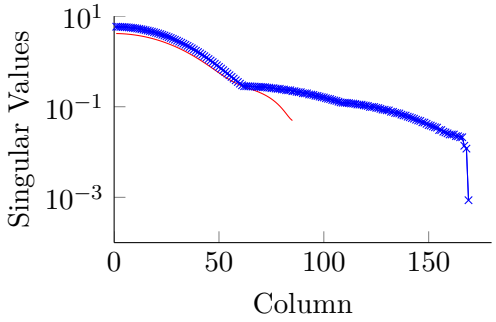

FIGURE 5.13: Decay of singular values of matrix C with stepsize h=5cm (blue) and h=10cm (red). The decay of S for h=5cm has a clear drop and is said to be rank deficient (numerically approximately linear dependent). For h=10cm the singular values decay gradually and the problem is ill-posed (Hansen, 1998).

Tikhonov regularization

Tikhonov regularization or damped least squares introduces a regularization term in the minimization:

$$||GC - A||^2 + ||\alpha IG||^2 \tag{5.7}$$

Where I is the identity matrix and α is the weight of the solution norm. For α equals zero this is equal to the ordinary least-squares solution. Increasing the weight of α will increase the residual norm $||GC - A||$ but as a result noise is damped (Hansen, 1994). The goal is to find a value such that noise is damped but an accurate solution is still obtained. The diagonal values of Tikhonov regularized solution are determined from the singular values using:

$$D_{ii} = \frac{\sigma_i^2}{\sigma_i^2 + \alpha^2} \tag{5.8}$$

And zero for all the off diagonal values. The filter factors dampens some of the last SVD components when $\sigma_i << \alpha$ while there is almost no effect to the singular values larger than α (Hansen, 1994). The same conclusion can be drawn from calculating the condition number. The higher resolution estimate $\hat{G}$ is equal to:

$$\hat{G} = UD^{-1}V^T A^T \tag{5.9}$$

Performance

Since we are using a synthetic dataset there is a direct way to measure the performance of the regularization parameters. The parameters are defined relative to an acceptable error, such they have the same order of magnitude. The measure for the goodness of fit is defined as the distance between the solution vector G and $\hat{G}$ over a specified interval:

$$gof = \frac{||\hat{G} - G||}{||cG||} \tag{5.10}$$

Where c is maximum defined error of the exact solution. The noise in the solution is defined as the variance of $\hat{G}$ scaled with the maximum allowed variance over the test interval:

$$noise = \frac{Var(\hat{G})}{\sigma^2_{max}} \tag{5.11}$$

The optimal solution is selected by minimizing the goodness of fit and the noise. The noise σ_{noise} is modelled following Gadekea et al. (1991) and is assumed to be normal distributed with zero mean and standard deviation proportional to the counts:

$$\sigma_{noise} = \frac{n}{\sqrt{counts}} \tag{5.12}$$

Where n is a constant representing the noise level. The equation simulates the behavior of the measurement error; intervals with low counts have a large uncertainty, high counts a small uncertainty.

5.3.4 Results on synthetic data

The following model parameters are used:

1. The gridblock height is 5cm.
2. The detector height is 15cm.
3. The vertical response function of the detector is assumed to be known and except for the detector length equal to figure 5.2.

The model is first tested on a noise free synthetic dataset. The synthetic data simulates an alternation of high and low radio-activity with increasing spacing, the layers are spaced 5, 10 and 20 cm apart with an interval of constant radio-activity between each section. The interval used to determine the performance of the model is the interval of constant radio-activity between 3.8 m and 4.8 m. The matrix A was sampled with three different logging speeds, noise perturbs the observations independent from the logging speed. First the detector stepsize is set equal to the grid height (5cm), in the other cases the detector stepsizes is set to 2 (10cm) and 3 (15cm) times the grid height.

Figure 5.14 shows the results, as expected in the first case the solution can be determined uniquely and results in a perfectly deconvolved signal, however the condition number of the matrix is very large. Although a lower condition number, the magnification of errors can be observed when comparing h=10 and h=15. Small noise effects are magnified in the second plot but more detail is present. In case the stepsize is increased detail is clearly lost and the thin beds cannot be reconstructed accurately from the observations. The small differences between between the response functions of each radio-nuclide also has an effect. K has the sharpest response function and as a result the inverse tends to cause larger oscillations. Without regularization and with noise present in the observations the amplification of the errors would make this method unusable, the most important task is therefore to assess which value for alpha gives the optimum noise suppression but maintains an increase in resolution.

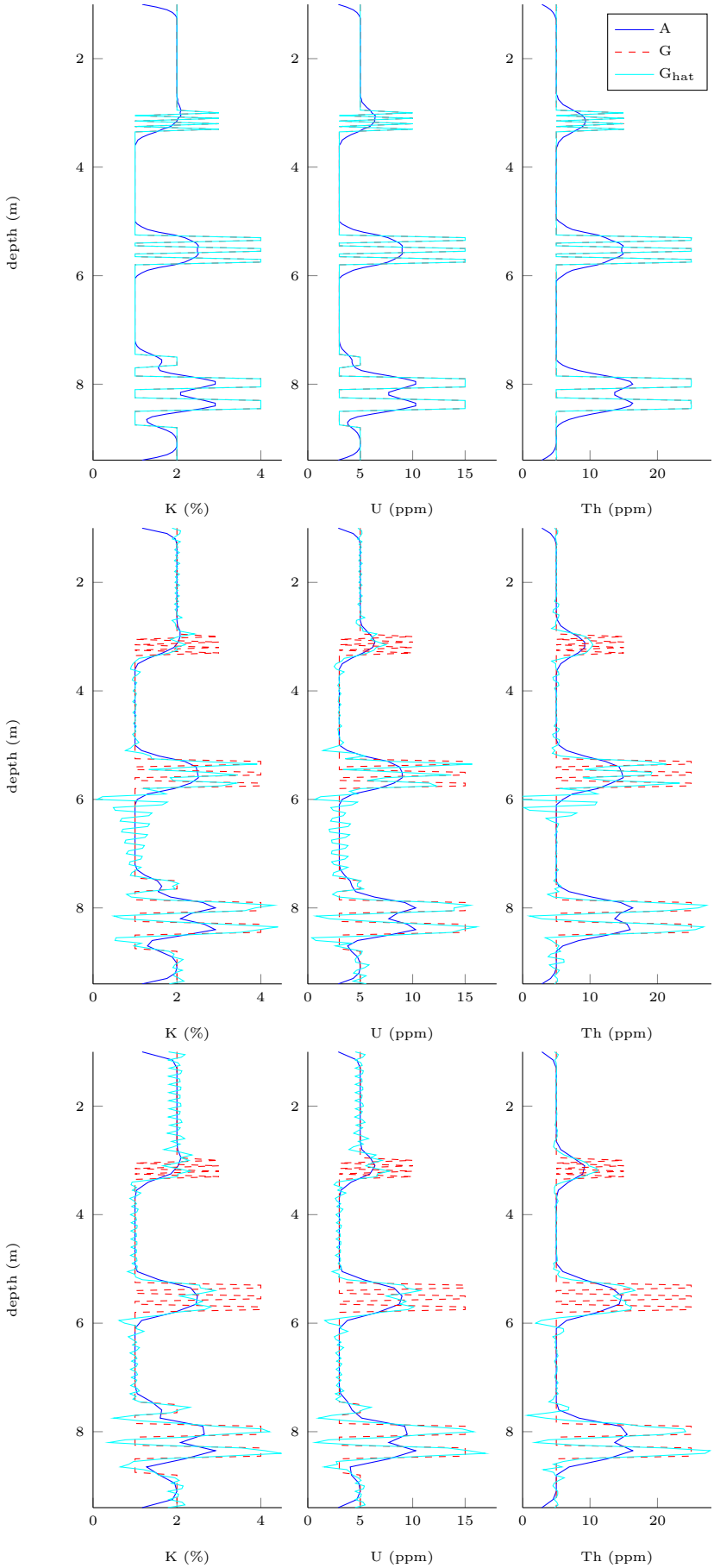

FIGURE 5.14: Effect of sampling with different detector speed: top figure h=5cm, middle h=10cm, bottom h=15cm. Observations A are noise free, no regularization i.e. α=0 and SVD matrix is not truncated.

Figure 5.15 shows the trade-off between noise and goodness of fit with increasing alpha in case 5% of noise, relative to the values on the test interval, are present in the observations. The values of alpha range between 0 - 3. For alpha is zero noise dominates the solution and the noise level is outside of the range of the plot. For alpha equal to 3 the noise is damped but deviation between the approximation and exact solution are very large. The plots only indicate the deviation or variance between the approximate and exact solution over the test interval.

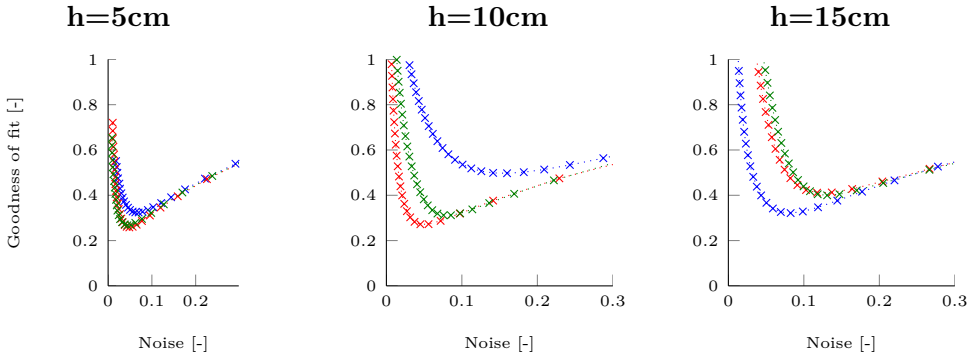

FIGURE 5.15: Trade-off between goodness of fit and noise, noise present in the observations is 5% for radio-nuclides: K (red), U (green) Th (blue).

The optimum of the regularisation parameter alpha can, when the solution is known, be obtained easily. The optimum solution for stepsize h=5cm and various levels of noise are depicted in figure 5.16. With noise levels around 15%, the optimum alpha factor is large and damps some of the noise. Only large noise oscillations are amplified. The resolution improvements are modest, beds of 15cm cannot be resolved from the logs but the procedure does in general not amplify the noise present. Of course, in case the solution is not known the choice for the regularization parameters is not straightforward. Several methods are commonly used such as cross-validation or restricted maximum likelihood. It was observed the noise levels between 5% - 15% do not cause the factor alpha to increase significantly (optimum values between 1.3 and 1.7) therefore another possibility could be finding optimum alpha values for a given noise level using a modelling approach.

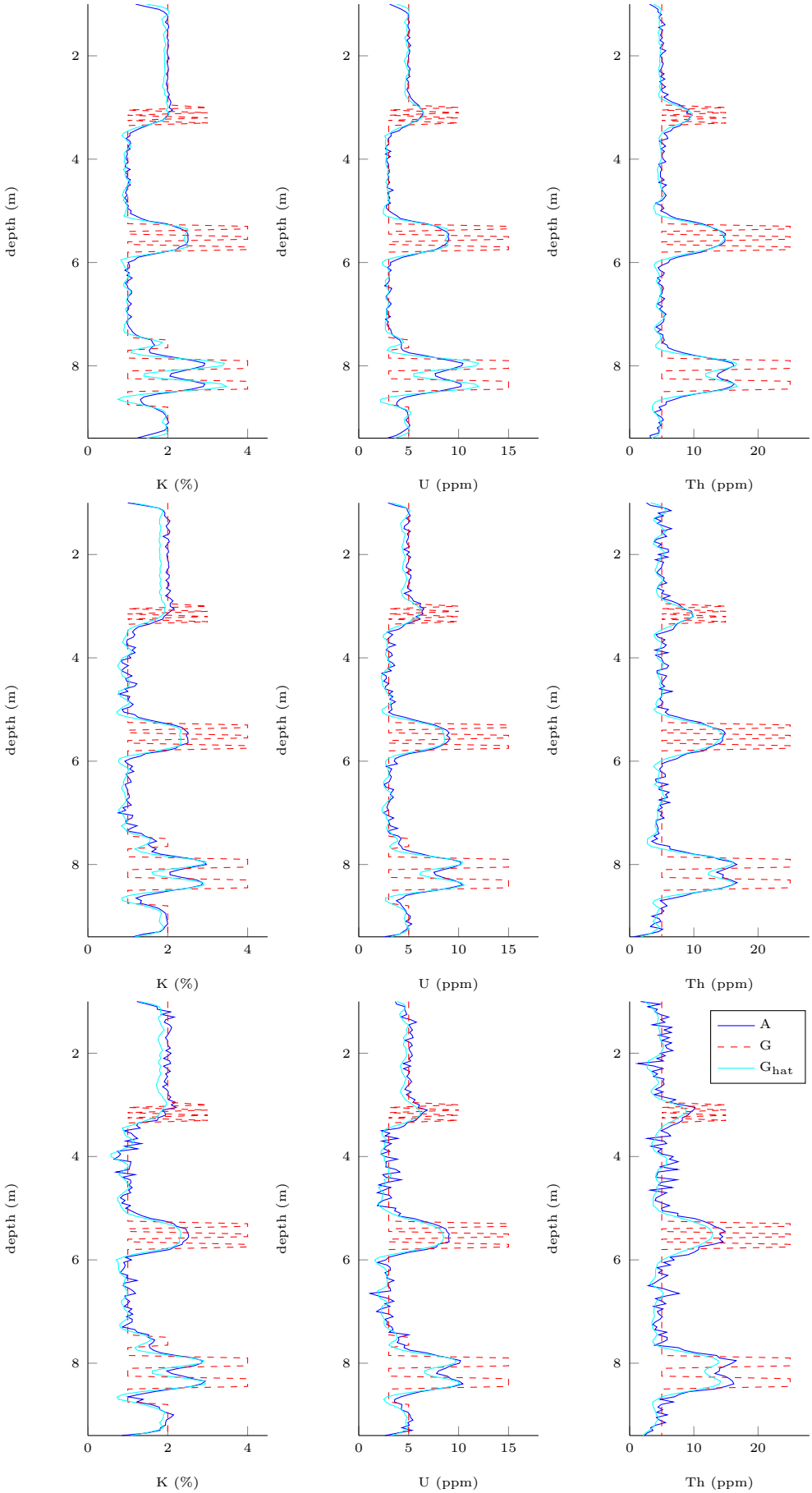

FIGURE 5.16: Optimum solution for h=5 and various noise levels: top figure 5%, middle 10% and bottom 15%. The SVD is truncated to 168 eigenvalues, optimum of alpha selected by minimizing the noise and goodness of fit parameter (varies between 1.3 and 1.7).

5.4 Discussion and conclusion

The main research question of this chapter is:

Can we derive information from the residual gamma-ray signal if the variation caused by selective transport is minimized?

In this chapter a forward model was constructed which simulates the averaging effect of the detector, with a grain size record and a gamma-ray signature derived from core plugs the gamma-ray well log of core E10-3 was reconstructed. By taking into account grain size, it is expected the largest variation in terms of size selective sorting minimized. The residual variance can (theoretically) be interpreted in terms of changes in provenance and diagenesis. There are however a lot of sources which could be responsible for the residual variability in the gamma-ray signal.

The initial fit of the model with the gamma-ray log was poor due to the poor results obtained from the core plug measurements, the weight and consequently the activity of the core-plugs is too small to derive accurate signatures from. With the Nelder-Mead optimisation algorithm a satisfactory K, U, Th signature for each grain size class was found (see table 5.3). The thorium content shows the strongest dependency with grain size probably due to its strong relation to clay minerals, both potassium and uranium show a comparable and poorer fit. Higher resolution grain size records derived from a grain size proxy (sampling interval of 1cm) resulted in a better fit with the well log gamma-ray, mainly due to the presence of thin beds of clay to silt sized particles invisible on the lower resolution grain size record. Mayor sources of residual variance in this case are expected to be related to degree of sorting, noise, differences related to the depositional environment such as organic content and diagenesis. Changes related to diagenesis are in this case, without additional information, hard to distinguish from the other sources of variance in the gamma-ray signal.

The high dependency on grain size in core E10-3 can be used to assess which grain size record, the MVR or the Bayesian classification, in the model produces the closest fit with the well log gamma-ray. The MVR and Bayesian dataset however, show a similar grain size classification and no clear conclusion can be drawn based on the core gamma-ray log. The core gamma-ray log is logged with an interval of 10cm versus a grain size record of 1cm, therefore the problem is likely to be underdetermined and the resolution of the gamma-ray too low to be decisive.

Due to the small volume of coreplugs, core-plug gamma-ray have proven to be unreliable. An alternative method is proposed in which the core gamma-ray is deconvolved to obtain an higher resolution gamma-ray log. A general inverse of the vertical response function of

	M	J	S1l	S1u	S2l	S2u	S3l	S4
Initial (meassured)	15.0	10.8	6.8	8.8	6.2	5.7	2.9	1.8
Fit low-res grain size	18.2	18.3	11.0	14.8	9.8	8.8	9.7	7.2
Fit high res MVR	17.2	12.5	14.4	7.5	12.4	5.5	9.2	6.3
Fit high res Bayesian	17.0	17.4	13.4	11.9	10.2	9.0	7.5	6.9

TABLE 5.3: Initial and fitted values for the thorium content in the facies classes of core E10-3 for each grain size record.

the detector can be used to deconvolve the observations to an higher resolution log. The results of the deconvolution on synthetic data only show modest resolution improvements but due to the use of regularization methods can suppress some of the noise. With 5% noise over the test interval layers of 10cm thickness cannot be resolved. A layer thickness of 20cm does show improvements at this noise level. A combination of decreasing the detector height and deconvolution could lead to better results. Simulations can be used to give an idea of the value of the regularization parameters at given noise levels.

Chapter 6

Application to Huesca core

In this chapter we will apply the theory and models of the preceding chapters to the dataset of the Huesca fluvial fan. A common depositional feature of the Huesca fluvial system are point bar deposits. On the sloping floor of a point bar fluid flow velocity gradually decreases and results in characteristic fining upward sequences. The deposits can be several meters in thickness. These features make the Huesca dataset a good candidate to test the usability of the size selective sorting model constructed in Chapter 4, the first goal of this chapter is:

Can we accurately model the gamma-ray signature of sediment subject to size selective sorting?

We will use this model in the interpretation in two ways and assess the results:

1. Forward prediction of the gamma-ray signature and assess if these match the well log.
2. Iteratively finding a fit with the well log gamma-ray by changing the concentration of radio-nuclides.

To simulate the gamma-ray signature with the selective transport model thin section from the point bar sequences were analysed to quantify the mineral composition. The predicted gamma-ray signatures are compared to the spectral gamma-ray well log.

In chapter 5 we used the grain size interpretation from the core analysis and saw that in this case the variation in grain size explains a large part of the variability in the gamma-ray signal and allows us to interpret the residual signal. Grain size or a facies description is, in this stage, usually not available but with a grain size proxy we can still apply this method. In this chapter the FMS log will be used to derive a grain size

record. We can again attempt to reconstruct the gamma-ray signature from this grain size proxy and assess if the residual signal provides us with additional information.

Can we derive information from the residual gamma-ray signal if the variation caused by selective transport is minimized?

6.1 Introduction

The Huesca fluvial fan located in the Ebro basin in Spain contains various fluvial deposits from a mixed-load fluvial system. The sediment originated from the Pyrenean Mountains and South Pyrenean foreland Basin and is of Olgocene to early Miocene age (Donselaar and Overeem, 2008). A common depositional feature of meandering rivers is the lateral accumulation of sediment on the inside of river bends, so called point bars. The helical flow in river bends sweeps lose particles up the slope of a point bar where the sediment accumulates laterally. The velocity of the flow is lower in the shallow part on the slope of the point bar, fine sediment particles accumulate here. In deeper parts on the slope of the point bar the velocity is high and coarser particles are deposited. This process results in a fining upward sequence, a typical vertical cross-section of a point bar is depicted in figure 6.1. The coarse bed load channel lag deposits are deposited when the flow rate in the river was high. When the meander loop is abandoned fine deposits accumulate during high water conditions on top of the point bar forming a clay plug. The total thickness of a point bar sequence varies but can be several meters.

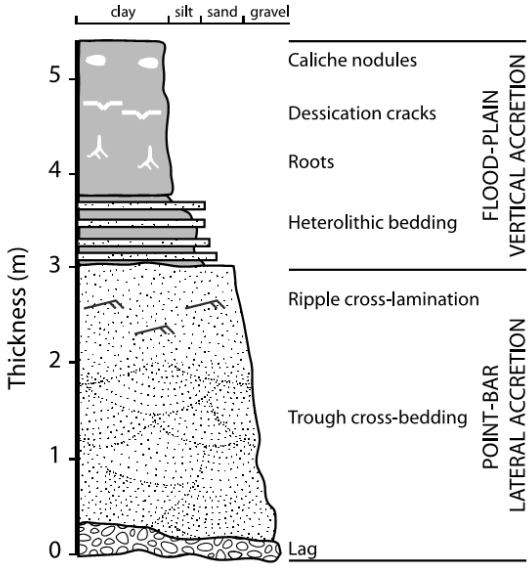

FIGURE 6.1: Classic point bar sequence from Donselaar and Overeem (2008)

6.2 Data acquisition

In the Huesca basin two wells were drilled and logged: Piracés-1 and Piracés-2. All common well logs are run in the wells such as spectral gamma-ray, FMI or FMS, density, NPHI etc. The well logs in Piracés-1 were run twice after the depth of the well was increased one year after drilling. In addition from Piracés-1 a core was recovered, slabbed and described. The logs and the core description show multiple point bars sequences in both wells.

From the well logs and core description of Piracés-1 4 point bar sequences were identified and selected for analysis. The sequences with their grain size interpretation are given in table 6.1. A number of samples from the core are selected:

1. 13 core plugs over the entire drilled interval in different grain size classes are selected to determine the spectral gamma-ray response per grain size class.
2. 12 thin section are prepared from rock samples within the point bar sequences to determine the (differences in) mineralogy.

Point bar	**Interval (m)**
1	15.0 - 24.8
2	28.8 - 35.5
3	35.5 - 45.0
4	57.2 - 61.0

TABLE 6.1: Point bar sequence intervals studied in this chapter.

6.2.1 Core plug analysis

The coreplugs were analysed at the Medusa office, the same methodology was used as in Chapter 5. The accuracy of the results is also comparable, although the activities are in general slightly higher. The uranium concentrations are not reliable, the thorium and potassium content are accurate with standard deviations lower than 10% (see Appendix C). A plot of grain size versus the core plug radio-activity is shown in figure 6.2.

The K content increases with decreasing grain size although this relationship does not hold in the finer grain size classes. The Th content as determined from the core plugs seem to be uncorrelated to grain size.

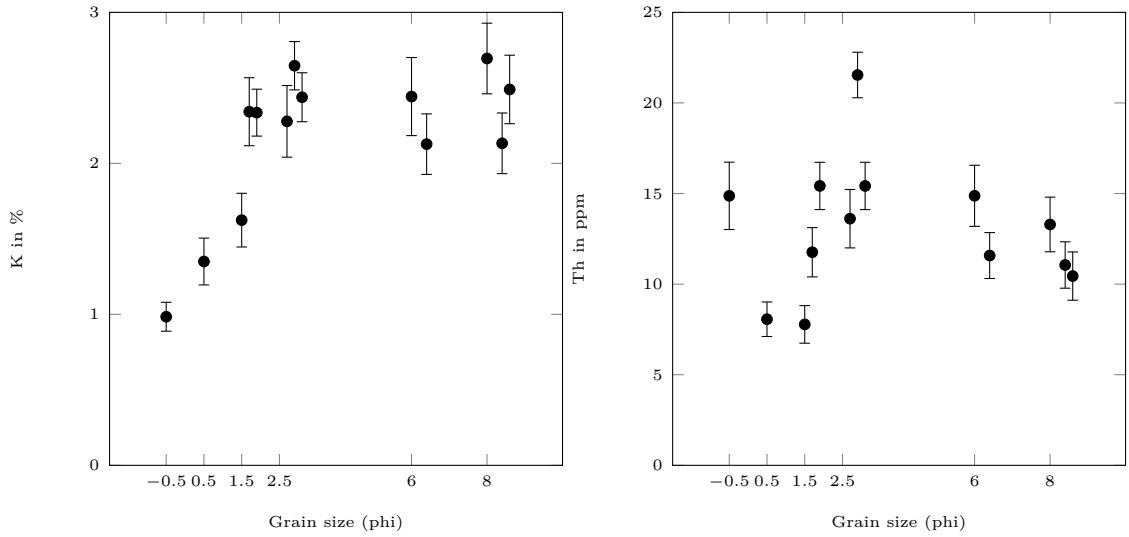

FIGURE 6.2: Left figure potassium content of coreplugs and estimated grain size. Right figure thorium content and grain size. Uranium measurements not shown due to poor results.

6.2.2 Thin section analysis

The mineralogy of the point bar sequences is studied to identify the most important gamma-ray carriers in each grain size class. A description of the thin sections is attached in Appendix C. A quantitative description of the minerals per grain size class was complicated by the large amount of rock fragments and is therefore not attempted. The coarse grains mainly consist of metamorphic and to a lesser extend volcanic rock fragments, quartz and calcite and minor amounts of feldspar (plagioclase and K-feldspar). Biotite and muscovite inclusions are sometimes present in the rock fragments. As the grain size decreases the proportion of clay minerals increases at the expense of rock fragments. In the fine grained fraction biotite and muscovite are more common but large biotite grains are often also present in the coarser fraction. Calcite is very common in every grain size class and is present as detrital clast and diagenetic cement especially in the fine grain fraction. The fine grained fraction is very well sorted, the coarsest fraction is poor to moderately sorted in these cases some clay can be present. The feldspar and biotite grains are largely unaltered indicating low maturity. The sediment is derived from granite and metamorphic rock. The most important minerals expected to carry the gamma-ray signal are clay minerals, biotite, muscovite, K-felspar and lithic fragments.

6.3 Interpretation of the gamma-ray signatures

The spectral gamma-ray were logged twice in well Piracés-1, once in the year the well was drilled (in 1996) and one year later when the depth of the well was increased(1997),

the logs are referred to as SGR96 and SGR97. A collection of relevant well logs are added in appendix C. The repeatability of the spectral gamma-ray logs is good in case of the thorium and potassium concentrations. The uranium content shows very large differences and appears to be not very reliable. Changes in borehole geometry (e.g. wash-outs) explain part of the deviation, clearly visible where K, U and Th show a spiked response but on other intervals the discrepancy is likely related to the poor repeatability of the gamma-ray log. The gamma-ray signature of the four point bar sequences as log-ratio quantities are plotted in figure 6.3.

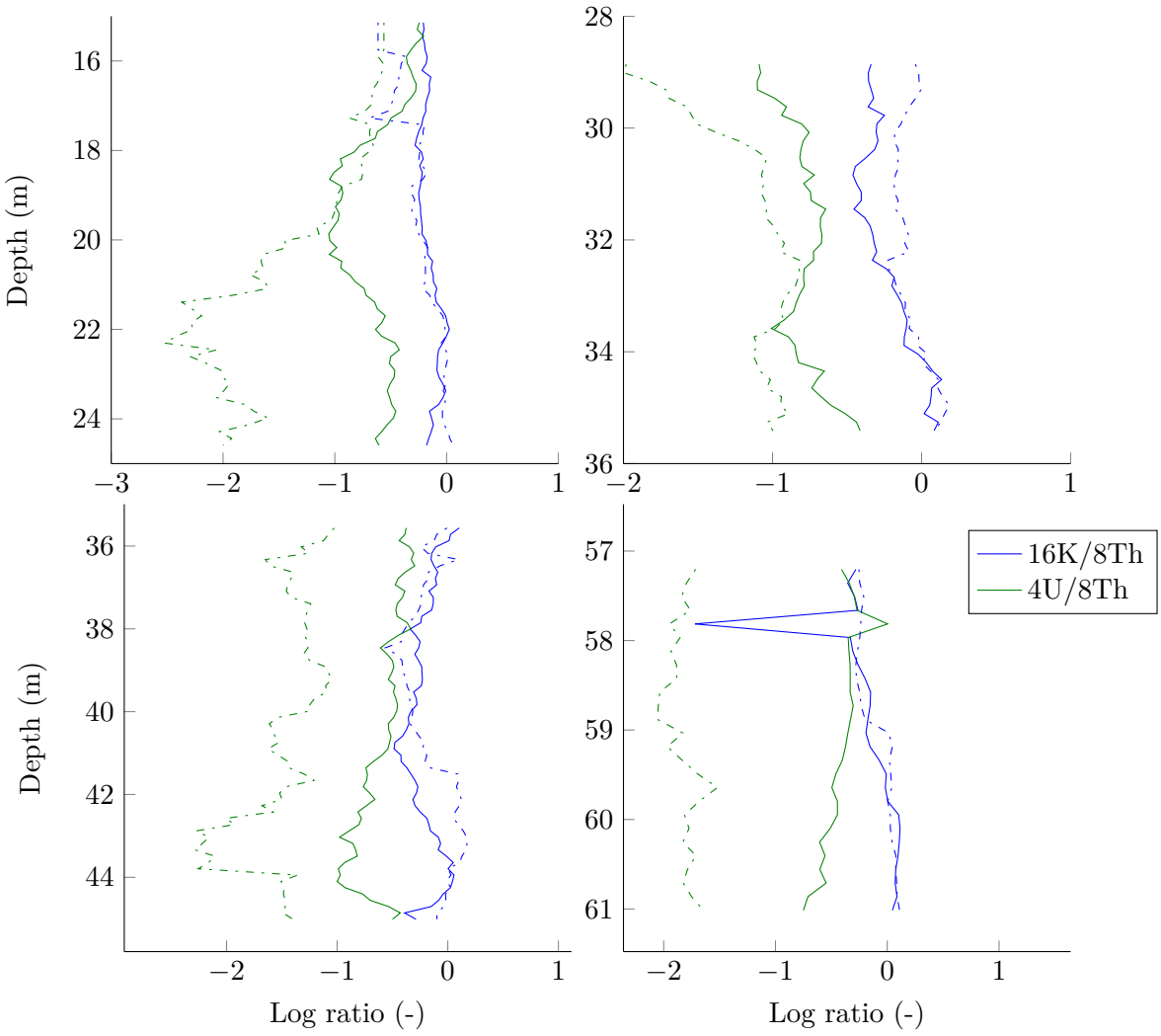

FIGURE 6.3: Depth versus log ratio of K/Th and U/Th over the point bar sequences. SGR96 is the dashed curve, the solid curve is the SGR97 log.

The K/Th ratio is almost constant with a slight tendency to increase upward i.e. the contribution of K to the API signal is slightly higher than the contribution of Th. In the U/Th ratio the opposite trend is dominant, the Th contribution is higher than U.

6.3.1 Forward prediction of gamma-ray signature

With the the size selective sorting model constructed in Chapter 4 an approximation of the signature over a point bar sequence can be made by estimating the proportion of minerals in the initial composition X_0. The most import gamma-ray carriers in the coarse fraction are expected to be rock fragments which can be weakly radio-active due to inclusion of for instance biotite and muscovite. All the minerals are assigned their average radio-activity values from table 2.1. The lithic fragments are assigned the following concentrations: 1 % K, 6 ppm Th and 2 ppm U. Calcite rock fragments are in this case included in the calcite group, since they are non-radio-active. Minerals present in small proportions include K-feldspars and mainly contribute to the K signal. In the fine fraction the mayor gamma-ray carriers are clay minerals and mica's. The clay minerals are expected to consists mainly of chlorite (as weathering product of biotite) and minor amounts of smectite based on a XRD mineralogy research in the area performed by Yuste et al. (2004). Figure 6.4 shows the predicted gamma-ray signature as function of k, where the sediment sorts from coarse sand sized particles to clay sized particles.

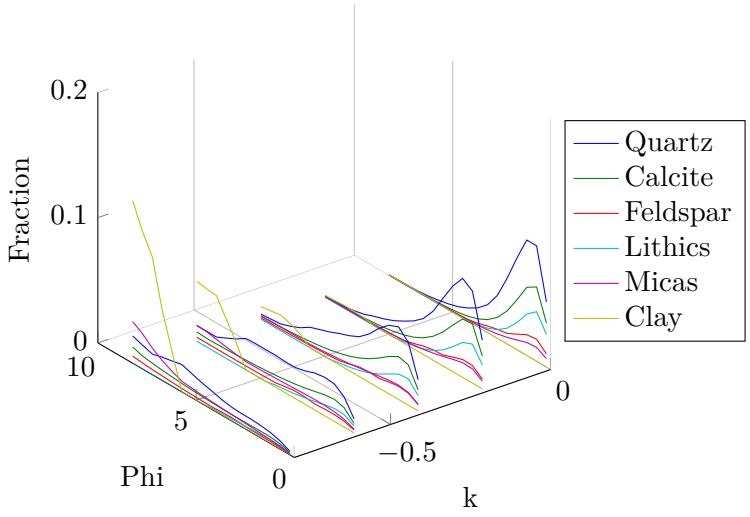

FIGURE 6.4: Initial composition: well sorted, coarse sand-sized particles consisting mainly of quartz,calcite and lithic fragments. Sorted particles are clay sized and consist of clay minerals, calcite and mica's.

The predicted gamma-ray signatures are depicted in figure 6.5. Both signatures do not resemble the gamma-ray signatures from the well logs (figure 6.3). In the modelled K/Th ratio the K signal is clearly dominant. Due to the high K content of K-feldspar and biotite in the clay fraction. The U/Th ratio shows a more complex trend where the uranium content in the coarse fraction dominates the thorium content, in the clay fraction the thorium content increases due to the presence of clay minerals and biotite and the U/Th ratio decreases.

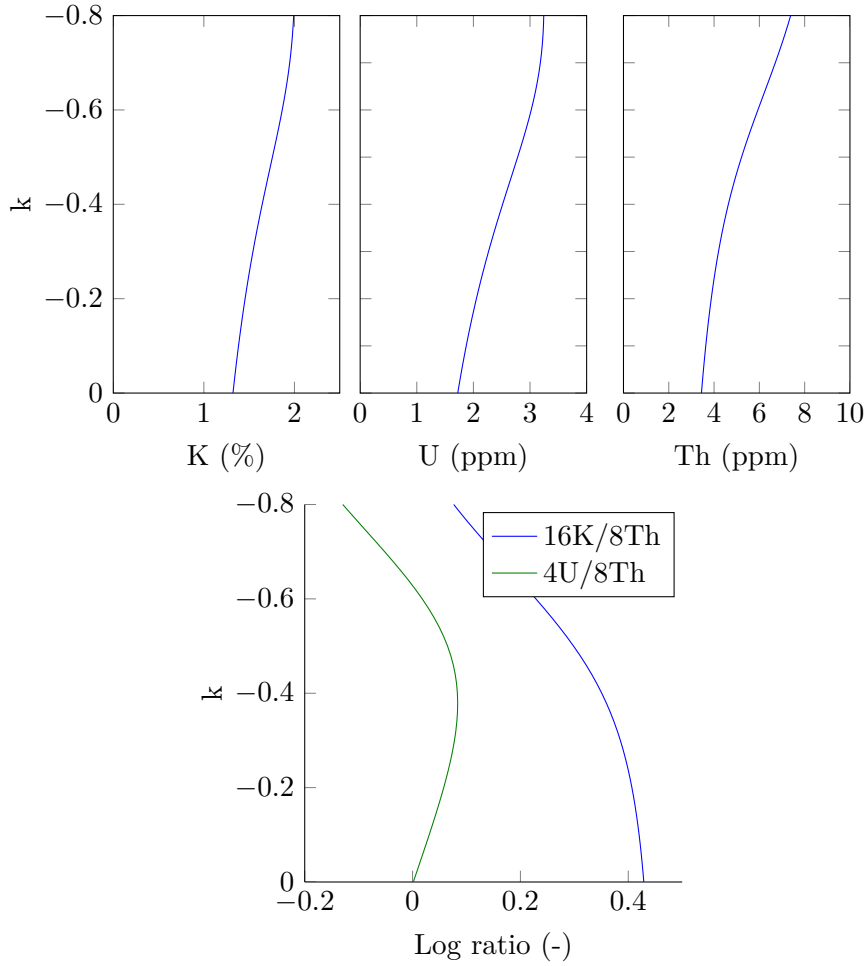

FIGURE 6.5: Forward predicted gamma-ray signatures of sediment. The k-values correspond to the following grain size classes: k=0 coarse grained sand, k=-0.2 medium sand, k=-0.4 medium sand k=-0.6 silt k=-0.8 clay.

6.3.2 Reconstruction of the gamma-ray log from grain size

In chapter chapter 5 a grain size record was available and used to assign a representative gamma-ray signature to each grain size class. In this stage of the analysis a grain size record is usually not available but other well logs can serve as a grain size proxy. Here, the Formation MicroScanner (FMS) well the log will be used to derive a grain size record. The approach is as follows:

- With calibration from samples derive an empirical relation from the FMS resistivity values;
- Assign a gamma-ray signature to the layers derived from the FMS;
- Find the optimal gamma-ray values for each grain size class by comparing the modelled and the measured gamma-ray log.

Formation Microscanner

The FMS records an high resolution image of the electrical conductivity ($ohm \cdot m^2/m$) of the formation. Layers of around 1 cm can be distinguished (Luthi, 2000), invisible to the spectral gamma-ray tool. The lower part of the sonde contains pads with electrodes and the current is forced in the formation at a right angle. The lower part of the tool is kept at a known potential with respect to the upper part of the tool, the potential drop is proportional to the resistivity of the formation. Piracés-1 has been logged with a sonde containing 4 pads each consisting of 16 electrodes, the resulting image covers approximately 50% of the 6inch borehole (Rider, 2002). The electrical conductivity of the formation is mostly influenced by the type and properties of the pore fluids (e.g. temperature, salinity and presence of hydrocarbons) but when these properties are constant, changes in the conductivity of the matrix are clearly visible. The rock matrix acts as an insulator while clay minerals are conductive. Figure C.1 shows the FMS and various other well logs. A linear curve was fitted between grain size and the log-transformed resistivity values and using this relation ranges of resistivity were assigned to each grain size class as shown in table 6.2.

Class	**Grain size**	**Phi**	**Resistivity range**
1	Clay	>8	26.9 - 142.8
2	Silt	4-8	11.4 - 26.9
3	Fine sand	3-4	9.2 - 11.4
4	Medium sand	1-2	6.0- 9.2
5	Coarse sand	< 1	0.0 - 6.0

TABLE 6.2: Resistivity range assigned to each grain size class based on calibration with thin sections and coreplugs.

The resistivity values were averaged such that the minimum bedding thickness is at least 5 cm. Thinner beds can be resolved with the FMS tool but since the gamma-ray tool only has an vertical resolution of 20cm - 30cm the model would be very insensitive to changes in gamma-ray signature. The result of the grain size classification are shown in figure 6.6.

Optimisation

The K,U and Th signature of each grain size class were determined with the optimisation model of chapter 5, using the input of the in 1996 recorded gamma-ray logs. The starting values assigned to each grain size class were initially based on the the core-plug gamma-ray measurements (see figure 6.2) with the exception of the uranium values which were estimated based on the gamma-ray log. The results, however, were poor due to the large measurement error in the core-plug gamma-ray values. When there is a large discrepancy between the initial values and the 'solution' the optimisation routine

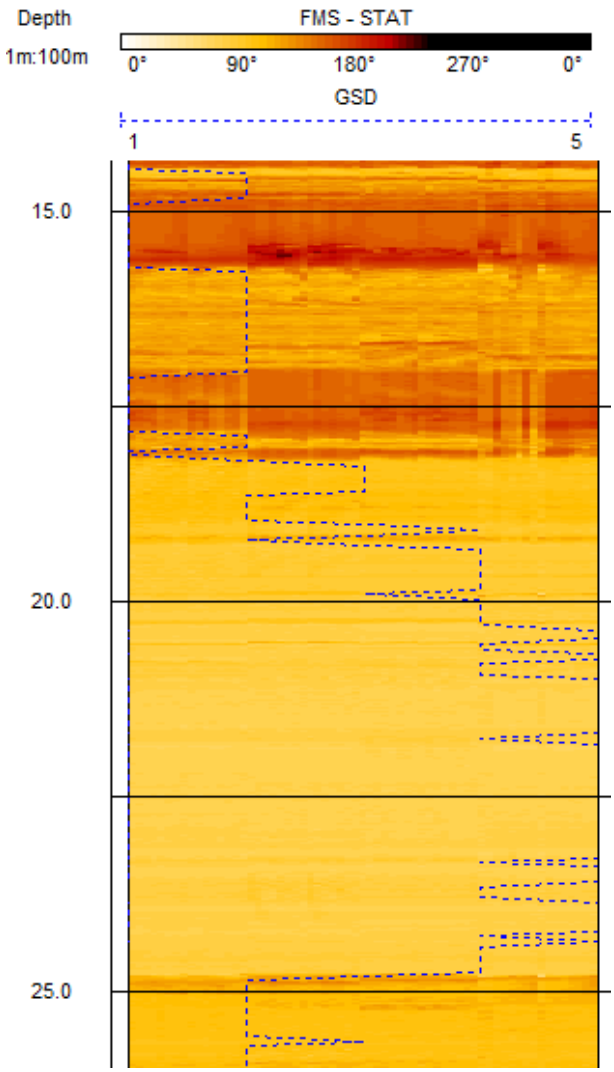

FIGURE 6.6: Sample grain size interpretation over one point bar sequence. Grain size codes refer to table 6.2. FMS resistivity values: dark = conductive bright = resistive.

can get 'stuck' in a local minimum. Therefore better results were obtained when the gamma-ray values were estimated from the gamma-ray log. The resulting fit is shown in figure 6.9 with the gamma-ray signature per grain size class given in figure 6.8. Again the thorium signal shows the strongest correlation to grain size. The uranium signal also corresponds reasonably well to grain size while for the potassium signal no relationship with grain size was found.

Signature per point bar sequence

For the potassium signal it appears no unique signature per grain size class can be determined. The response per point bar sequence can be processed individually to determine the difference in the composition or properties of the minerals within equal grain size classes. Due to the low number of data points in grain size classes with phi values < 1 in point bar sequence 2 and grain size class 3-4 in point bar sequence

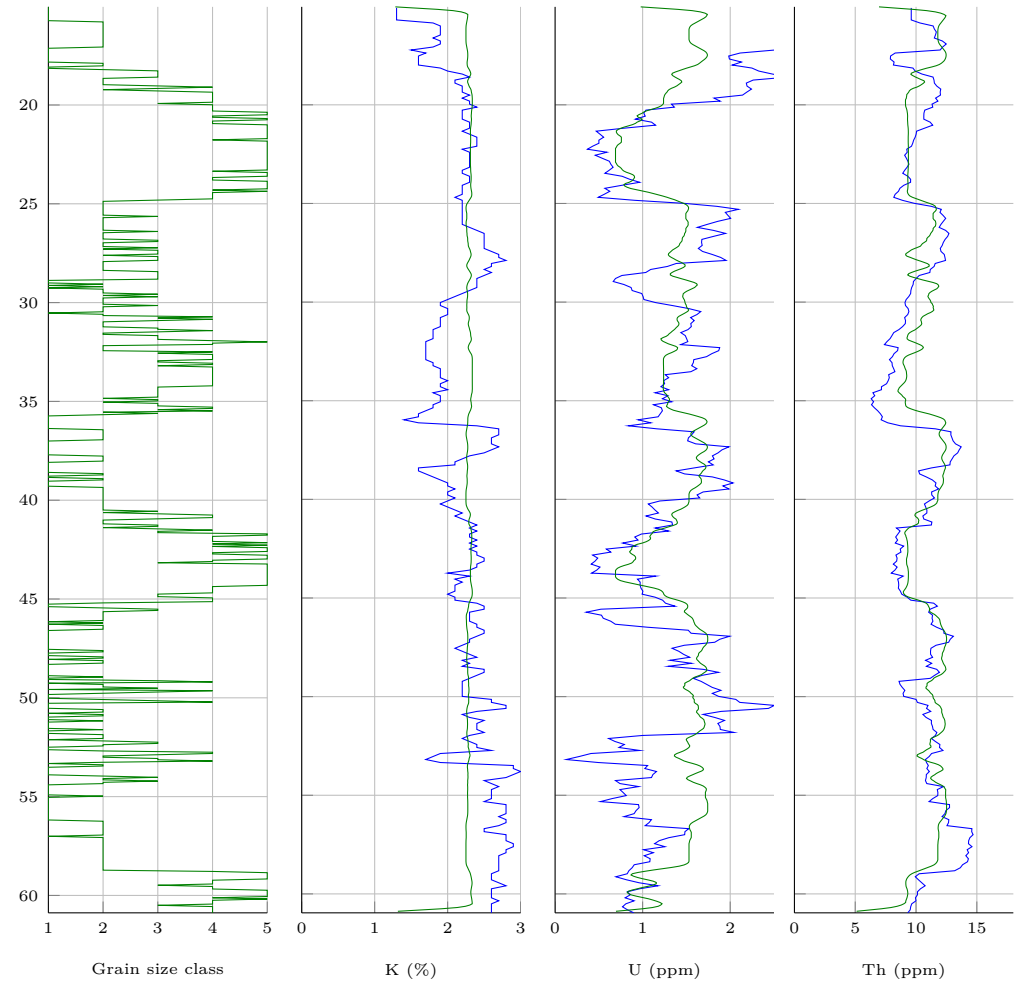

FIGURE 6.7: Left figure grain size interpretation from FMS. Right figures, gamma-ray signature from well logs (blue) and fitted gamma-ray signature (green). Grain size codes increasing in grain size from clay (1) to coarse sand (5), see table 6.2.

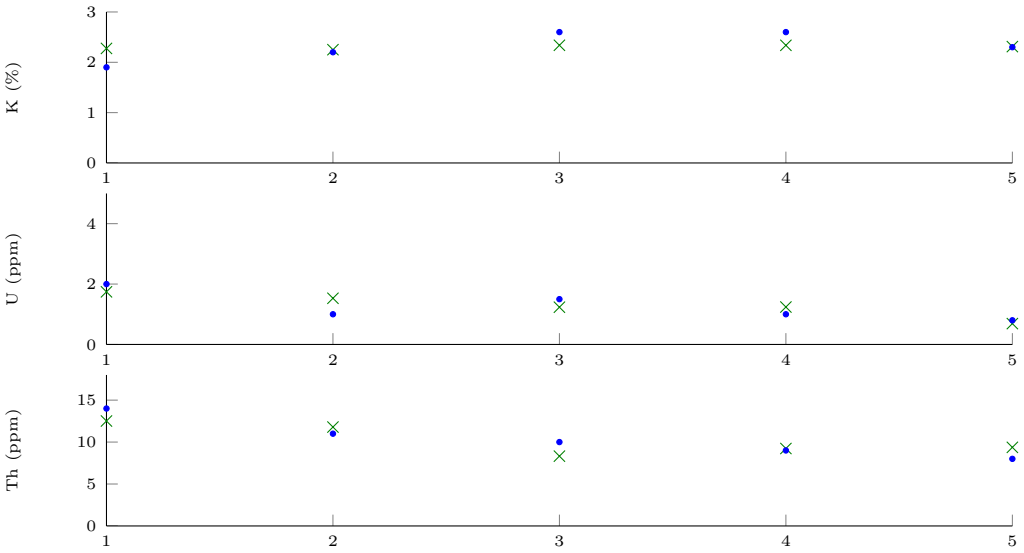

FIGURE 6.8: Resolved gamma-ray values for each grain size class. Blue dots, initial values from core-plug gamma-ray. Green crosses, optimised values.

4 these results were discarded. Figure 6.9 shows the fit of each separately processed interval with the well log gamma-ray, figure 6.10 shows the variance in the gamma-ray signature. The thorium signature is in almost all cases increasing with decreasing grain size. The uranium signal shows a similar trend, except point bar 1 which shows values in grain size class 1 and 3. As expected the potassium signal shows a fairly high spread in almost every grain size class except class 3 and a variable relationship with grain size.

Point bar	$> 8\phi$			4ϕ-8ϕ			3ϕ-4ϕ			1ϕ-2ϕ			$< 1\phi$		
1	1.7	2.9	12.3	2.0	1.7	10.7	2.4	2.2	11.0	2.3	1.4	11.4	2.3	0.5	9.3
2	2.9	1.8	17.5	2.0	1.3	8.9	2.3	1.4	8.5	2.3	1.4	7.8	-	-	-
3	2.0	1.8	12.3	2.2	1.4	11.4	2.5	1.5	8.1	2.3	0.9	10.3	2.2	0.7	8.7
4	2.9	1.7	14.3	2.8	1.1	14.1	-	-	-	2.7	0.9	8.7	2.5	0.8	10.7

TABLE 6.3: K, U and Th signatures per grain size class of each point bar sequence.

The most striking difference in gamma-ray signatures of the point bar sequences is the high potassium content in point bar 4 (interval 57m - 61m) where the potassium values of every grain size class, with the exception of grain size class 3, show an higher potassium content. The increase in potassium seems unrelated to grain size and with the increase in potassium content no increase in thorium or uranium is observed, see figure 6.11, it is therefore expected to be unrelated to an increase in clay minerals. A plausible explanation can be an increase the proportion or K content of K-feldspar, K-feldspar has an high K-content and very low U and Th content. The thin section analysis did not reveal any large differences in mineralogy but no quantitative analysis was performed.

Resolution improvements with high resolution grain size

If a well log is particularly well described by changes in grain size (i.e. the gamma-ray signal is mainly a grain size signal) the resolved layered input (matrix G) represents a higher resolution gamma-ray log. The higher resolution log can be used in petrophysical analysis, for example to determine the shale content. As an example the layered model of the point bar sequence in the interval 57.2m - 61m is shown in figure 6.12.

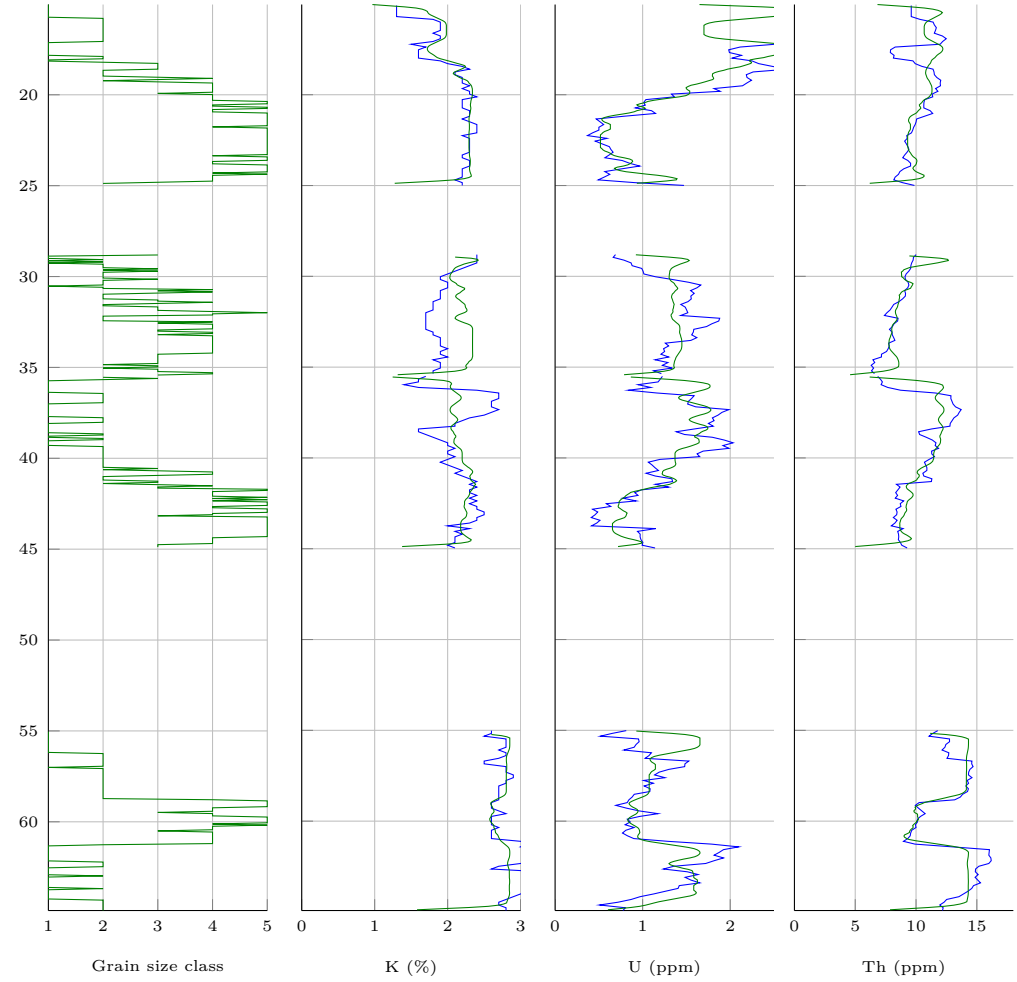

FIGURE 6.9: Fit of modelled (green curve) and gamma-ray well log (blue curve) of the point bar sequences processed separately.

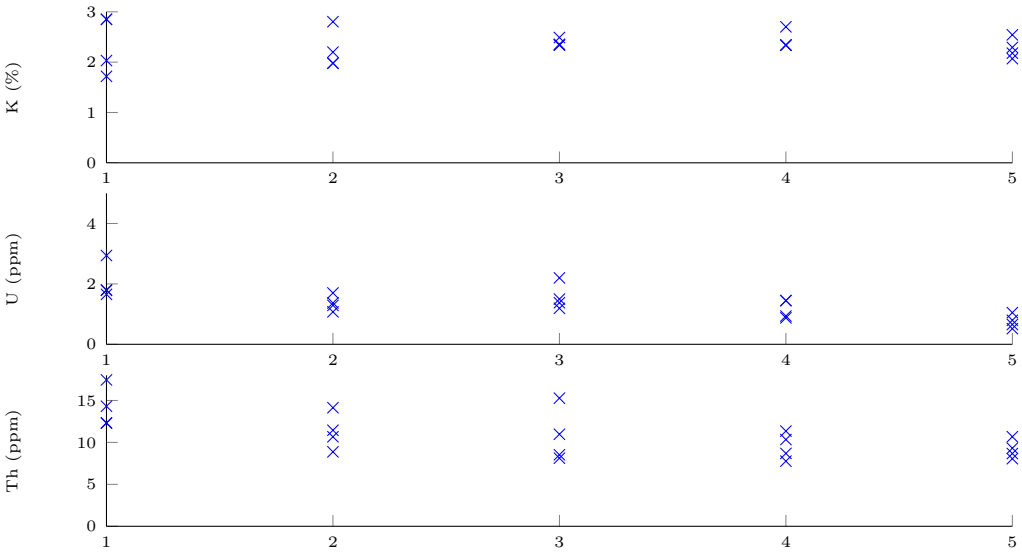

FIGURE 6.10: Point bar sequences resolved separately. Colors refer to following point bar sequences: 15 - 24.8m red, 28.8 - 35.5m green, 35.5 - 45.0 black, 57.2 - 61 blue.

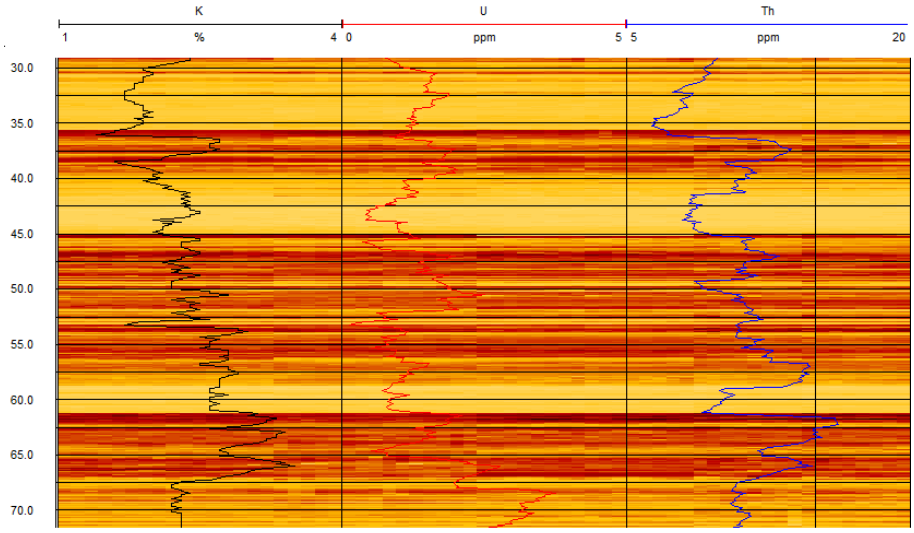

FIGURE 6.11: FMS with gamma-ray overlay. Large section of increasing potassium content in the interval 45m - 67m. Grain size decreases from bright to dark.

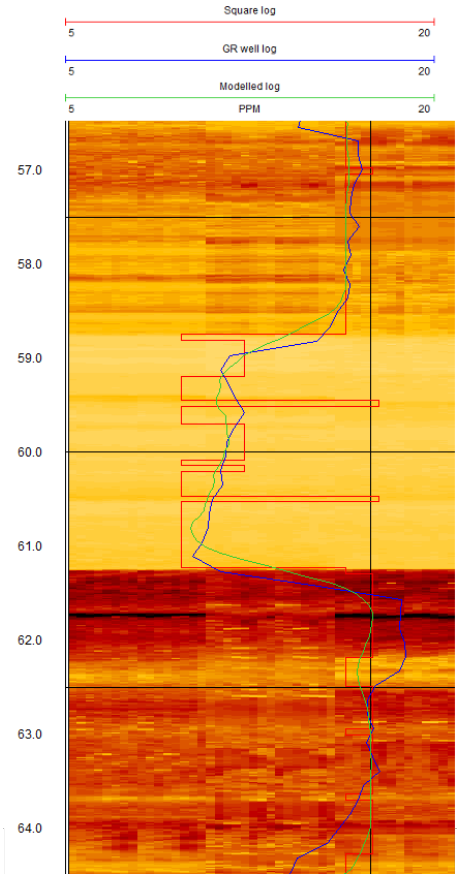

FIGURE 6.12: FMS with high resolution squared log (red) overlay. Blue curve is the thorium response of the gamma-ray log with the fitted (green) curve

6.3.3 Iterative fit of the selective sorting model with the well log gamma-ray

The gamma-ray signatures produced by the forward model failed to result in a close match with the recorded well log gamma-ray. With the iterative forward model we can attempt to find the closest match by iteratively changing the concentration of K, U and Th of the mayor radio-active minerals and assessing the fit with the well log gamma-ray and resulting radio-nuclide concentrations. The start and end values are of the interval are chosen based on the grain size, the interval starts at an interval of coarse sand and ends at an interval containing clay. The grain size is based on the classification from the FMS log. The minerals are grouped in 4 classes and given the initial values as defined in table 6.4.

Mineral	K (%)	U (ppm)	Th (ppm)
Feldspar	14	1	5
Lithics	2,5	2	8
Mica	8	5	25
Clay	1	1	15

TABLE 6.4: Initial values and classes defined for the optimisation.

The optimisation is applied to the log-transformed radio-nuclide concentrations of the API, K/Th and the U/Th ratio. The optimisation is roughly constrained to upper and lower bounds given in the literature, see table 2.1. The quality of the fit is given in figure 6.13, the resulting radio-nuclide concentrations are listed in table 6.5.

The spread in the radio-nuclides is very large. Furthermore, the results of the fitting procedure change considerably when the model is given different initial values or upper and lower bounds. In other words, there is a large number of solutions for this problem with not enough constraints to provide a meaningful solution.

6.4 Discussion and conclusion

The first goal of this chapter was:

Can we accurately model the gamma-ray signature of sediment subject to size selective sorting?

The model input was determined by estimating the mineral composition of the point bar deposits by thin sections analysis selected a number of grain size classes. With

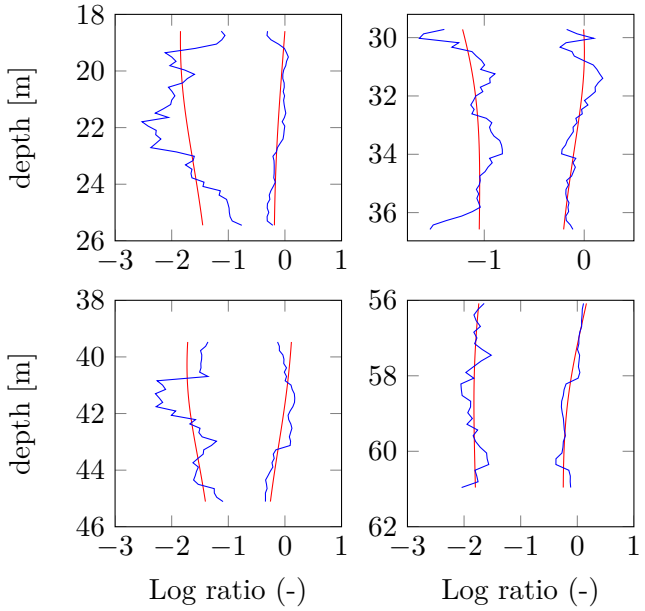

FIGURE 6.13: Log ratio nuclide concentrations, left: U/Th right: K/Th with fit from sorting model in red.

	Feldspar			Lithics		
	K (%)	U (ppm)	Th (ppm)	K (%)	U (ppm)	Th (ppm)
PB 1	7.4	0.8	0.7	1.0	1.1	7.2
PB 2	0.9	1.4	9.7	0.1	0.0	9.5
PB 3	1.3	0.2	7.7	1.3	1.1	3.1
PB 4	0.1	1.3	6.3	6.3	1.0	3.5
	Mica			Clay		
	K (%)	U (ppm)	Th (ppm)	K (%)	U (ppm)	Th (ppm)
PB 1	0.1	0.0	40.6	3.4	2.7	8.6
PB 2	11.1	3.7	2.6	7.8	8.9	56.9
PB 3	6.4	0.0	19.2	0.4	2.0	8.0
PB 4	4.3	1.0	46.4	8.9	4.0	37.9

TABLE 6.5: Radio-activity in minerals resolved from gamma-ray signatures.

the forward model, using fixed radio-nuclide concentrations, and the iterative model, where the concentrations are free to vary, the match with the well log gamma-ray was assessed. The forward model does not result in a close match with the well log gamma-ray. With the iterative model the signatures can be replicated very accurately but the resulting radio-nuclide concentrations show an unrealistic large spread. This confirms the earlier findings on synthetic data (chapter 4): small differences in signature result in a very large difference in radio-nuclide concentrations. Furthermore, it is observed that

(small) changes in the constraints of the optimisation routine have a very large effect on the resulting radio-nuclide concentrations. This result indicate there is a multitude of solutions to the problem with not enough constraints.

Can we derive information from the residual gamma-ray signal if the variation caused by selective transport is minimized?

Similarly to chapter 5 with a grain size record the gamma-ray signature per grain size class can be derived. In this case a proxy for grain size is obtained from the FMS log. In assigning a resistivity range to the grain size values, calibration with samples is necessary. The fit of the model with the thorium content is good, the uranium content moderate, while for the potassium content no unique signature per grain size class could be found. Therefore the difference in gamma-ray signature between the point bar sequences was assessed individually. In general the spread in the gamma-ray signatures is modest, apart from a few outliers. The thorium and (less pronounced) the uranium content both show decreasing concentrations with increasing grain size. The potassium content shows no trend with grain size. The largest difference in gamma-ray signature are observed in point bar sequence 4, where the potassium content is higher than in other point bar deposits. An increasing potassium content is observed over a larger interval from 45m to 66m. With the increase in potassium no increase in thorium or uranium is observed. Many plausible explanations can be given for the increased potassium content for example increased proportion of K-feldspar, radio-activity of the potassium bearing minerals or increased K-content in the pores due to dissolution.

Chapter 7

Conclusions and recommendations

7.1 Conclusions

In chapter 1 two questions were posed with the aim of finding an answer to the main question: can we improve the use of the gamma-ray log? The first question:

Can we accurately model the gamma-ray signature of sediment subject to size selective sorting?

In the application of the iterative forward and forward model to the Huesca dataset it was observed the model is unable to produce realistic results. In the iterative approach the model is able to find a close fit with the well log gamma-ray. However, the resulting radio-nuclide concentrations show very large variations between the point bar sequences. This confirms the earlier findings on synthetic data: small changes in gamma-ray signatures result in large variations in the radio-nuclide concentrations. The constraints and initial values used in the optimisation have a very large effect on the resulting radio-nuclide concentrations illustrating there are many solutions possible.

The use of a compositional linear trend may, in case of the point bar deposits, not be an accurate representation of the sorting of the sediment. Point bar deposits consist of well sorted sediment but starting with a well sorted coarse fraction the model will sort to a poorly sorted composition before reaching a well sorted clay fraction (see figure 6.4).

The second question:
Can we derive information from the residual gamma-ray signal if the variation caused by selective transport is minimized?

The gamma-ray record of core E10-3 showed a fairly high dependency on grain size, especially the thorium content. Residual variation remains but cannot only be attributed to changes in provenance or diagenesis because part of the variation is still (partly) caused by size dependent processes. Especially the degree of sorting can cause large variations. Since we are dealing with consolidated sediment there is no way to obtain a gamma-ray signature per (perfectly sorted) grain size fraction. Poorly sorted sediment in the model is represented by a scalar (median grain size) while in reality the grain size is a vector (a distribution) and therefore will show a variable gamma-ray response. Other factors expected to explain the variation in core E10-3 are:

1. Organic content.
2. Diagenesis (kaolinite).
3. Noise in the gamma-ray log. For example changes in borehole geometry such as wash-outs and position of the detector during acquisition.

In case of core E10-3 it is hard to interpret the residual variance since no large structural differences are observed.

The analysis on the Huesca core resulted in more obvious differences in gamma-ray signature. The analysis of the point bar deposits showed an increase in almost all grain size classes in the concentrations of potassium in the point bar at the interval 57-61m. This increased content is observed over a larger interval and therefore more likely explained by diagenesis or provenance. Many plausible explanations exist for example diagenesis (dissolved potassium from feldspars), increased radio-activity in potassium bearing minerals and increased proportions of K-feldspar.

The main goal of this thesis was:
Can we improve the use of the gamma-ray log?

Gamma-ray signatures or curves are mainly used for correlation purposes but have the potential to serve as an indicator for changes in provenance or diagenesis as illustrated in this thesis. The most important limitations of the gamma-ray log are the sensitivity to noise and limited resolution. Moreover, the dependency on facies often (partially) remains because when dealing with consolidated rock we cannot group the sediment in perfectly sorted grain size classes. It can therefore only be considered a fairly crude tool.

Therefore one particular suitable application of the core or well gamma-ray log could be to guide the core plug or thin section sampling from a recovered core. Usually, core plugs are sampled with a fixed interval from a recovered core. The sampling strategy could be

improved if areas of interest are indicated from the interpretation of the gamma-ray log. However, this requires a grain size record or grain size proxy such as the FMS tool as applied in Chapter 6. When multiple wells are drilled within the same basin this type of information might be available and can be used to assess the similarity of the sediment across wells.

The use of the gamma-ray log as a form of quality control after core analysis can also be considered, as attempted with the two grain size records in chapter 5. The use of an higher resolution gamma-ray log could further improve the use of this method.

7.2 Recommendations

The recommendations are separated in two sections for their relevant models, the selective sorting model and model used to derive the grain size signatures.

Selective sorting model
The performance or validity of the model has been assessed only based on the forward and iteratively forward prediction of gamma-ray logs of the point bar sequences of the Huesca dataset. Due to the large amounts of lithic fragments proper quantification of the mineral composition was not attempted. Instead the composition was estimated, which could potentially be large source of errors. A more thorough evaluation should contain an accurate quantification of the minerals in the composition.

Gamma-ray reconstruction from grain size
The results of the gamma-ray measurements on the core plugs were poor due to the low weight of the samples. It was suggested to change the acquisition of the core gamma-ray such that an higher resolution gamma-ray log is obtained, by decreasing the length of the detector and using deconvolution and regularisation. This approach should be investigated further to assess if this approach is feasible.

The Nelder-Mead optimization routine used to derive the gamma-ray signature in general performed excellent but more constraints can be added to select the most optimum solution. For example to prevent solution which are just an average value of the gamma-ray log, the variance of the solution and the well log can be compared.

Appendix A

Synthetic granitiod and metamorphic dataset

The synthetic data is compiled from (Sanchez-Ramirez et al., 2010). The metamorphic dataset can be found in table A.1. The granitoid dataset can be found in table A.2.

TABLE A.1: Metamorphic dataset (matrix F)

Mineral	Median phi grain size																		
	-0.77	-0.27	0.23	0.73	1.23	1.73	2.23	2.73	3.23	3.73	4.23	4.73	5.23	5.73	6.23	6.73	7.23	7.73	8.23
Quartz	0.56	0.61	0.65	0.55	0.50	0.40	0.35	0.36	0.37	0.26	0.18	0.13	0.09	0.06	0.04	0.03	0.02	0.01	0.00
K-Feldspar	0.22	0.19	0.18	0.19	0.19	0.16	0.13	0.13	0.13	0.09	0.06	0.04	0.03	0.02	0.01	0.01	0.01	0.00	0.00
Plagioclase	0.18	0.14	0.12	0.21	0.27	0.36	0.42	0.41	0.40	0.28	0.19	0.13	0.09	0.06	0.04	0.03	0.02	0.01	0.00
Lithics and other	0.01	0.01	0.00	0.00	0.00	0.00	0.00	0.00	0.00	0.00	0.00	0.00	0.00	0.00	0.00	0.00	0.00	0.00	0.00
Non-radioactive	0.00	0.00	0.00	0.00	0.00	0.01	0.02	0.02	0.02	0.01	0.01	0.01	0.00	0.00	0.00	0.00	0.00	0.00	0.00
Apatite	0.00	0.00	0.00	0.00	0.00	0.00	0.00	0.00	0.00	0.00	0.00	0.00	0.00	0.00	0.00	0.00	0.00	0.00	0.00
Hornblende	0.00	0.00	0.00	0.00	0.00	0.00	0.00	0.00	0.00	0.00	0.00	0.00	0.00	0.00	0.00	0.00	0.00	0.00	0.00
Xenotime	0.00	0.00	0.00	0.00	0.00	0.00	0.00	0.00	0.00	0.00	0.00	0.00	0.00	0.00	0.00	0.00	0.00	0.00	0.00
Muscovite	0.00	0.02	0.03	0.02	0.00	0.03	0.03	0.03	0.02	0.02	0.01	0.01	0.01	0.00	0.00	0.00	0.00	0.00	0.00
Biotite	0.02	0.02	0.02	0.03	0.03	0.04	0.05	0.05	0.06	0.04	0.03	0.02	0.01	0.01	0.01	0.00	0.00	0.00	0.00
Chlorite	0.00	0.00	0.00	0.00	0.00	0.00	0.00	0.00	0.00	0.00	0.00	0.00	0.00	0.00	0.00	0.00	0.00	0.00	0.00
Smectite	0.00	0.00	0.00	0.00	0.00	0.00	0.00	0.00	0.00	0.10	0.17	0.22	0.26	0.29	0.30	0.32	0.33	0.33	0.34
Illite	0.00	0.00	0.00	0.00	0.00	0.00	0.00	0.00	0.00	0.10	0.17	0.22	0.25	0.28	0.30	0.31	0.32	0.32	0.33
Kaolinite	0.00	0.00	0.00	0.00	0.00	0.00	0.00	0.00	0.00	0.10	0.17	0.22	0.25	0.28	0.30	0.31	0.32	0.32	0.33

TABLE A.2: Granitoid dataset (matrix F)

Mineral	Median phi grain size															
	0.73	1.23	1.73	2.23	2.73	3.23	3.73	4.23	4.73	5.23	5.73	6.23	6.73	7.23	7.73	8.23
Quartz	0.44	0.40	0.34	0.35	0.36	0.36	0.36	0.21	0.12	0.08	0.05	0.04	0.03	0.01	0.01	0.01
K-Feldspar	0.33	0.27	0.19	0.16	0.10	0.12	0.15	0.09	0.05	0.03	0.02	0.01	0.01	0.01	0.00	0.00
Plagioclase	0.13	0.21	0.32	0.34	0.38	0.36	0.33	0.19	0.11	0.06	0.04	0.03	0.02	0.01	0.01	0.01
Lithics and other	0.01	0.01	0.01	0.01	0.01	0.01	0.02	0.01	0.01	0.00	0.00	0.00	0.00	0.00	0.00	0.00
Non-radioactive	0.01	0.00	0.00	0.00	0.01	0.00	0.00	0.00	0.00	0.00	0.00	0.00	0.00	0.00	0.00	0.00
Apatite	0.00	0.00	0.00	0.00	0.00	0.00	0.00	0.00	0.00	0.00	0.00	0.00	0.00	0.00	0.00	0.00
Hornblende	0.00	0.00	0.00	0.00	0.00	0.00	0.00	0.00	0.00	0.00	0.00	0.00	0.00	0.00	0.00	0.00
Zircon	0.00	0.00	0.00	0.00	0.00	0.00	0.00	0.00	0.00	0.00	0.00	0.00	0.00	0.00	0.00	0.00
Xenotime	0.00	0.00	0.00	0.00	0.00	0.00	0.00	0.00	0.00	0.00	0.00	0.00	0.00	0.00	0.00	0.00
Muscovite	0.03	0.02	0.02	0.03	0.04	0.03	0.02	0.01	0.01	0.00	0.00	0.00	0.00	0.00	0.00	0.00
Biotite	0.05	0.08	0.11	0.11	0.10	0.10	0.11	0.06	0.03	0.02	0.01	0.01	0.01	0.00	0.00	0.00
Chlorite	0.00	0.00	0.00	0.00	0.00	0.01	0.01	0.00	0.00	0.00	0.00	0.00	0.00	0.00	0.00	0.00
Smectite	0.00	0.00	0.00	0.00	0.00	0.00	0.00	0.14	0.22	0.27	0.29	0.30	0.31	0.32	0.32	0.31
Illite	0.00	0.00	0.00	0.00	0.00	0.00	0.00	0.14	0.22	0.27	0.29	0.30	0.31	0.33	0.33	0.34
Kaolinite	0.00	0.00	0.00	0.00	0.00	0.00	0.00	0.14	0.22	0.27	0.29	0.30	0.31	0.32	0.32	0.33

Appendix B

Dataset E10-3

B.1 Core plug selection and analysis

Core E10-3 consists of 11 grain size classes, in total 20 (homogeneous) core plugs are selected to be analysed. The selected core plugs are listed in table B.1. The sample codes are adopted from Boels (2003). The standard deviations (listed as fraction) is the uncertainty based on count statistic. Table B.2 gives the final values of K, U and Th assigned to each grain size class.

Sample	**Facies**	**Mass**	**K**	**S-K**	**U**	**S-U**	**Th**	**S-Th**
		(gr)	**(%)**	**(-)**	**(ppm)**	**(%)**	**(ppm)**	**(-)**
16	S3l	47,8	0,07	0,39	-0,64	-0,82	1,05	0,76
20	S3l	47,2	0,22	0,39	-0,02	-0,70	4,83	0,17
43	M	37,4	1,69	0,10	0,21	2,10	-0,06	-15,00
75	J	41	1,49	0,10	0,20	1,30	5,91	0,16
80	S1u	42,4	1,44	0,10	-0,07	-0,11	8,79	0,10
84	S2l	40,4	0,94	0,14	-0,73	-0,62	2,32	0,41
86	S1u	40,6	1,55	0,10	0,20	2,10	-0,06	-15,00
100	S2u	47	0,79	0,09	0,14	2,38	2,09	0,41
104	S2u	45,6	0,61	0,10	-3,42	-0,11	9,26	0,13
122	S4l	44,4	-1,06	-0,15	-0,79	-0,64	4,49	0,25
142	S2l	47,6	1,05	0,06	-1,73	-0,11	10,13	0,08
155	S3u	44,6	0,05	0,47	-0,23	-1,85	1,78	0,48
156	S4u	47,6	0,78	0,47	-0,74	-0,23	2,92	0,21
167	S3u	43,2	-0,11	-0,24	3,65	0,08	-3,50	-0,24
174	S5l	44,6	0,07	0,80	0,04	11,00	1,40	0,54
218	S1l	58,6	0,90	0,12	0,37	0,67	7,25	0,11
222	S1l	49,6	1,17	0,11	1,52	0,23	6,36	0,14
252	M	53,4	2,06	0,09	1,56	0,23	12,45	0,09
259	M	47,4	2,06	0,09	3,17	0,15	17,57	0,09
280	J	54,4	2,33	0,08	1,12	0,34	15,75	0,08

M	Mudstone	S3l	Medium lower sandstone
J	Siltstone	S3u	Medium upper sandstone
S1l	Very fine lower sandstone	S4l	Coarse lower sandstone
S1u	Very fine upper sandstone	S4u	Coarse upper sandstone
S2l	Fine lower sandstone	S5l	Very coarse lower sandstone
S2u	Fine upper sandstone		

Table B.1: Core plug radio-nuclide concentrations and facies class.

	K (%)	S-K (%)	U (ppm)	S-U (ppm)	Th (ppm)	S-Th (ppm)
M	1.94	0.22	1.65	1.48	15.01	3.62
J	1.91	0.60	0.66	0.65	10.83	6.96
S1l	1.03	0.19	0.94	0.81	6.81	0.63
S1u	1.50	0.08	0.20	0.00	8.79	0.00
S2l	1.00	0.08	0.00	0.00	6.23	5.53
S2u	0.70	0.12	0.07	0.10	5.68	5.07
S3l	0.14	0.11	0.00	0.00	2.94	2.67
S3u	0.05	0.00	3.65	0.00	1.78	0.00
S4l	0.00	0.00	0.00	0.00	4.49	0.00
S4u	0.78	0.00	0.00	0.00	2.92	0.00
S5l	0.07	0.00	0.04	0.00	1.40	0.00

TABLE B.2: Mean and standard deviation of K, U and Th values assigned to each grain size class. The standard deviation is zero when only one core plug within a grain size class is analysed.

B.2 Fit results Nelder-Mead

The histograms in this section show the residuals (well log gamma-ray minus the optimised gamma-ray) per grain size class for both the multi-variate regression and the Bayesian grain size classification.

Potassium discrepancy based on the Bayesian dataset

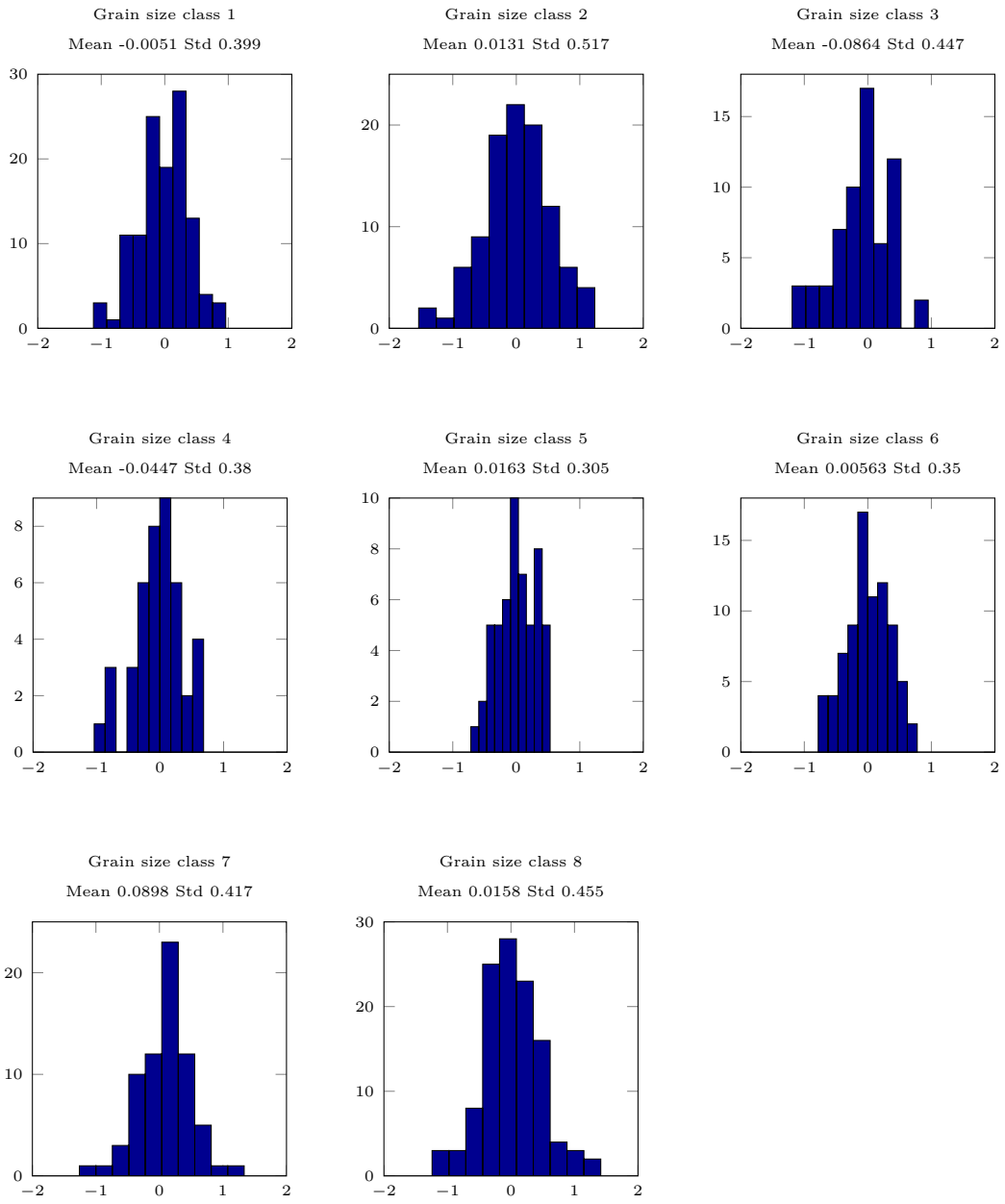

Uranium discrepancy based on the Bayesian dataset

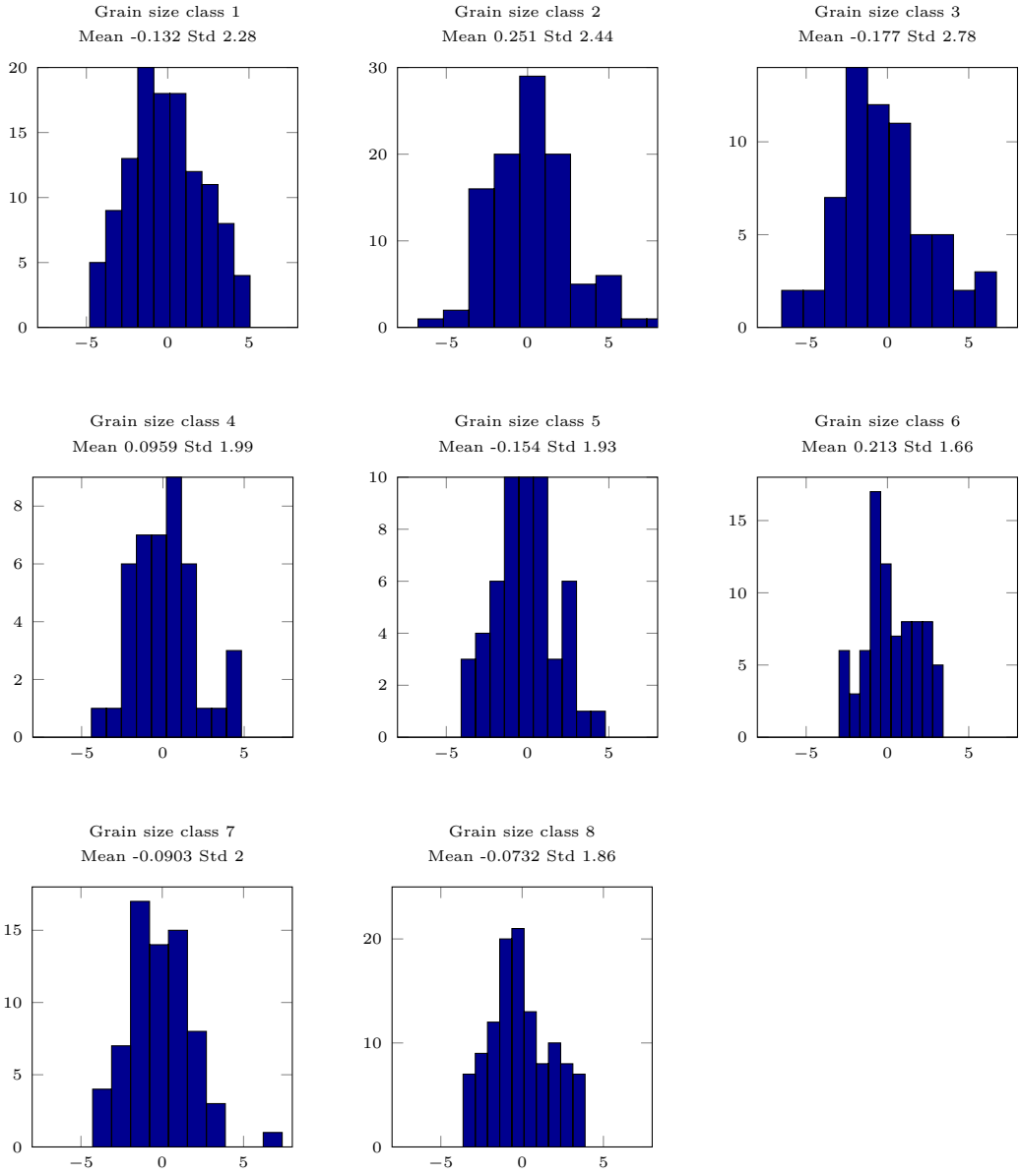

Thorium discrepancies based on the Bayesian dataset

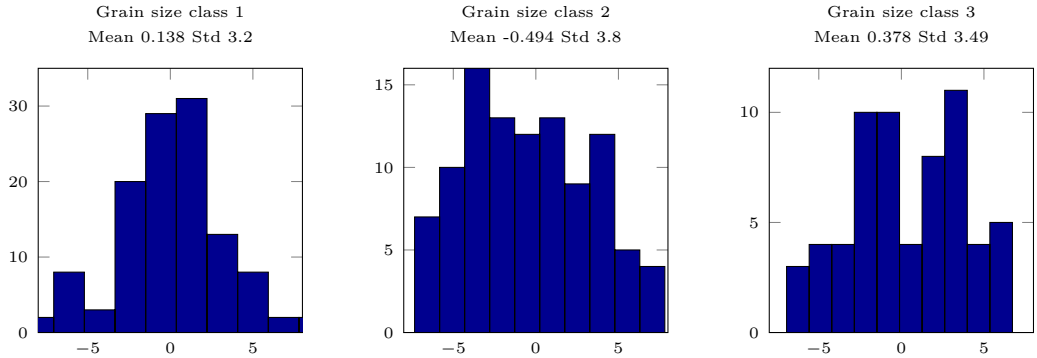

Grain size class 4
Mean 0.473 Std 2.9

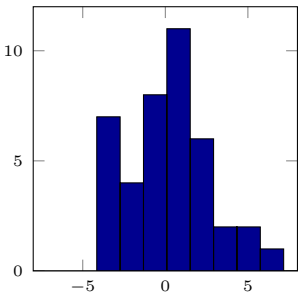

Grain size class 5
Mean 0.255 Std 2.35

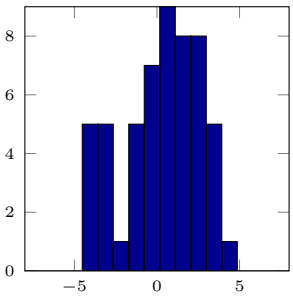

Grain size class 6
Mean -0.147 Std 2.34

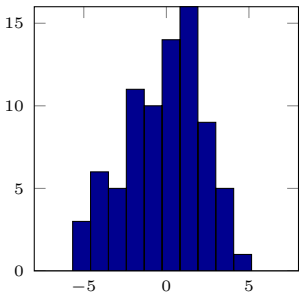

Grain size class 7
Mean 0.223 Std 2.03

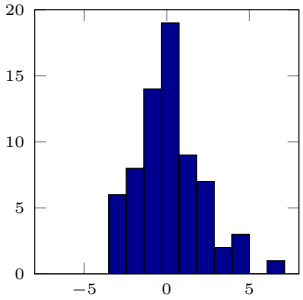

Grain size class 8
Mean -0.176 Std 2.18

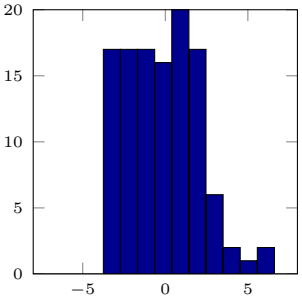

Potassium discrepancy based on the MVR dataset

Grain size class 1
Mean 0.00712 Std 0.502

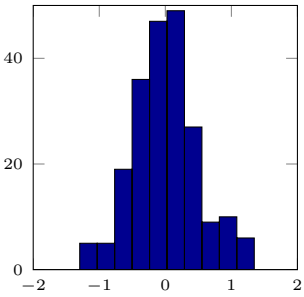

Grain size class 2
Mean -0.0412 Std 0.419

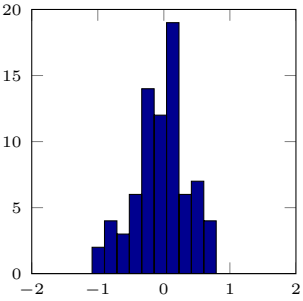

Grain size class 3
Mean 0.0387 Std 0.477

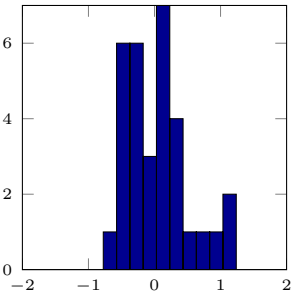

Grain size class 4
Mean -0.00684 Std 0.36

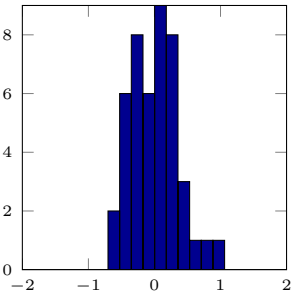

Grain size class 5
Mean 0.0198 Std 0.413

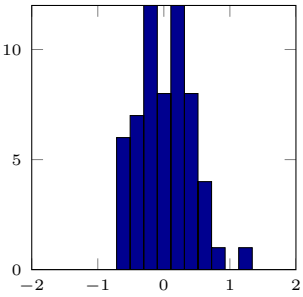

Grain size class 6
Mean -0.0219 Std 0.481

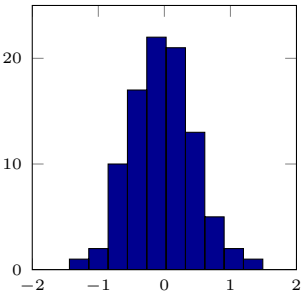

Grain size class 7
Mean 0.298 Std 0.461

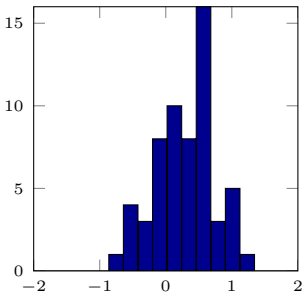

Grain size class 8
Mean 0.00508 Std 0.541

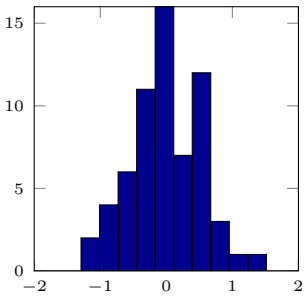

Uranium discrepancy based on the MVR dataset

Grain size class 1
Mean 0.0621 Std 2.41

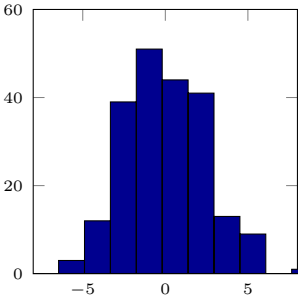

Grain size class 2
Mean -0.101 Std 2.65

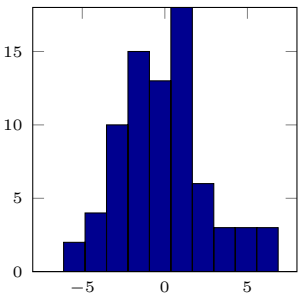

Grain size class 3
Mean -0.127 Std 2.08

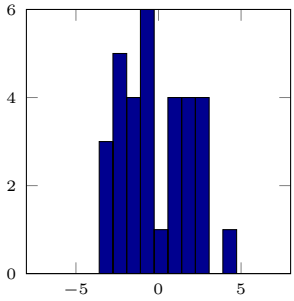

Grain size class 4
Mean -0.056 Std 2

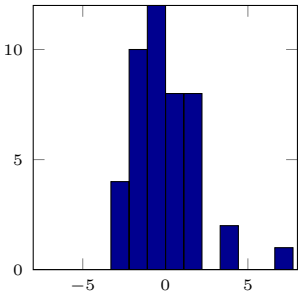

Grain size class 5
Mean -0.0417 Std 2.02

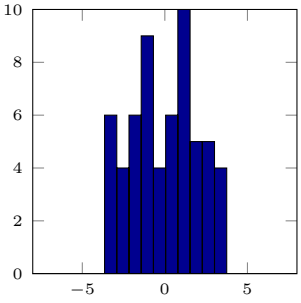

Grain size class 6
Mean 0.214 Std 1.87

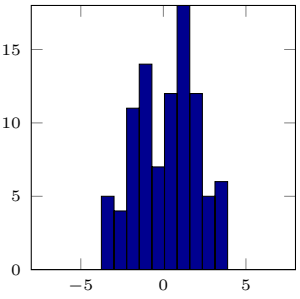

Grain size class 7
Mean -0.262 Std 1.86

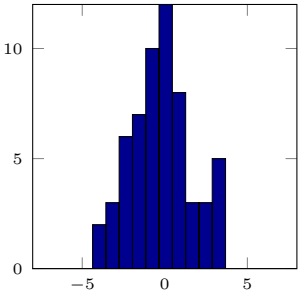

Grain size class 8
Mean -0.0271 Std 1.75

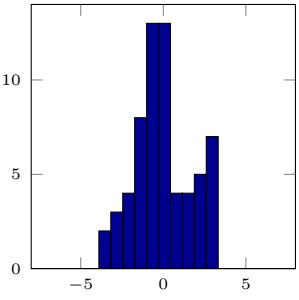

Thorium discrepancies based on the MVR dataset

Grain size class 1
Mean 0.0205 Std 3.55

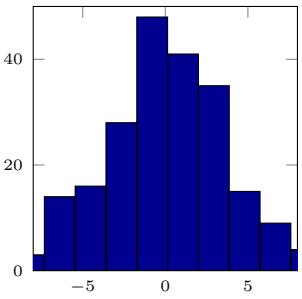

Grain size class 2
Mean -0.305 Std 3.57

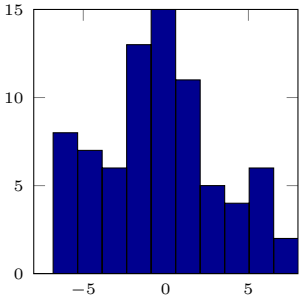

Grain size class 3
Mean 0.72 Std 3.1

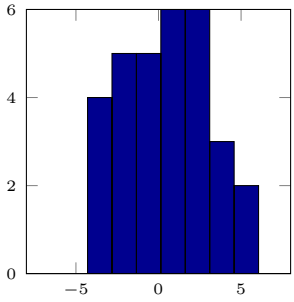

Grain size class 4
Mean 0.00329 Std 2.5

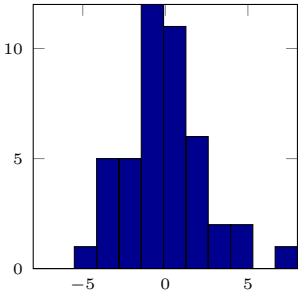

Grain size class 5
Mean -0.0483 Std 2.15

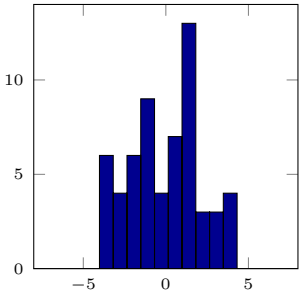

Grain size class 6
Mean -0.0645 Std 2.34

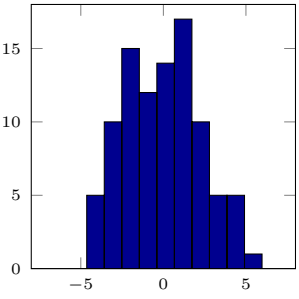

Grain size class 7
Mean 0.276 Std 2.51

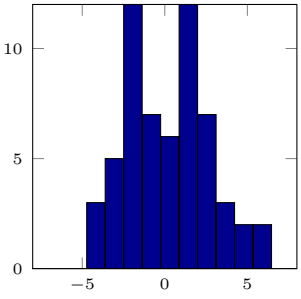

Grain size class 8
Mean -0.0553 Std 2

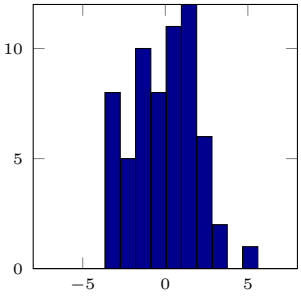

Appendix C

Huesca dataset

C.1 Well logs

Figure C.1 show the most important well logs logged in Piracés-1.

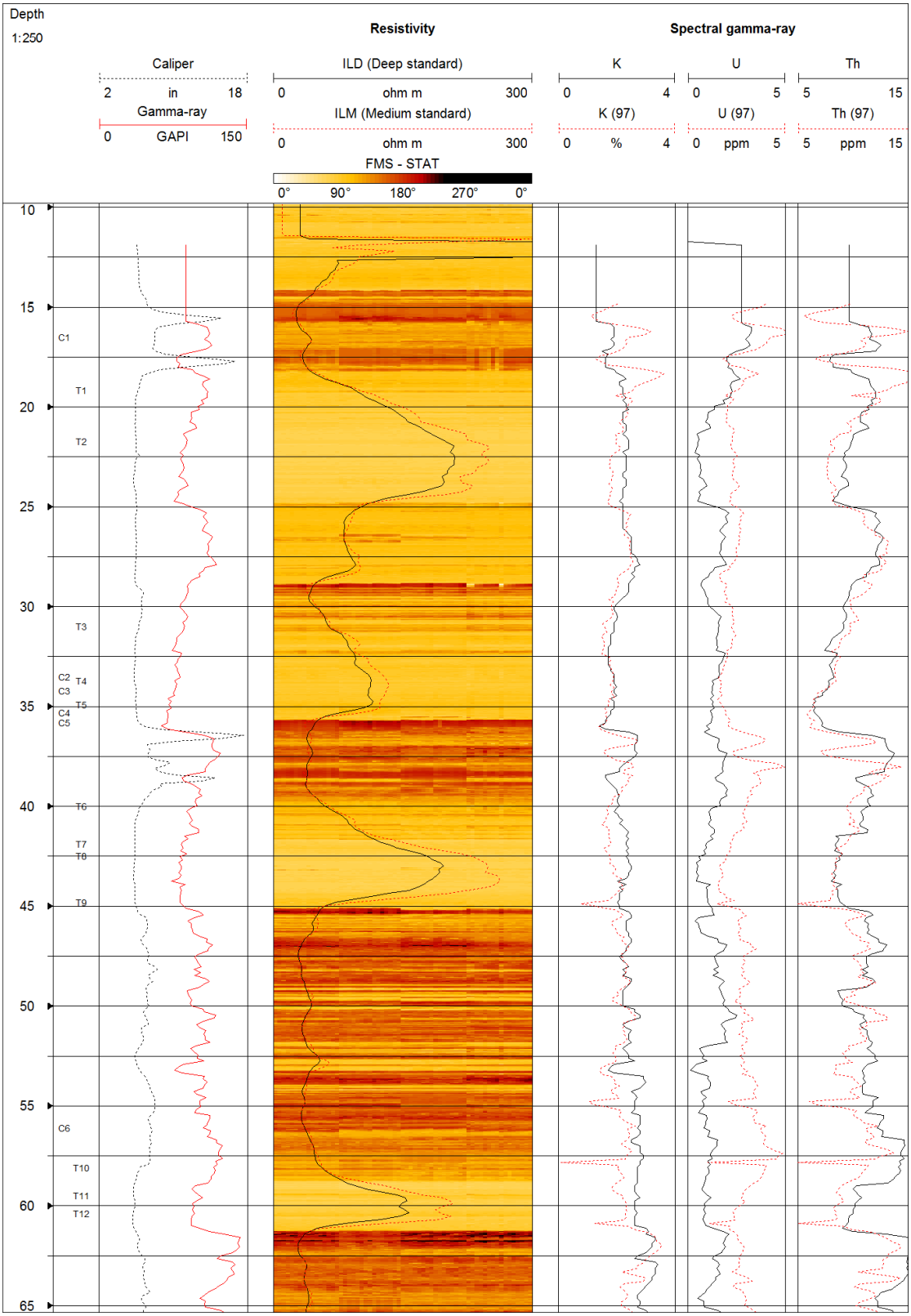

FIGURE C.1: Selection of well logs recorded in 1996 with the exception of indicated gamma-ray logs. Codes in left row refer to following samples used in the analysis of chapter 6 Cx = coreplugs sample x, Tx = Thin section sample x.

C.2 Core plug selection and analysis

The results of the core plug analysis can be found in table C.1. The standard deviations (listed as fraction) is the uncertainty based on count statistic.

Sample	**Mass** (gr)	**K** (%)	**S-K** (-)	**U** ppm	**S-U** (-)	**Th** ppm	**S-Th** (-)
51	24,2	2,44	0,11	-0,33	-1,40	14,88	0,11
119	32,4	1,62	0,11	-0,37	-0,73	7,78	0,13
122	37,8	1,35	0,11	-0,87	-0,27	8,06	0,12
126	28,4	0,98	0,10	-5,49	-0,11	14,87	0,13
127	33,4	2,69	0,09	0,36	1,20	13,29	0,11
209	35,6	2,13	0,09	0,18	2,13	11,06	0,12
264	39,8	2,13	0,09	1,05	0,37	11,58	0,11
293	26,8	2,28	0,10	-0,54	-0,78	13,61	0,12
296	30,0	2,34	0,10	-0,35	-1,08	11,76	0,12
309	42,0	2,65	0,06	-4,84	-0,06	21,54	0,06
353	38,6	2,44	0,07	-3,42	-0,10	15,42	0,08
357	40,2	2,34	0,07	-3,42	-0,10	15,42	0,08
488	32,4	2,49	0,09	0,27	1,45	10,44	0,13

TABLE C.1: Core plug radio-nuclide concentrations and grain size class.

C.3 Petrographic analysis

Rock samples were impregnated with blue- dyed epoxy resin to aid the identification of porosity. From each thin section the grain size, sorting and a qualitative description of mineralogy is given. The grain size is determined from the thin sections by randomly selecting 50 quartz/feldspar grains and measuring their longest axis (a). Johnson (1994) found that the true nominal diameter D can be approximated by multiplying the uncorrected mean axis length $\bar{a}$ by 0.95. This correction accounts for the 'sectioning' effect and converts the axis to a nominal diameter. The degree of sorting in each sample was estimated using a visual comparator developed by Jerram (2001). The findings are summarized in table C.2.

On the following pages a short qualitative mineralogy analysis is presented of each sample.

Sequence	**Depth (m)**	**Nominal grain size μm**	**Phi**	**Description**
1	19,18	235	0 - 0.36	(Very) well sorted
	21,75	368	0 - 0.36	(Very) well sorted
2	31	94	0	(Very) well sorted
	33,7	206	0.36	Well sorted
	34,9	425	0	Very well sorted
3	40	92	0.36	Well sorted
	41,9	277	0	Very well sorted
	42,5	445	0.67	Moderately well sorted
	44,8	485	1.06	Poorly sorted
4	58,1	37	0	Very well sorted
	59,5	177	0.67	Moderately well sorted
	60,4	378	0.36	Well sorted

TABLE C.2: Sample properties from thin section analysis.

Thin section photomicrographs

No photomicrograph

This thin section shows well sorted, medium sand sized particles with medium porosity. Metamorphic rock fragments, calcite and quartz are very abundant. Plagioclase and orthoclase are abundant. Biotite and volcanic rock fragments are scarce. Clay minerals are commonly present in the pore space.

Depth 19.18m **Grain size 235μm** **Point bar sequence 1**

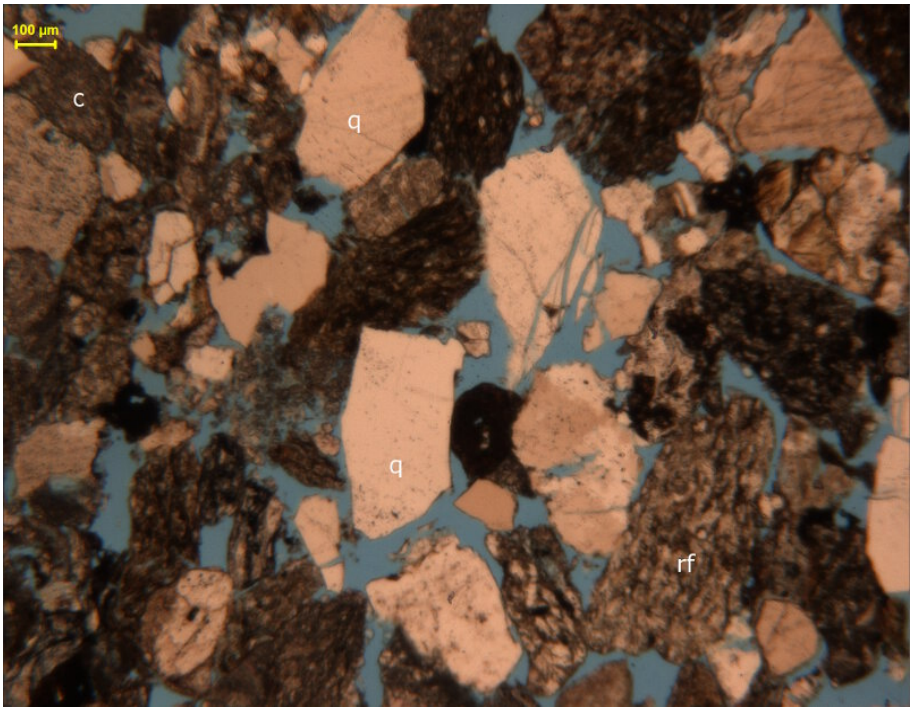

A. Magnification 5x Plane polarization

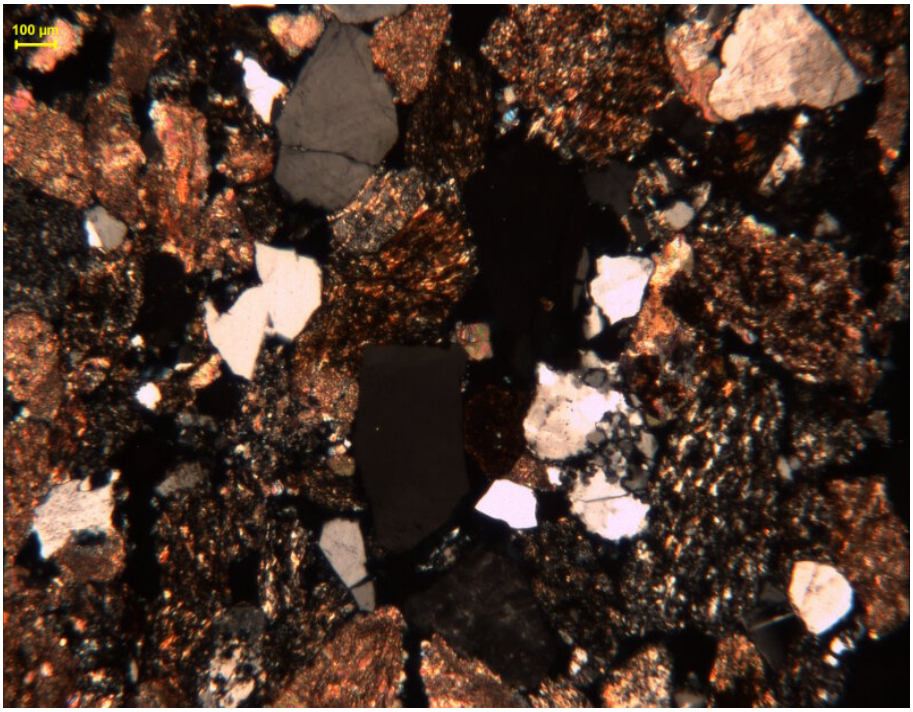

B. Magnification 5x Crossed nicols

This thin section shows well sorted, medium sand sized particles with (very) high porosity. Figure A shows abundant (Metamorphic) rock fragments (rf), calcite (c) and quartz (q). Plagioclase and orthoclase are abundant. Biotite is scarce. Clay minerals are almost absent in the pore space. Calcite precipitation in the pores is common .

Depth 21.75m **Grain size 368μm** **Point bar sequence 1**

No photomicrograph

This thin section shows very well sorted, very fine sand sized particles with low porosity. Quartz, Feldspar (Plagioclase), caclite are abundant. Biotite and muscovite are scarce. Clay minerals are commonly present in the pore space.

Depth 31.00m **Grain size 94μm** **Point bar sequence 2**

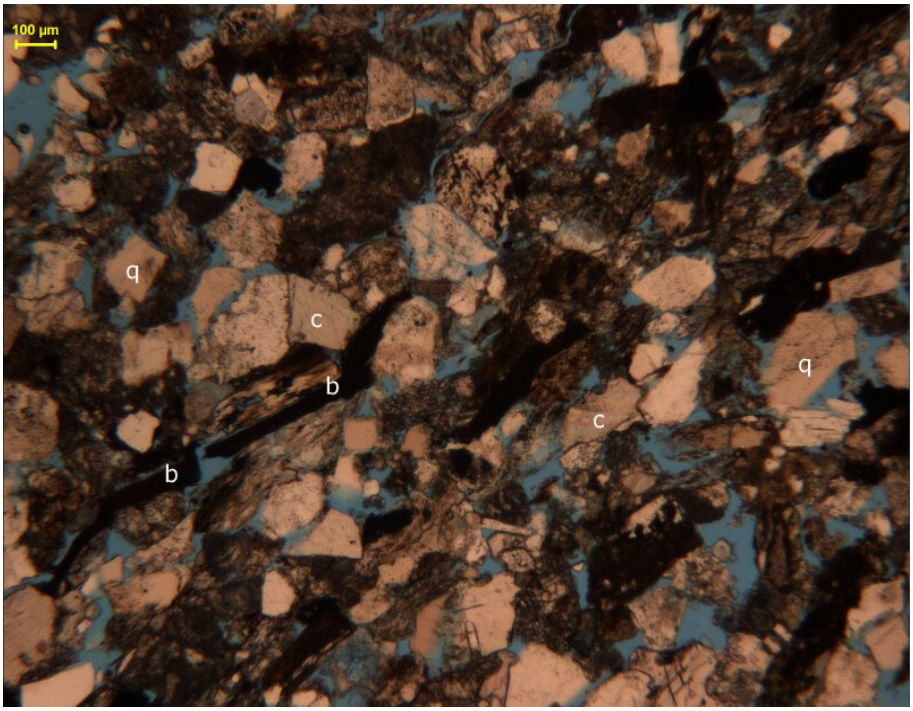

A. Magnification 5x Plane polarization

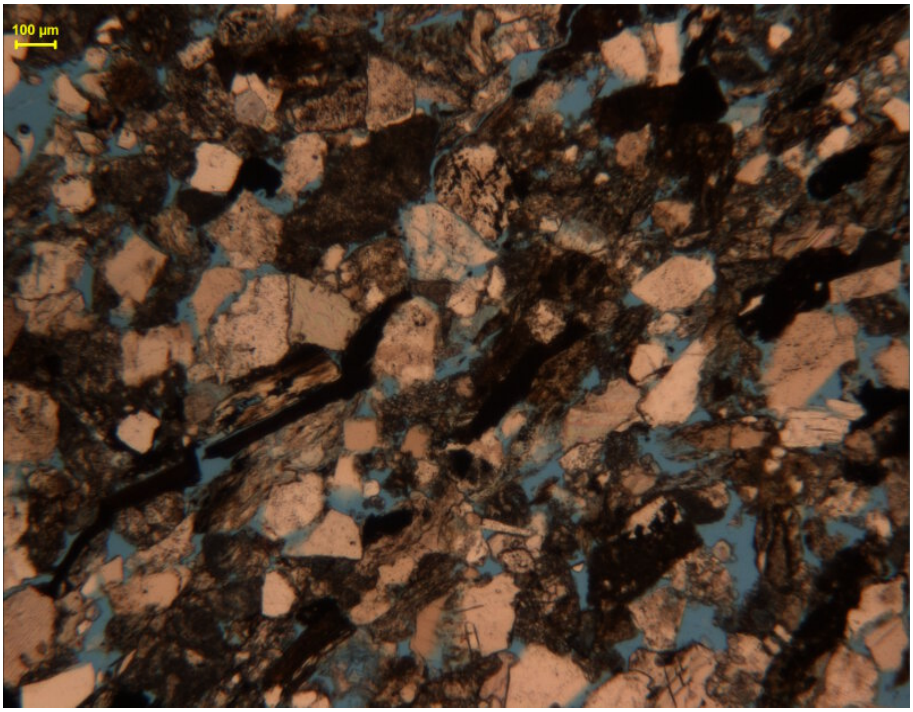

B. Magnification 5x Crossed nicols

These figures show well sorted, fine to medium sand sized particles with high porosity. Quartz, calcite and rock fragments are abundant. Some rock fragments partly dissolved. Figure A shows quartz (q), calcite (c) and deformed biotite (b).

Depth 33.70m **Grain size 206μm** **Point bar sequence 2**

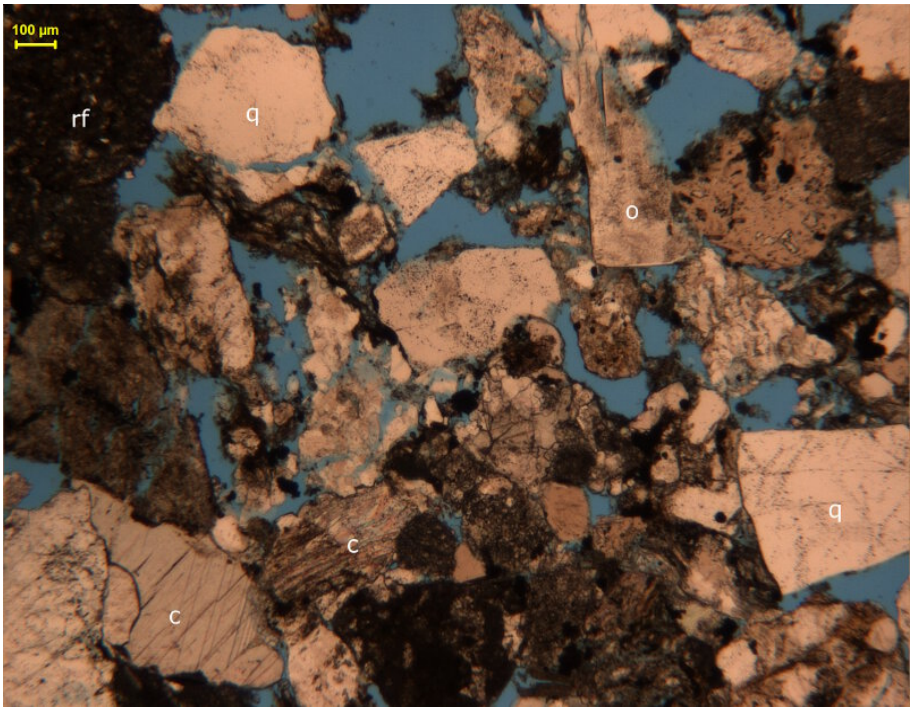

A. Magnification 5x Plane polarization

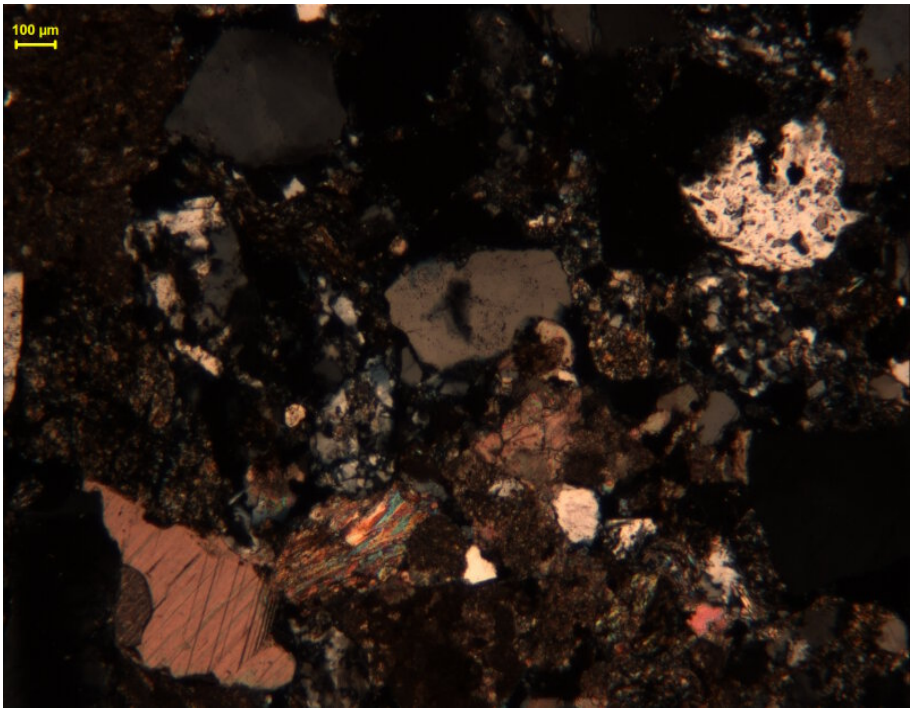

B. Magnification 5x Crossed nicols

This thin section shows very well sorted, poorly cemented, coarse sand sized particles with (very) high porosity. Calcite, rock fragments, quartz, orthoclase (commonly with albite twinning), plagioclase are abundant. Figure A shows partially altered orthoclase (o), quartz (q), calcite (c) and rock fragments (rf). Clay minerals are almost absent

Depth 34.90m **Grain size 425μm** **Point bar sequence 2**

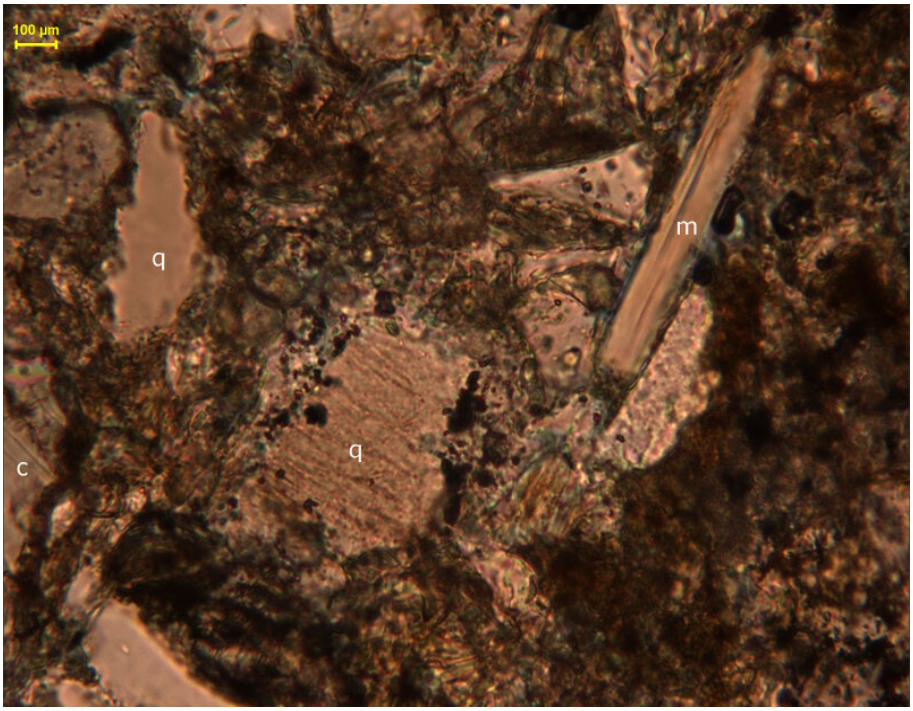

A. Magnification 25x Plane polarization

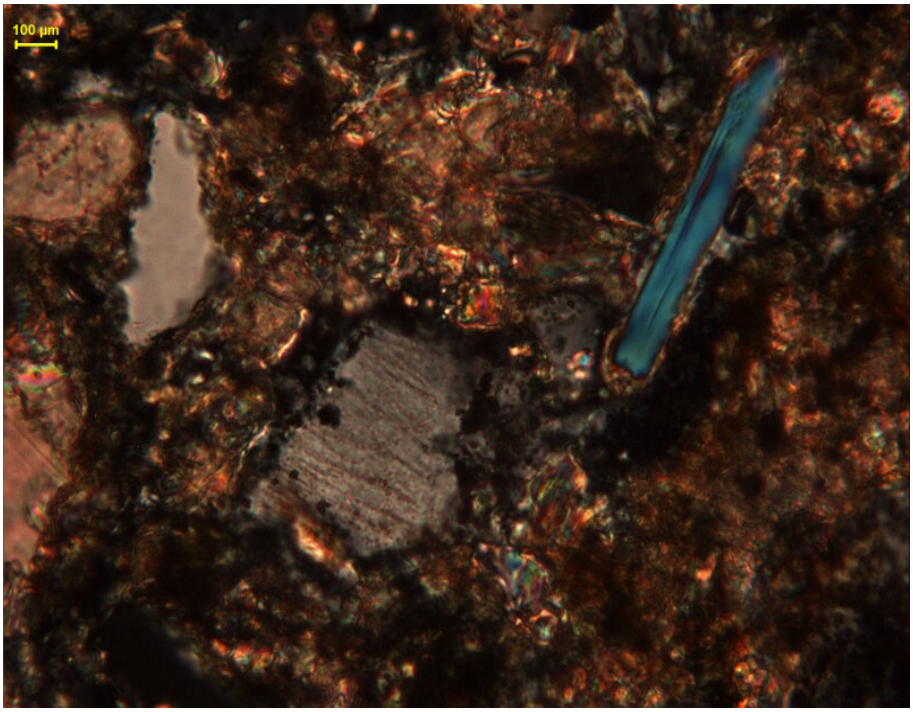

B. Magnification 25x Crossed nicols

This thin section shows well sorted, very fine sand sized particles with very low porosity. The thin section shows abundant Calcite (cement), clay minerals, quartz (q). Calcite precipitates are commonly observed in partially dissolved felspar grains. Muscovite is common (m).

Depth 40.00m **Grain size 92μm** **Point bar sequence 3**

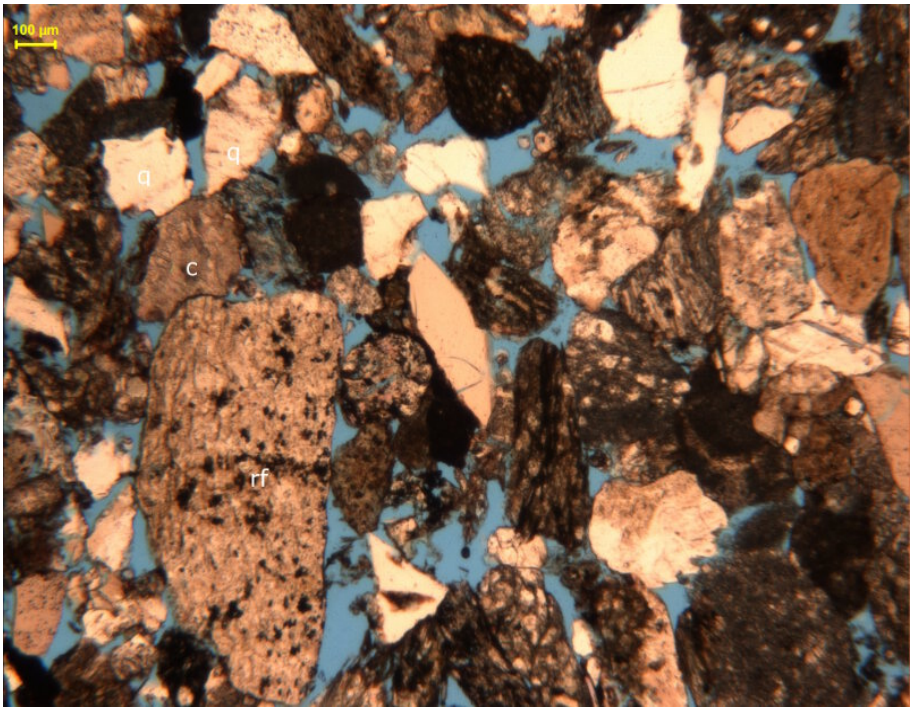

A. Magnification 5x Plane polarization

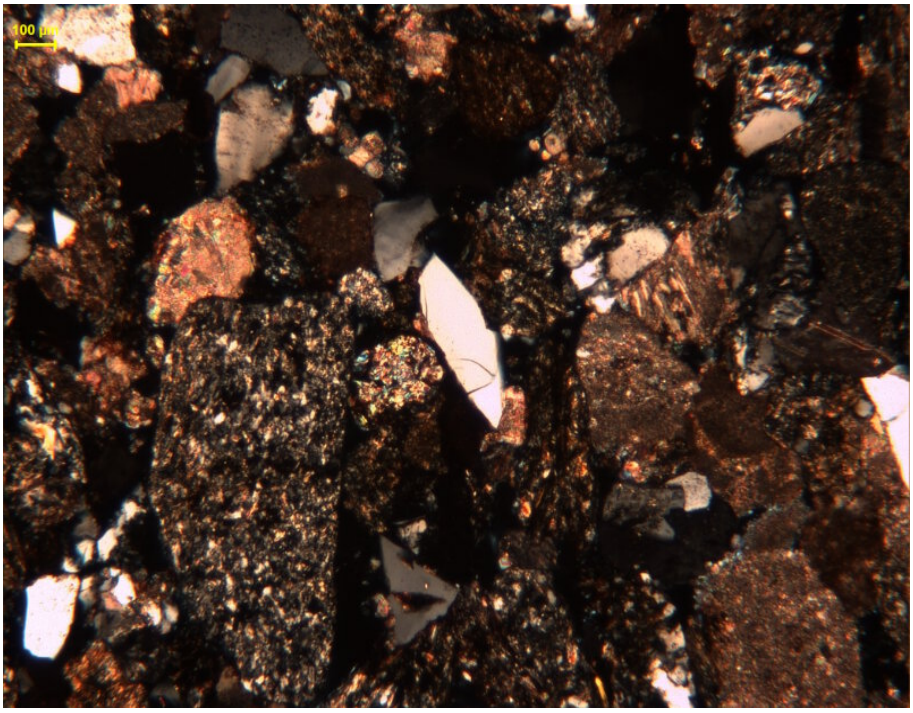

B. Magnification 5x Crossed nicols

This thin section shows very well sorted, fine sand sized particles with high porosity. The thin section shows abundant rock fragments (rf), calcite (c), quartz (q) and feldspar (orthoclase and plagioclase). A large proportion of rock fragments and feldspar grains are unaltered.

Depth 41.90m **Grain size 277μm** **Point bar sequence 3**

No photomicrograph

This thin section shows moderately sorted, coarse sand sized particles with high porosity. Rock fragments (metamorphic and some volcanic) calcite, quartz, plagioclase and orthoclase are abundant. Biotite is scarce.

Depth 42.50m **Grain size 445μm** **Point bar sequence 3**

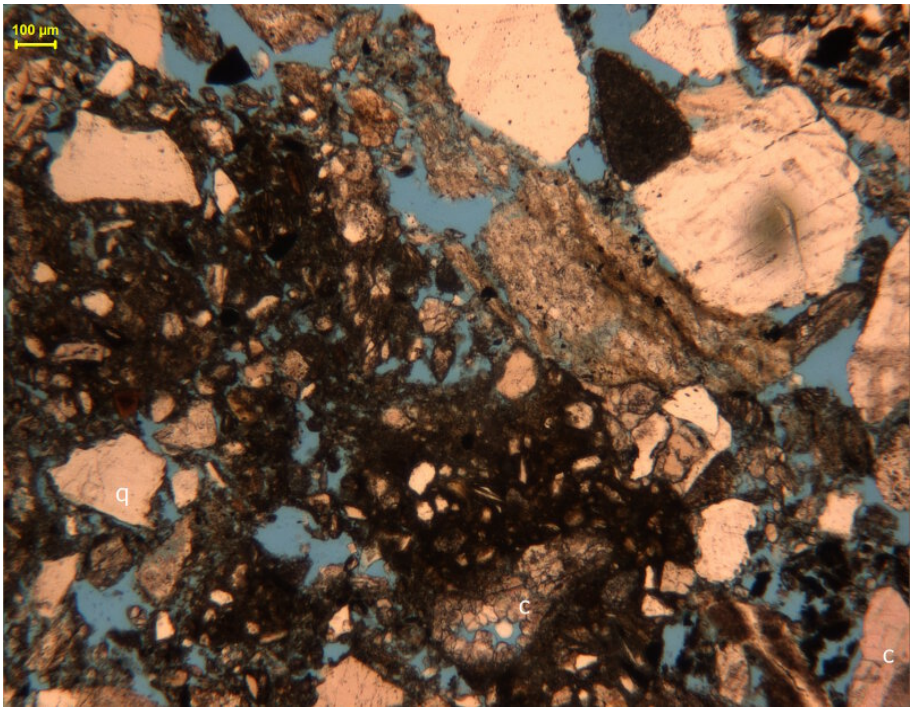

A. Magnification 5x Plane polarization

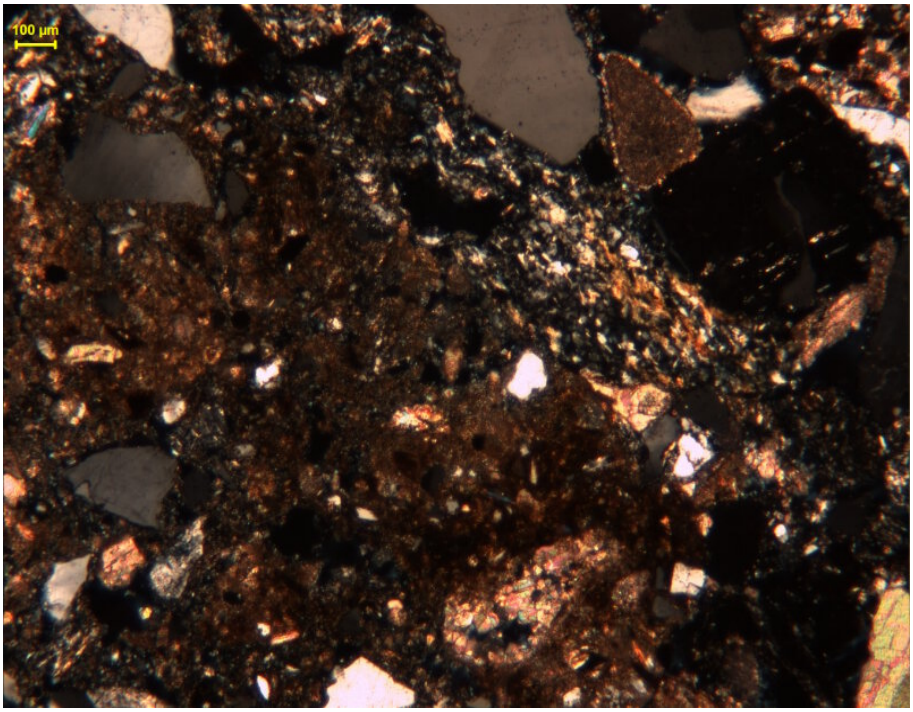

B. Magnification 5x Crossed nicols

This thin section shows poorly sorted, poorly cemented, coarse sand sized particles with very high porosity. Rock fragments,calcite, quartz and plagioclase and orthoclase are common. Clasts fragments cemented by calcite with muscovite inclusions. Figure A shows calcite precipitation in a pore(c) and quartz (q). Clay and biotite are rare.

Depth 44.80m **Grain size 485μm** **Point bar sequence 3**

No photomicrograph

This thin section shows very well sorted, silt sized particles with almost no visible porosity. Quartz grains, calcite are abundant. Muscovite and biotite are common. Matrix almost completely filled with clay minerals and calcite.

Depth 58.1m **Grain size 37μm** **Point bar sequence 4**

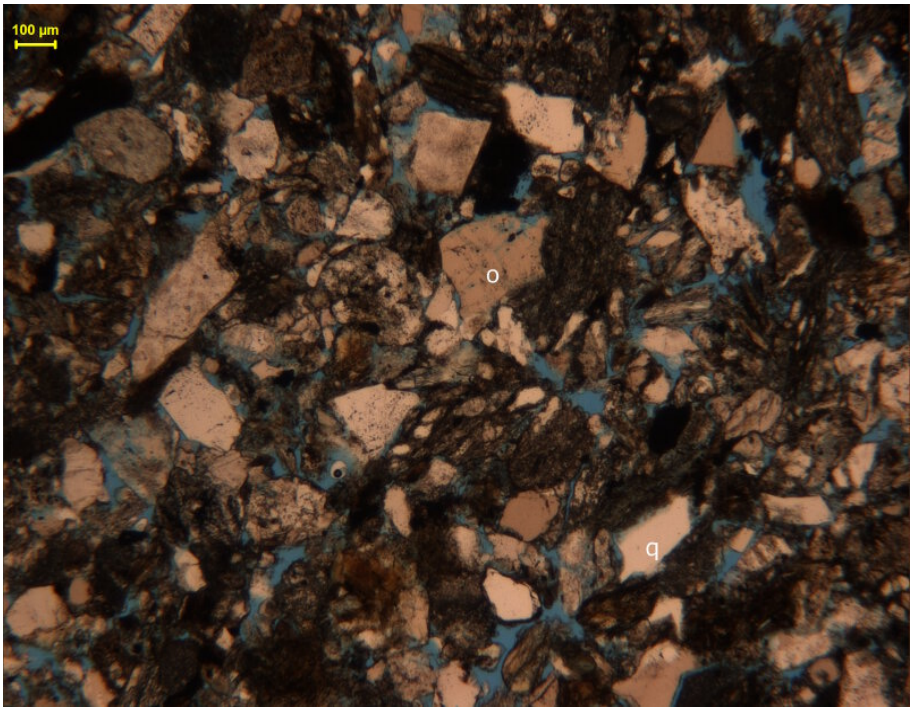

A. Magnification 5x Plane polarization

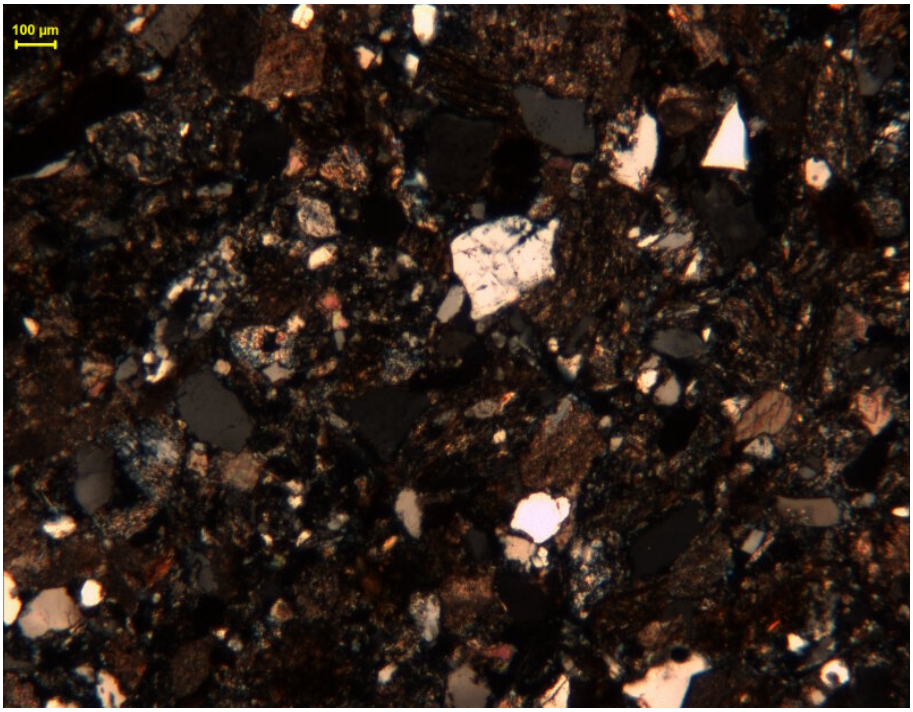

B. Magnification 5x Crossed nicols

This thin section shows moderately well sorted, medium sand sized particles with high porosity. Rock fragments,calcite, quartz and plagioclase and orthoclase are common. Figure A shows quartz (q) and orthoclase (o) with abundant clay minerals in the pore space.

Depth 59.5m **Grain size 177μm** **Point bar sequence 4**

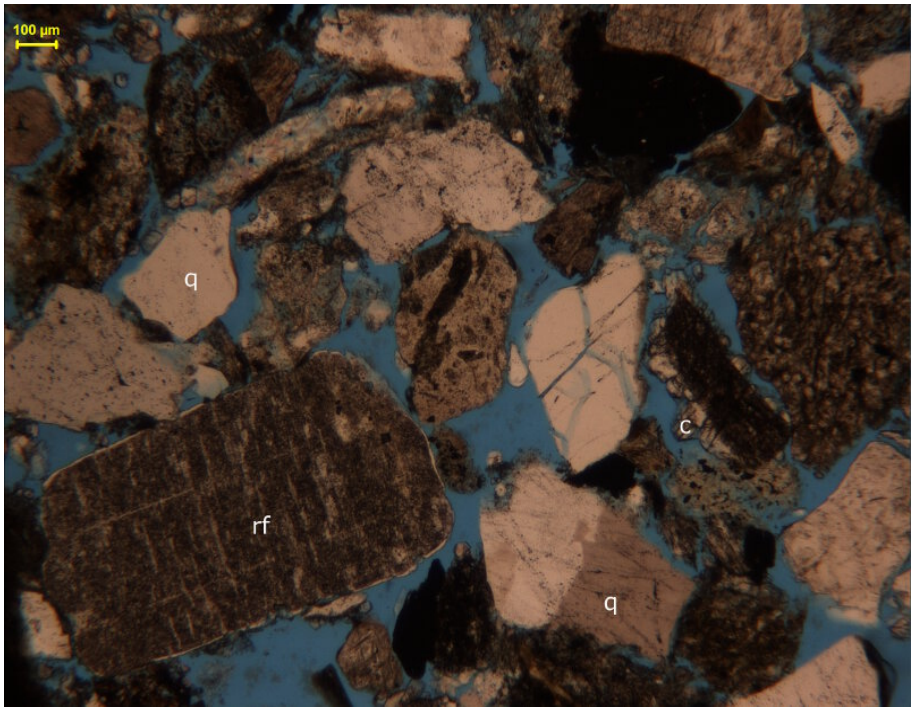

A. Magnification 5x Plane polarization

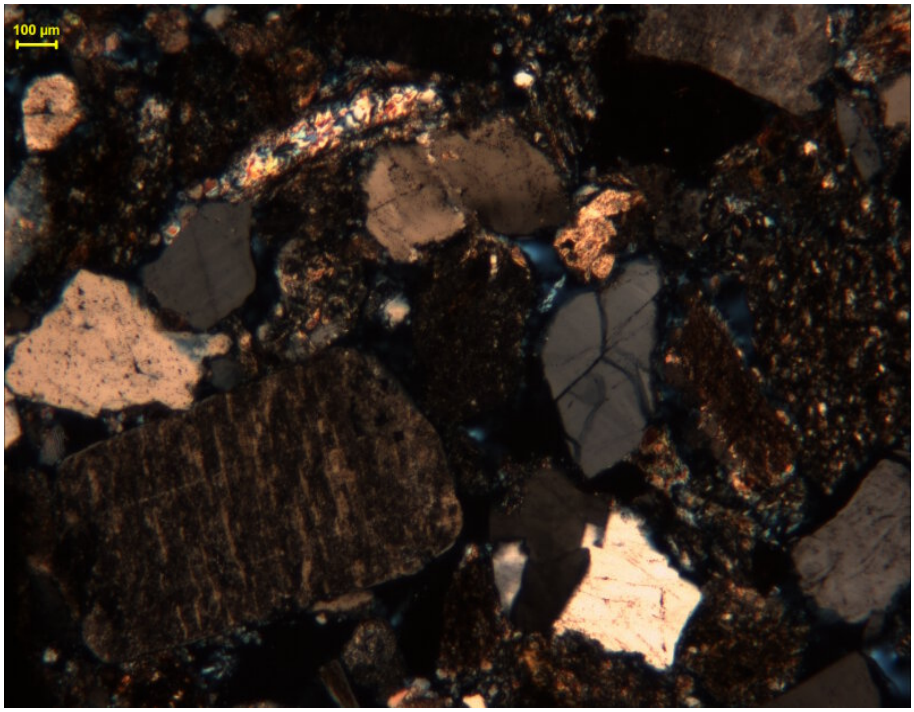

B. Magnification 5x Crossed nicols

This thin section shows moderately well sorted, poorly cemented, coarse sand sized particles with very high porosity. Rock fragments,calcite, quartz and plagioclase and orthoclase are common. Figure A shows quartz some with slight undulose extinction (q), a metmorphic rock fragment (rf) and precipitated calcite (c).

Depth 60.40m **Grain size 378μm** **Point bar sequence 4**

Bibliography

Aitchison, J. (1986). *The statistical analysis of compositional data*. Chapman and Hall.

Blatt, H., Middleton, G. V., and Murray, R. C. (1980). Origin of sedimentary rocks.

Bloemsma, M. (2010). Semi-automatic core characterisation based on geochemical logging data. Master's thesis.

Boels, J. (2003). Sedimentology, petrography and reservoir quality of the upper carboniferous in well e10-3. *Technical report, Panterra Nederland BV*.

Carmichael, R. (1982). *Handbook of physical properties of rocks*. CRC Press.

Donselaar, M. E. and Overeem, I. (2008). Connectivity of fluvial point-bar deposits: An example from the miocene huesca fluvial fan, ebro basin, spain. *AAPG bulletin*, 92(9):1109–1129.

Ellis, D. V. (2007). *Well logging for earth scientists*. Springer, Dordrecht, The Netherlands, 2nd edition. 2008921855 Darwin V. Ellis and Julian M. Singer. ill. ; 25 cm.

Fabricius, I., L.D., F., Steinholm, A., and Korsbech, U. (2003). The use of spectral natural gamma-ray analysis in reservoir evaluation of siliciclastic sediments: a case study from the middle jurassic of the harald field, danish central graben. *Geolog-ical Survey of Denmark and Greenland Bulletin*, 1:349–366.

Fertl, H., W., Chilingar, and V., G. (1988). Total organic carbon content determined from well logs. *SPE Formation Evaluation*, 3(2):407–419.

Gadekea, L., Jacobson, L. A., Merchant, G. A., and Wyatt, D. F. (1991). Resolution enhancement of nuclear measurements through deconvolution. *The Log Analyst*, 32(6).

Golub, G. and Reinsch, C. (1970). Singular value decomposition and least squares solutions. *Numerische Mathematik*, 14(5):403–420.

Hansen, P. (1998). *Rank-Deficient and Discrete Ill-Posed Problems: Numerical Aspects of Linear Inversion*. Society for Industrial and Applied Mathematics.

Hansen, P. C. (1994). Regularization tools: A matlab package for analysis and solution of discrete ill-posed problems. *Numerical algorithms*, 6(1):1–35.

Hassan, M., Hossin, A., and Combaz, A. (1976). Fundamentals of the differential gamma ray log - interpretation technique.

Hendriks, P., Limburg, J., and De Meijer, R. (2001). Full-spectrum analysis of natural gamma-ray spectra. *Journal of Environmental Radioactivity*, 53(3):365–380.

Hubbell, J. H. (1982). Photon mass attenuation and energy-absorption coefficients. *The International Journal of Applied Radiation and Isotopes*, 33(11):1269–1290.

Hurst, A. (1990). Natural gamma-ray spectrometry in hydrocarbon-bearing sandstones from the norwegian continental shelf. *Geological Society, London, Special Publications*, 48(1):211–222.

Jerram, D. A. (2001). Visual comparators for degree of grain-size sorting in two and three-dimensions. *Computers & Geosciences*, 27(4):485–492.

Johnson, M. R. (1994). Thin section grain size analysis revisited. *Sedimentology*, 41(5):985–999.

Komar, P. D., Baba, J., and Bingquan, C. (1984). Grain-size analyses of mica within sediments and the hydraulic equivalence of mica and quartz. *Journal of Sedimentary Research*, 54(4):1379–1391.

Komar, P. D. and Cui, B. (1985). Analysis of grain-size measurements by sieving and settling-tube techniques. *International Journal of Rock Mechanics and Mining Sciences & Geomechanics Abstracts*, 22(3):A80–A81.

Koomans, R. (2000). *Sand in motion: Effects of density and grain size*. PhD thesis.

Lagarias, J. C., Reeds, J. A., Wright, M. H., and Wright, P. E. (1998). Convergence properties of the nelder–mead simplex method in low dimensions. *SIAM Journal on Optimization*, 9(1):112–147.

Luthi, S. M. (2000). *Geological Well Logs: Their Use in Reservoir Modeling*.

Menke, W. (2012). Chapter 4 - solution of the linear, gaussian inverse problem, viewpoint 2: Generalized inverses. In Menke, W., editor, *Geophysical Data Analysis: Discrete Inverse Theory (Third Edition)*, pages 69 – 88. Academic Press, Boston, third edition edition.

Nichols, G. (2009). *Sedimentology and Stratigraphy*. Wiley.

Palomares Herranz, M., Tortosa, A., and Arribas Mocoroa, J. (1990). Caracterizacias-tomica de los depos detrcos de cabecera de arroyos en el sistema central: influencia de la litologel a fuente. *Bolete la Real Sociedad Espa de Historia Natural. Secciola*, 85(1-5):5–21.

Rider, H. (2002). *The Geological Interpretation of Well Logs*. Rider-French Consulting.

Rider, M. H. (1990). Gamma-ray log shape used as a facies indicator: critical analysis of an oversimplified methodology. *Geological Society, London, Special Publications*, 48(1):27–37.

Sanchez-Ramirez, J., Torres-Verdan, C., Z., L., Wolf, D., M., A, W., and G.L., Schell, G. (2010). Field examples of the combined petrophysical inversion of gamma-ray, density, and resistivity logs acquired in thinly-bedded clastic rock formations. *Petrophysics*, Vol. 51(No. 4):P. 247–263.

Serra, O. (1988). *Fundamentals of well-log interpretation: I The Acquisition of Logging Data*.

Serra, O., Sulpice, L., et al. (1975). Sedimentological analysis of shale-sand series from well logs.

von Eynatten, H. (2004). Statistical modelling of compositional trends in sediments. *Sedimentary Geology*, 171(1-4):79–89.

Weltje, G. J. (2004). A quantitative approach to capturing the compositional variability of modern sands. *Sedimentary Geology*, 171(1):59–77.

Weltje, G. J. (2012). Quantitative models of sediment generation and provenance: State of the art and future developments. *Sedimentary Geology*, 280(0):4–20.

Weltje, G. J. (2014). (in press).

Weltje, G. J. and von Eynatten, H. (2004). Quantitative provenance analysis of sediments: review and outlook. *Sedimentary Geology*, 171(1-4):1–11.

Wu, W. and Wang, S. S. (2006). Formulas for sediment porosity and settling velocity. *Journal of Hydraulic Engineering*, 132(8):858–862.

Yuste, A., Luz., and Bauluz, B. (2004). Provenance of oligocenemiocene alluvial and fluvial fans of the northern ebro basin (ne spain): an xrd, petrographic and sem study. *Sedimentary Geology*, 172(34):251–268.